Spring 2019

# Estimation of Arterial Wall Parameters Via Model-Based Analysis of Noninvasively Measured Arterial Pulse Signals

Dan Wang
*Old Dominion University*, d2wang@odu.edu

# ESTIMATION OF ARTERIAL WALL PARAMETERS VIA MODEL-BASED ANALYSIS OF NONINVASIVELY MEASURED ARTERIAL PULSE SIGNALS

by

Dan Wang
B.S., June 2010, Southwest University of Science and Technology, China
M.E., June 2013, University of Electronic Science and Technology of China, China

A Dissertation Submitted to the Faculty of
Old Dominion University in Partial Fulfillment of the
Requirements for the Degree of

DOCTOR OF PHILOSOPHY

MECHANICAL ENGINEERING

OLD DOMINION UNIVERSITY
May 2019

Approved by:

Julie Zhili Hao (Director)

Leryn Reynolds (Co-Director)

Linda Vahala (Member)

Thomas Alberts (Member)

## ABSTRACT

ESTIMATION OF ARTERIAL WALL PARAMETERS VIA MODEL-BASED ANALYSIS OF NONINVASIVELY MEASURED ARTERIAL PULSE SIGNALS

Dan Wang
Old Dominion University, 2019
Director: Dr. Julie Zhili Hao

This dissertation presents a model-based method for estimating arterial wall parameters from noninvasively measured arterial pulse signals via a microfluidic-based tactile sensor. The sensor entails a polydimethylsiloxane (PDMS) microstructure embedded with $5\times1$ transducer array built on Pyrex/Polyethylene terephthalate (PET) substrate. The arterial pulse causes a time-varying deflection on the top of the PDMS microstructure, which registers as a resistance change by the transducer at the site of the artery.

Owing to the time-harmonic nature of its radial motion, the arterial wall is modeled as a second-order dynamic system. By combining this dynamic model with a hemodynamic model of blood flow, the arterial wall parameters: elasticity, viscosity, and radius, were represented by spring constant and damping coefficient. Moderate exercise was utilized to introduce changes in arterial wall parameters because sensor-artery interaction varies with arteries and subject-specificity (i.e. overlying tissue and blood pressure). The same sensor was used to measure pulse signals pre-exercise and post-exercise on a subject for tracking changes of arterial wall parameters. The estimated values on five subjects revealed a statistically significant difference between pre-exercise and post-exercise ($p<0.05$).

A measured arterial pulse signal is a combination of the sensor design, hold-down pressure, and subject-specificity. Optimization of the sensor design was needed to improve the sensor-artery interaction for maximizing the measured pulse amplitude. Toward this end, the

same sensor design with a PDMS conformal layer of different mixing ratios (elastomer curing agent and base) and different thickness was tried to improve the sensor-artery interaction in six subjects with different BMI. Adding a conformal layer was found to significantly increase the amplitude of a measured pulse signal in a subject with high BMI. The changes in arterial wall parameters introduced by moderate exercise were estimated from the measured signals using the sensor with a conformal layer on two subjects. The obtained changes in arterial wall parameters were consistent with the measured changes using a medical instrument.

In summary, the feasibility of a model-based method for estimating arterial wall parameters from measured arterial pulse signals was validated using the changes introduced by moderate exercise on several subjects. Future work will focus on implementing the sensor for practical use.

This thesis is dedicated to my parents and sisters.

## ACKNOWLEDGMENTS

Completion of this dissertation was impossible without the support, guidance, and encouragement of several people. I want to express my gratitude to all of them.

Firstly, I sincerely would like to express my sincere gratitude to my principle advisor Dr. Julie Zhili Hao for giving me an opportunity to complete my Ph.D. thesis under her supervision, it is indeed an honor. Thank you for providing me with fruitful ideas, valuable advice, support, encouragement, patience, and kindness in guiding me through this project. She has been a great mentor and a constant source of inspiration for me in the past years. The thesis cannot be complete without her guidance and help, especially in writing. I appreciate this excellent research opportunity provided by Dr. Hao, which widens my horizon and sheds light on my future career. I will also be grateful for her kindness and encouragement when I was sick or felt depression during the past years.

Next, I would like to thank Dr. Leryn Reynolds, who co-advised this research. She is an excellent professor and an expert in human exercise who gives valuable advice and helps with the arterial pulse measurements on subjects. I appreciate all her help for IRB application. I deeply thank her for spending time on arterial pulse measurement after moderate exercise and further efforts on data analysis.

I want to express my appreciation to committee member Dr. Alberts for his constant support, encouragement, collaboration, and insightful advice. Thank you taking time out for helping me on writing. Thanks also to committee member Dr. Vahala for supporting, guiding and spending time on my project.

I also acknowledge the excellent research facilities and opportunities provided by the Department of Mechanical and Aerospace Engineering at Old Dominion University. I am

grateful to all the professors, classmates, and staff for their support in the last years. I want to express my gratitude to the department chair Dr. Sebastian Bawab, the department GPD Dr. Miltos Kotinis, former GPD Dr. Han Bao, Dr. Dipankar Ghosh, Dr. Abdelmageed Elmustafa, and Dr. Shizhi Qian. Thanks also to Ms. Diane Mitchell and Ms. June Blount for their constant support.

A special thanks to all the team members in Micro Devices and Micromechanics Laboratory (MDML) Lab, both past and present, deserve acknowledgments. I would like to express my thanks to Ms. Wenting Gu, Ms. Jiayue Shen, Mr. Yichao Yang, Mr. Siqin Dong, Mr. MD Aktharuzzaman, and Mr. Dabhi Saumikkumar Mahendrabhai for sharing ideas, thoughts, and giving me constant support. I deeply appreciate their help for sharing ideas on device fabrication, recruiting subjects for arterial pulse measurement, and spending time for assisting the experiment. Additionally, I would like to thank Mr. Xavier-lewis Palmer for his training on sample preparation and sharing the experience on communication skills. Also, thanks to Mr. Kevin Colvin and Mr. Larson Lindberg in Engineering Model Shop, who helped to prepare the fundamental components and samples for experiments.

I am grateful to all my friends for their great company and constant support during highs and lows while I pursue my academic goals. It is a beautiful memory for the time spent with my roommates, Ms. Liuliu Fu, Ms. Wenlu Zhang, Ms. Yi Jian, Ms. Yueming Zhou, Ms. Luni Sun, Ms. Chen Jin, Ms. Chenxi Luo, Ms. Xiaozhang Siwen, Ms. Rui Wang, Ms. Chen Wei, and Ms. Chi Li. I appreciate their sincere encouragement and sharing stories and opinions in the past years. A special thanks to Dr. Wenfeng Zheng, Dr. Xiaolu Li, and Dr. Shan Liu for supporting and encouraging me to pursue my dream and build a future career. Thanks for sharing experience

and giving me valuable advice. I appreciate the way they helped me and am thankful for our friendship.

Many thanks are also due to my sisters Ling and Jia. Thank you for the constant support and encouragement. Thank you for looking after my parents while I spent many years away from home to pursue my Ph.D. degree. I appreciate the kind support and heartily encouragement from other members of my family and family friends. My most profound appreciation I owe to my parents for raising me in a loving home with my loving sisters. Thank you for creating a stable and lovely environment to grow and discover my passions in research. Thanks to their generous support to pursue my dream and complete my Ph.D. study.

# TABLE OF CONTENTS

Page

# LIST OF TABLES

# LIST OF FIGURES

Figure Page

Figure Page

Figure Page

Figure Page

Figure Page

# CHAPTER 1

# INTRODUCTION

As the single leading cause of death worldwide [1], cardiovascular diseases (CVDs) have been studied for their diagnosis and treatment over the years [2]. With the global trend of obesity, aging, and unhealthy lifestyle, CVDs have been more prevalent and posed a significant burden to the healthcare system. The majority of CVDs are associated with atherosclerosis (arterial stiffening) [3]. Early detection, diagnosis, and treatment can slow their progress and prevent adverse CVDs. In current clinical practice, an invasive or non-invasive method is commonly used for evaluating the cardiovascular condition of an individual.

## 1.1 Clinical Relevance of Arterial Wall Parameters

### 1.1.1 Biological Characteristics of Artery

The functionality of the artery in the blood circulation through the cardiovascular system is of great importance. Understanding the underlying physiology is critical to study the arterial wall parameters, i.e., elasticity, viscosity, and radius. The blood circulation originates from the heart pumping blood through aorta from the left ventricle to the lungs for oxygenation. Then the blood flows along the arterial tree with saturated oxygen. The role of the artery in the cardiovascular system is to carry blood down to blood vessels and capillaries for exchanging nutrients. A strong and thicker wall with enhanced mechanical property of an artery is required to counterbalance the high pressure from the heart. The blood returns to the heart with oxygen-depleted blood through a converging low-pressure system of veins, which have thinner walls [4].

The mechanical property of the arterial wall is viscoelastic by nature, i.e., exhibits elastic and viscous properties. The stress-strain curve provides a measure of a material’s mechanical property when subjected to an external load. The stress symbolizes the force applied per unit area

on the material, while the strain means the deformation under the load. According to Hooke's law, the stress-strain curve is linear, which is independent of time, in purely elastic materials, while it is nonlinear in viscous materials. Due to the viscoelastic property of an artery, it becomes stiffer after receiving rapid stress, while it becomes softer after receiving slow stress [5]. The elastic modulus or Young's modulus is calculated as the slope of a stress-strain curve when the arterial wall is treated as a purely elastic material. The incremental Young's modulus is calculated as the slope of the loading curve defined by a tangent line when a material has viscoelastic characteristics [6].

The mechanical property of the artery depends on the biological composite and structure. The artery is a muscular tube with smooth tissue and has three layers, tunica intima inside of the artery, tunica media in the middle, and tunica adventitia on the outside. The innermost layer is one layer of endothelial cells, which is directly contacted with blood flow and supported by an internal elastic lamina [7]. The middle layer is made up of smooth muscle cells, elastic tissue, and collagen. The outermost layer is composed of collagen and elastic fiber to form connective tissue surround the artery, which is supported by an external elastic lamina. The mechanical behavior of an artery primarily depends on tunica media and tunica adventitia under low or high blood pressure. The role of these layers is to protect the arteries from stretching beyond the physiological limits during a cardiac cycle. Elastic continents contribute to the elastic property of the artery at low pressure. As the pressure increased, the collagen fibers will contribute larger tensile strength than elastic continents from the initially unstretched state [8]. Thus, Young's modulus increases with the arterial pressure exponentially at high pressure.

### 1.1.2 Causes and Consequences of Arterial Stiffening

The change in biological composite and structure of the artery alters the mechanical properties of the arterial wall, which affects its functionality of carrying blood and becomes risk factors of cardiovascular events. The related changes involve structure, function, and size of the arterial wall and the mean arterial blood pressure (BP). Arterial stiffening, which is the increased rigidity of an arterial wall, occurs in association with these changes. Arterial stiffness, which denotes the loss of elasticity, is commonly used to represent the mechanical property of the artery.

Aging and atherosclerosis can lead to arterial stiffening by modifying the arterial wall structure, function, and size. Arterial stiffening may be both a cause and consequence of CVDs risk, such as hypertension. The elastin fibers, which mediates the arterial stiffness, degrade during the aging process. It results in a rising arterial stiffness and blood pressure with age. The comparison of the aortic and radial pressure waveforms for two adults, a 68-year-old subject and his 37-year-old son, [9] are shown in Figure 1.1. The stiffened arterial wall causes earlier reflection to the heart, and as a consequence, the aortic pressure increases. The blood pressure is higher in the old subject than that in the young subject due to their different arterial wall condition. Atherosclerosis is another cause of arterial stiffening. Arterial stiffening arises from the accumulation of lipids in the intimal lining of a large or medium-sized artery. Inflammation in the narrowed arterial caliber results in calcification of lipids, the build-up of hard plaques, and fibrotic lesions [10]. These changes in arterial structure have ramifications on blood circulation, blood pressure, and add burden to the heart. It can be prevented by early diagnosis and treatment. Otherwise, the stiffened artery increases wave reflection in systole, which leads to more burden to the heart.

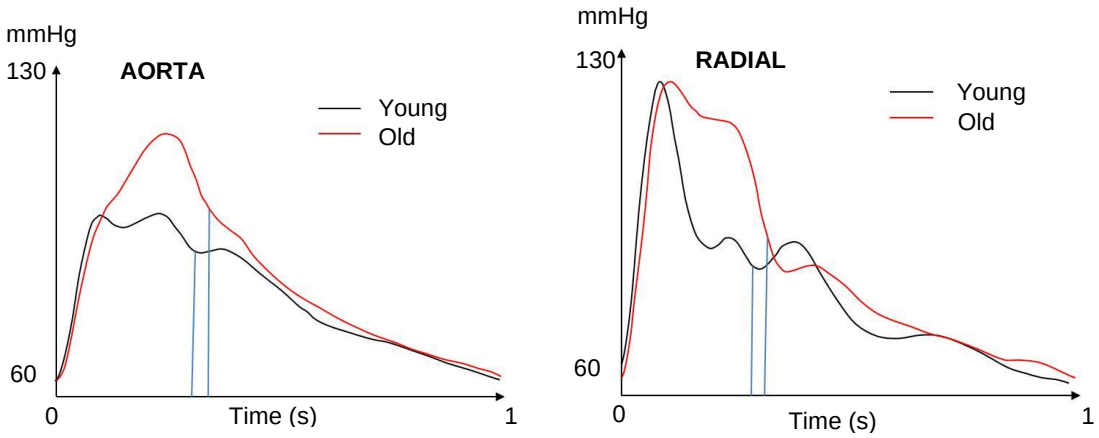


(a) (b)

Figure 1.1 Aortic (a) and radial (b) pressure wave in a 36-year-old man (young) and his 68-year-old father (old) [9].

Changes in the components and structures of the arterial wall affect the function of the artery and BP. The aortic and branch arterial waves are composed of two waves in a cardiac cycle [5]: the ejection wave, and the reflected wave. The ejection wave originates from the heart pumping blood and propagates waves in the arterial tree. It is influenced by the ventricular ejection from the heart and the stiffness of the aorta. The reflected wave returns at the end of the systolic contraction from the peripheral arteries to the heart. This wave mainly depends on the reflection coefficients, the degree of arterial stiffening, Pulse Wave Velocity (PWV), and the distance between the heart and the reflection point [11]. The stiff artery causes the ejection wave to propagate more quickly in the arterial tree and the reflected wave to arrive faster. It increases the stress in the arterial wall because the wave reached during systole is supposed to arrive during diastole. The heart needs to work harder to pump blood from the heart to the whole body due to the early wave reflections, which increases systolic BP and decreases diastolic BP. The mean arterial pressure may be raised over normal among patients with CVDs, such as hypertension, diabetes, and end-stage renal disease (ESDR). However, the systolic BP has disproportional increases over diastolic BP [11].

### 1.1.3 Arterial Wall Parameters

Arterial wall parameters, namely elasticity, viscosity, and radius, are prognostic markers of the cardiovascular system. They provide valuable information for evaluating the mechanical properties of the arterial wall, which is related to CVDs.

Arterial stiffness, namely the loss of elasticity of the arterial wall, has been well established as an independent risk predictor of adverse cardiovascular events at an early stage [3]. Because of the complexity of the cardiovascular system in the human body, the characterization of arterial stiffness is problematic due to three reasons. First, the mechanical property of an arterial wall varies at any location in the arterial tree. Second, the physical and chemical wall properties of an arterial wall vary from site to site. Third, the pressure wave is a combination of the ejection wave from the heart and reflected wave from the periphery artery, which travels a long distance [12]. Arterial stiffness indices are carried out to indirectly indicate the arterial stiffness without addressing the complexity of the cardiovascular system. Arterial stiffness can be expressed as arterial distensibility (its inverse), Young's modulus, PWV, Augmentation Index (AI), stiffness index (β), arterial compliance, etc.

PWV and AI have been commonly used to evaluate the arterial stiffness non-invasively. PWV represents the velocity of the pulse wave propagation through the arterial tree. The PWV is related to the elasticity of the arterial wall by the well-known Moens-Korteweg formula [3]:

$$PWV = \sqrt{\frac{E_{\theta\theta} h}{2 r_0 \rho_b}} \tag{1.1}$$

where $E_{\theta\theta}$ and $\rho_b$ are the effective incremental circumferential modulus and density of the arterial wall, respectively, $h$ is the arterial wall thickness, and $r_0$ is the radius of the arterial wall at diastolic pressure.

AI is another commonly used index to evaluate arterial stiffness. The arterial waveform is the combination of ejection and reflected wave at any location in the arterial tree. The pressure of the reflected wave is of great importance as it is obtained by assessment of the peripheral artery [13]. For example, the reflected wave from a radial artery (RA) is associated with aortic systolic blood pressure. The AI is calculated as the early wave reflection and the boost of pressure from systolic shoulder divided by the systolic pressure peak. Increased radial AI and carotid AI have been directly linked with risk factors on CVDs, such as diabetes, hypertension, and end-stage renal failure. Aortic AI is closely related to arterial properties by changing the PWV. The arterial stiffening causes an increased PWV, which in turn results in the early return of the reflected wave from the peripheral reflecting sites to the heart [14].

Other than arterial wall elasticity, arterial wall viscosity (i.e., damping) is of great importance to the cardiovascular system [15]. Wall viscosity is related to collagen and smooth muscle content [5]. The wall viscosity dampens the pulsatile forces of cardiac contraction to the arterial wall and impedes wall distension due to the time limit for distension [16, 17], and this is also indicative of the cardiovascular system condition.

Arterial wall radius is the key determinant of vascular resistance. Systematic vascular resistance (SVR) is indicative of cardiovascular compensation to maintain physiological homeostasis [18], peripheral arteries are the dominant factors in determining SVR, due to their small dimensions [18]. PVR is the effect of the vessels resisting flow and is primarily a function of vessel size and numbers of the vessel open. It can be calculated as mean arterial pressure (MAP) divided by cardio output (CO). Meanwhile, the Cardiac Output (CO) is calculated as CO = SV×HR [L/min], SV is stroke volume, HR is heart rate.

## 1.2 Traditional Techniques for Estimating Arterial Wall Parameters

### 1.2.1 Current Instruments for Arterial Pulse Measurement

Instruments need to be used to obtain arterial pulse waveforms and related parameters, such as blood pressure, arterial radius, and arterial wall thickness. There are numerous devices invented in history for blood pressure monitoring and obtaining arterial pulse waves. Blood pressure measurements are critical to the assessment of cardiovascular and health condition. Cardiac catheterization is the golden standard to evaluate the central pressure waveform invasively by a direct intra-arterial measurement in clinical practice. A catheter is implanted into the brachial or radial artery through the skin toward the heart and connected through fluid manometer tubing to a pressure transducer. However, a skilled technician and medical imaging instruments with high resolution are required to locate the arterial sites accurately. The procedure may pose a risk of injury, such as bleeding, bruising, and infection. Moreover, it is impossible for repeated measurement in an individual's daily life [19]. Thus, the indirect and noninvasive methods of arterial pulse measurement based on measuring the counter pressure are commonly used currently. Noninvasive arterial pulse measurement on peripheral arteries has been down recently, the central pressure waveforms are reconstructed through mathematical algorithms [20].

For centuries the arterial pulse waves monitored by contacting with different arterial sites of the body, such as the brachial artery (BA), RA, femoral artery (FA), carotid artery (CA), superficial temporal artery (STA), and dorsalis pedis artery (DPA). The first noninvasive measurement of blood pressure was invented in 1855. Then, the method has been improved by Etieene Jules Marey et al., who developed an RA sphygmomanometer [21]. A Russian doctor Nikolai Korotkoff established the basics of modern auscultation measurement of blood pressure in 1905. He used a stethoscope to specify the blood flowing sound generated by the arteries at

different cuff pressures [22]. The auscultatory measurement was further developed by Riva-Rocci and Korotkoff at the beginning of the 20$^{th}$ century. A cuff situates at the upper arm, and a stethoscope is placed over the artery under the pressure cuff. The technique is performed by deflating the cuff until the first sound is heard, then flattening again until the sound disappeared. Finally, the measurement results are indicated by the mercury column [23]. In the early 70s, the oscillometric devices were developed by digital processing of pressure oscillations transmitted from the arteries to the cuff [24].

Applanation tonometry was first presented by Pressman and Newgard in 1963 [25]. This method can noninvasively and continuously obtain pulse pressure alterations in a superficial artery, for example, RA and CA. The subjects are required to remain still while the measurements are performed by a technician. The pulse measurement is performed by applying force over a superficial artery to flatten the artery until the blood vessel starts distorting. The piezo-resistive pressure transducer on the probe captures the pressure change. The transducer captures the vertical displacement; then it is translated into electrical signals, which are proportional to the arterial pressure. The intra-arterial pressure is treated as perpendicular to the surface and the circumferential tension is negligible in the flattened segment [26]. The instrument is considered as correctly positioned at the arterial site by reaching the strongest level of the pulsation. The probe with a sensor array may provide more accurate results by optimizing the location at the arterial region. This method is facilitated by cuff-based devices to calculate absolute pulse pressure. Other errors may occur, such as device positioning for accuracy and reproducibility, device calibration, and motion artifacts. [26]. This method is also less accurate for obese subjects because of the thicker overlying tissue between artery and skin. Thus, it weakens the signal transmission between the artery and the probe.

The volume-clamp measurement was introduced by Penaz in 1969 [27]. The method is performed by placing a small cuff incorporating a photoplethysmography (PPG) device around a finger. PPG device is widely used in clinical studies to monitor peripheral circulation, HR, large artery compliance and oxygen saturation. The device consists of a red or infrared light emitting diode (LED) and a photodetector. The light is emitted from the LED (spectrum: ~650-800nm) to the skin, and the photodetector receives the intensity change of the light. The changes include orientation of red blood cells and variations in blood flow, blood volume, and arterial wall movement. A conventional pulse oximeter is used to monitor the changes in light absorption [28]. Recently, devices based on volume-clamp methodology have been developed, such as the Portapres and Finometer (Fianpres Medical Systems, Holland), the Task Force Monitor system (CNSystems Medizintechnik, GmbH) and the ccNexfin (Edwards Lifesciences, California, USA).

Biomedical imaging devices, such as Ultrasound and Magnetic Resonance Imaging (MRI), are commonly used nowadays for measuring the smallest biological structures, lumen diameter, PWV, blood flow, arterial distensibility, and plaque morphology [29]. In the 1930's, the ultrasonic imaging method emerged into the world as an instrument for physical therapy. Now, it is used in a variety of applications, such as tissue characterization and assessment of the cardiovascular system. The pulse-echo technique for this method is performed by generating acoustic waves (frequency, 2-15MHz or higher) via piezoelectric elements, which converts electric signals into mechanical vibrations. The ultrasound waves propagate through different tissues and finally return to the transducer as reflected echoes [29]. The well-known type is B-mode imaging, it can be used for acquiring arterial distension waveform, arterial wall texture, and elasticity features of the arterial wall with algorithms [30]. Moreover, the development of pulsed Doppler ultrasound techniques can provide information on blood velocity at specific

arterial sites within a large artery [29]. MRI provides valuable information on the arterial wall with high spatial resolution. It can monitor the small plaques, for example, a lipid core inside the arterial wall, to predict future cardiovascular events, such as heart attacks and strokes. It is found to be a valuable tool for diagnosing the early stage of cardiovascular risk for patients [31].

### 1.2.2 Current Methods for Estimating Arterial Wall Parameters

Arterial wall parameters, especially elasticity (related to arterial stiffness) and radius, can be evaluated by the imaging method with an instrument mentioned above or model-based analysis. Three major methods are involved: the measurement at the local site of an artery, the measurement between two arterial locations, and model-based systemic estimation at several sites along the arterial tree [32].

#### 1.2.2.1 Local Measurement

The arterial stiffness at a specific artery is evaluated by estimating cross-sectional arterial distensibility, which is the relative change in arterial diameter (area) for a known pressure change in an artery [32]. Typically, the measurement system is based on a vascular echo-tracking device, such as ultrasound by the Doppler shift principle or MRI by echo imaging method. The measured stress (the internal pressure) and the strain (arterial diameter or area) support the estimation of parameters by drawing a stress-strain curve. Some researchers used Bramwell-Hill for calculating local PWV. It is an extension of the Moens-Korteweg equation, which mainly focuses on the arterial pulse propagation in the cardiovascular tree based on hemodynamic blood flow. An expression of Bramwell-Hill is:

$$c = \sqrt{\frac{\Delta P \cdot V}{\rho \cdot \Delta V}} \tag{1.2}$$

where, $\Delta P$ is a change in blood pressure, $\Delta V$ is a change in arterial volume relative to volume $V$, and $\rho$ is the density of blood.

Numerous studies have investigated arterial wall properties via the stress-strain curve to characterize the viscoelasticity of the arterial wall locally using the instruments as mentioned earlier. By treating the arterial wall as a purely elastic or viscoelastic material, models for characterizing its mechanical properties are carried out, such as the hyper-elastic model, viscoelastic model, autoregressive model, and empirical nonlinear elastic models. The investigation focuses on *ex vivo* and *in vivo* experiments in ovine and human arteries. Jasso et al. [33] investigated the biomechanical properties of descending thoracic aorta and CA using linear and nonlinear viscoelastic models. The change of wall diameter of CA was captured by applanation tonometry and change of blood pressure was obtained by B-mode imaging, respectively [33]. The pressure-diameter loop is then drawn in the same graph to study the viscoelastic properties of the arterial wall. Shin et al. analyzed the first and second derivative of PPG waveforms and set up a proper model to extract pressure-related parameters. Then they assessed the derived indexes with experimental data [34].

1.2.2.2 Regional Measurement

The regional measurement for estimating arterial wall parameters is based on PWV. PWV is a valuable parameter for the determination of arterial stiffness, as well as a predictor for potential cardiovascular events. This method is conducted by capturing the two arterial pulse waveforms at a proximal and a distal arterial site simultaneously. The time delay in the wave propagation and the distance between the two arterial sites are used to calculate PWV.

There have been numerous studies that investigate PWV measurement by different means. Some use two sensors by a known distance over a segment of arteries, such as aorta-femoral PWV, carotid-femoral PWV, carotid-radial PWV, and finger-toe PWV, are commonly used in clinical experiments [35]. The two arterial waveforms can be obtained by an electrocardiogram

(ECG) with a pressure sensor, or an ECB with a photoplethysmography device, or applanation tonometry with an ultrasound instrument, or two applanation tonometry devices. The PWV is calculated as the length, $L$, divided by the time delay, $\Delta t$, between two arterial sites.

There are two commercially available devices commonly used in clinical studies: the Complior (Alam Medical) and the SphygmoCor (AtCor Medical New South Wales, Australia). The Complior measures the PWV between arterial sites: carotid and femoral artery. The SphygmoCor measures the PWV between R-peak from the ECG foot point of the carotid arterial pulse and the femoral arterial pulse.

1.2.2.3 Systemic Measurement

Pulse contour analysis has been used to evaluate the systemic arterial stiffness [36]. The Windkessel model and one-dimensional (1D) blood flow model combined with the mechanical model can describe changes in the cardiovascular system and estimate the arterial wall parameters.

Numerous models can be implemented in the estimation of arterial wall parameters based on theories of hemodynamics and material science. Windkessel model describes the hemodynamics of blood flow in the arterial tree in connection with resistance and compliance, which ignores the pressure wave propagation along the arterial tree [36]. In this model, the compliance of the central arterial system is represented by a compliance C and the peripheral arterial wall is modeled as a rigid tube with a constant resistance R. Another commonly used model, 1D blood flow model, explains the relationship between pressure propagation and blood volume flow in the cardiovascular system using Navier-Stokes equations. Several methods have been investigated in the literature to adapt the model for the the patient-specific condition, these methods can be grouped as [37] 1) fitting the model to a set of measurements, for example,

estimation of model parameters and 2) calibrating the wall models to subject-specific measurements at a specific arterial site. An accurate model for evaluating blood pressure and flow can be obtained from several segments of arteries along the arterial tree because the geometry changes are concerned with the model.

Liberson et al. proposed a model-based method with Navier-Stokes equations to assess arterial elastance and blood pressure from direct measured PWV [38]. Furthermore, numerous models with viscoelastic wall model, such as Fung's quasilinear viscoelastic model, have been proposed in the literature to estimate the mechanical properties of the arterial walls. Menacho et al. [39] focused on modeling the propagation of pressure waves along a viscoelastic pipe using the Maxwell and the Zener models. Ghigo et al. analyzed a nonlinear Kelvin-Voigt wall model to study the viscoelasticity of the arterial wall in the waves propagated along a sheep's arterial network [40]. Lungu et al. [41] predicted the mechanical properties of the pulmonary artery based on Windkessel and 1D blood flow model of the blood flow and wall motion measured by MRI. These complex models, either tested *ex vivo* or *in vivo*, require the measurements at arterial segments and selection of proper models under linear or nonlinear assumptions.

### 1.3 Motivation

CVDs are the primary cause of death in the world. Pathological degradation of arterial walls by CVDs may have severe outcomes, such as heart attacks, hypertension, or stroke. Atherosclerotic plaques located in large or medium-sized artery cause arterial stiffening, which poses risks to individuals. When CVDs problems are detected too late, the best treatment time may be missed for an individual. The changes in structure and composites of the arterial wall modify its mechanical property. Evaluation of its mechanical property indirectly via instruments can provide information for early diagnosis.

As discussed in Section 1.2.1, the current instruments for arterial pulse measurement have limitations [42]. Tonometry is a partly occlusive method for capturing arterial pulse waves, but it is highly sensitive to motion. It needs a continuous precise positioning of the sensor by a technician and the readout may be inaccurate for obese subjects. PPG devices are highly sensitive to movement, which makes their use in measuring signals during exercise difficult. It needs continuous supervision by a doctor. The cuff around the finger is still uncomfortable to the patient by poor blood circulation, and it is not suitable for placing it on damaged skin. Ultrasound and MRI can measure the blood flow and arterial radius in a minimal dimension, but they are expensive and complicated. Currently, health monitoring for a patient during a doctor visit is not a routine yet, because a lack of convenient diagnostic tools in their daily lives. Moreover, long-term continuous monitoring of an individual's health-related parameters is not only for optimized treatment of CVDs but for early diagnosis [43]. As such, there is a high demand for affordable sensors that allow untrained individuals to monitor their arterial pulse waveforms by themselves frequently.

Arterial wall parameters can be estimated with the methods as mentioned above in Section 1.2.2. However, those methods have limitations in estimating arterial wall parameters. The local measurement method reflects the arterial mechanical properties only locally. It requires local pulse pressure which can only measure in the brachial artery. Although local PWV measures the local change of arterial stiffness, its measurements demand user-unfriendly operation of complex instruments: imaging instrument for arterial radius waveform and tonometry for arterial pressure waveform [3]. Regional PWV over a long arterial trajectory (e.g., carotid-femoral) neglects the local change within the vasculature, suffers from errors in distance measurement, and only provides a gross regional measurement of arterial stiffness [44]. As the

gold standard for arterial stiffness, carotid-femoral PWV is obtained by measuring the pulse waveforms at carotid and femoral arteries simultaneously and calculating the time delay between the two pulse waveforms. High-quality transducers are needed to capture the arterial pulse waveforms for calculating the time delay. Also, it may be difficult to get accurate parameters from the subject with a high Body Mass Index (BMI).

To measure the elasticity and viscosity of the arterial wall, the arterial pulsatile pressure waveform and the arterial radius waveform need to be measured at the same arterial location simultaneously by two instruments (e.g., tonometry and imaging). The two measured waveforms are then plotted into a pressure-radius loop, from which the arterial wall elasticity and viscosity are extracted using the related machine-learning algorithms [15]. However, owing to the technical difficulty involved in its measurement, arterial wall viscosity has not been extensively studied for their clinical implications [5, 45].

As compared with SVR, peripheral Vascular Resistance (PVR) can be non-invasively measured and thus is more convenient for monitoring cardiovascular compensation. Contraction or dilation of peripheral arteries causes changes in PVR, but direct observation of arterial wall radius needs imaging instruments. Recently, a combination of a tactile sensor and a PPG sensor for acquiring two pulse signals (pressure versus radius) at an artery and system-identification algorithms for deriving PVR from the two signals tracked the change in PVR of a swine subject, which was introduced by infusion of norepinephrine [18, 46].

It is difficult to predict the pressure and blood flow along the arterial tree non-invasively, the model-based analysis can afford important information. Mathematical or computational modeling of the blood circulation is now used in the analysis of conditions and pathologies associated with CVDs. Zero-dimensional Windkessel model and 1D blood flow model are the

two models that have been extensively analyzed to derive the pressure and wave propagation relationship for further evaluating arterial stiffness [47]. These models treat the arterial wall as an elastic material and assume that the pressure is proportional to the cross-section area of the artery. However, limited parameters are estimated by Windkessle models because the whole artery is reduced to a single point. The mechanical models can be described in relaxation, creep, and recovery owing to the viscoelastic characterization of the arterial wall. The stress (pressure) as input and strain (relative change in radius) as output are plotted in the same graph for mechanical modeling of a viscoelastic material. Although some studies combined the 1D blood flow model and a mechanical model to solve the problem in estimating arterial wall parameters, the systemic evaluation is time-consuming and requires complex algorithms. Thus, it is unsuitable for an untrained individual to use at home.

In this dissertation, a model-based method was implemented in estimating arterial wall parameters from the measured signals via a microfluidic-based tactile sensor. A 5×1 transducer array built on a Pyrex/polyethylene terephthalate (PET) substrate is embedded into polydimethylsiloxane (PDMS) microstructure for capturing arterial pulse signals. The fabrication process for the sensor built onto a Pyrex substrate is previously developed by our group [48]. The developed tactile sensor features simple design and fabrication, low cost and performance robustness. A tactile sensor built on a PET flexible substrate was developed for health monitoring [43], which shares the same design as a Pyrex-based sensor. The performance of the sensor on arterial pulse monitoring was investigated by extracting tonometric parameters and calculating PWV and AI from five subjects at RA and CA. The repeatability of the sensor on arterial pulse measurement was also assessed. The factors, such as hold-down pressure (HDP), sensor sensitivity, and intra-subject variation, may affect the measured results. A method was

developed to enhance the sensor-artery interaction, particularly for the subjects with high BMI. A model-based analysis of arterial wall parameters from the measured pulse signals was proposed. The ultimate goal of this study is to offer a method to evaluate the arterial wall parameters non-invasively via a tactile sensor for at home monitoring.

The model-based method for estimating the arterial wall parameters is realized by combining the dynamic model with the hemodynamic model. The changes in the arterial wall parameters at rest and post-exercise serve as a better assessment of cardiovascular health. The t-test is utilized to statistical analysis of changes in arterial wall parameters from the measured signals before and post-exercise. The improvement of sensor-artery interaction is tackled by adding conformal layers with different stiffness and thickness without changing the fundamental design of the sensor. The estimated arterial wall parameters are compared with the measured results from a medical instrument.

**1.4 Objectives**

This dissertation aims to develop model-based analysis for estimating arterial wall parameters from noninvasively measured signals via a microfluidic-based tactile sensor. To implement the model-based method, the starting point is to design, fabricate, characterize, and apply a tactile sensor for obtaining arterial pulse waveforms. By holding the sensor toward the arterial sites, the arterial pulse causes sensor deflection, which is further translated to resistance change and recorded by the LabVIEW program. An algorithm is written to extract arterial pulse waveform and tonometric parameters. Next, owing to the time-harmonic nature of its radial motion, the arterial wall is modeled as a second-order dynamic system. By combining this dynamic model with a hemodynamic model of blood flow in the artery, the arterial wall parameters: elasticity, viscosity, and radius, were represented by spring constant and damping

coefficient. Then, the sensor is optimized with adding a conformal layer to improve the sensor-artery interaction. The measured results from a medical instrument is used as a reference.

To achieve our objective, we set some specific aims: (1) design and develop a microfluidic-based tactile sensor for arterial pulse measurement; (2) design and develop a model-based method for extracting the arterial wall parameters from measured arterial pulse signals; validate the proposed method for tracking changes in arterial wall parameters by moderate exercise; and (3) optimization of sensor design, improvement of sensor-artery interaction, and investigation of the influence of arterial wall parameters on sensor and subjects.

### 1.5 Dissertation Organization

This dissertation is arranged into seven chapters. This chapter (Chapter 1) presents a review of the clinical relevance of arterial wall parameters, current methods for estimation arterial wall parameters, and the motivation and objectives of this work. The organization of the remaining chapters is given below.

Chapter 2 describes the microfluidic-based tactile sensor used as the basis for collecting arterial pulse signals. This chapter includes the introduction of the sensor working principle, fabrication, and performance characterization. Additionally, technical issues associated with current methods that may be encountered in arterial pulse measurement are also discussed.

Chapter 3 focuses on the feasibility study of the tactile sensor for obtaining arterial pulse signals from different subjects at different arteries. Furthermore, data-processing algorithms for extracting arterial pulse waveform and tonometric parameters were presented. The calculated PWV and AI and extracted tonometric parameters from measured arterial pulse signal on five subjects at RA and CA were analyzed and compared.

Chapter 4 includes a detailed analysis of the model-based method for estimating arterial wall parameters. The 1D governing equations of axial blood flow in the artery and the constitutive equation of the arterial wall were re-examined, and the governing equations for the radial and longitudinal motion of the arterial wall with consideration of their coupling were derived. Owing to the time-harmonic nature of its radial motion, the arterial wall is modeled as a second-order dynamic system. Key equations for estimating arterial wall parameters were derived in this chapter by combining dynamic model with a hemodynamic model of blood flow in the artery.

Chapter 5 describes the application of the model-based method for estimating arterial wall parameters from measured signals on subjects at different arteries. First, the estimated parameters from the measured pulse signals on seven subjects at rest were analyzed. Due to the sensor-artery interaction that varies with arteries and subject-specificity, the measured value is not suitable for comparison. Next, the change in arterial wall parameters via moderate exercise is introduced. The change in the arterial wall parameters from measured signals on five subjects at rest and post-exercise were statistically analyzed.

Chapter 6 studies the performance of optimized sensor design with a conformal layer for improving sensor-artery interaction and its influence on estimation of arterial wall parameters. Three factors that may influence the arterial pulse measurement were described. A method for improving sensor-artery interaction was introduced to accommodate the sensor for practical use in different subjects. The estimated arterial wall parameters from arterial pulse signals measured on six subjects at rest via the sensor with different conformal layers were compared. Meanwhile, two subjects require to do moderate exercise, the estimated arterial wall parameters before and post-exercise were compared with the measured results from a medical instrument.

Chapter 7 provides the achievements and highlights the limitations of this work by giving some directions for future study on estimating arterial wall parameters.

# CHAPTER 2

# A MICROFLUIDIC-BASED TACTILE SENSOR

This chapter presents a microfluidic-based tactile sensor used as a basis for arterial pulse measurement. The tactile sensor consists of a PDMS microstructure embedded with a $5 \times 1$ transducer array built on a Pyrex or PET substrate. The details of sensor design and fabrication process for the microfluidic-based tactile sensor built on a Pyrex substrate can be found in our previous publications [48, 49]. The fabrication process for PET-based tactile sensor is described below as a new contribution to this work. Both Pyrex-based and PET-based tactile sensors are developed for capturing arterial pulse signals. A brief introduction of the tactile sensor will be described in this chapter, which includes the sensor design, working principle, fabrication, and characterization. The associated technique issues occurred in sensor fabrication and the practical use of the sensor for arterial pulse measurement will be discussed.

## 2.1 Sensor Design, Working Principle and Fabrication

Configuration and working principle of the tactile sensor are depicted in the pictures (Figure 2.1). Built on either a flexible PET slide or a rigid Pyrex slide (75mm×25mm) with five electrode pairs, the microfluidic-based tactile sensor comprises of a 1mm-thick PDMS microstructure embedded with a microchannel (cross section: 1mm×80μm) underneath. A set of five Indium tin oxide (ITO)/Au electrode pairs on the PET/Pyrex substrate are evenly distributed along the microchannel length. The portion of electrolyte between an electrode pair functions as a resistive transducer, whose resistance varies with the geometry of this portion of electrolyte and is routed out by the electrode pair. Thus, one body of electrolyte and five electrode pairs form a 5×1 transducer array underneath the microstructure. The transducer array spans 6mm and has a spatial resolution of 1.5mm. Key design parameters and their values of the microfluidic-

based tactile sensor are exhibited in Table 2.1. An external pressure acting on the microstructure translates to distributed deflection of the microstructure at the top of the microchannel and thus geometrical reduction of the microchannel along its length, which registers as resistance changes at the locations of the transducers [43].

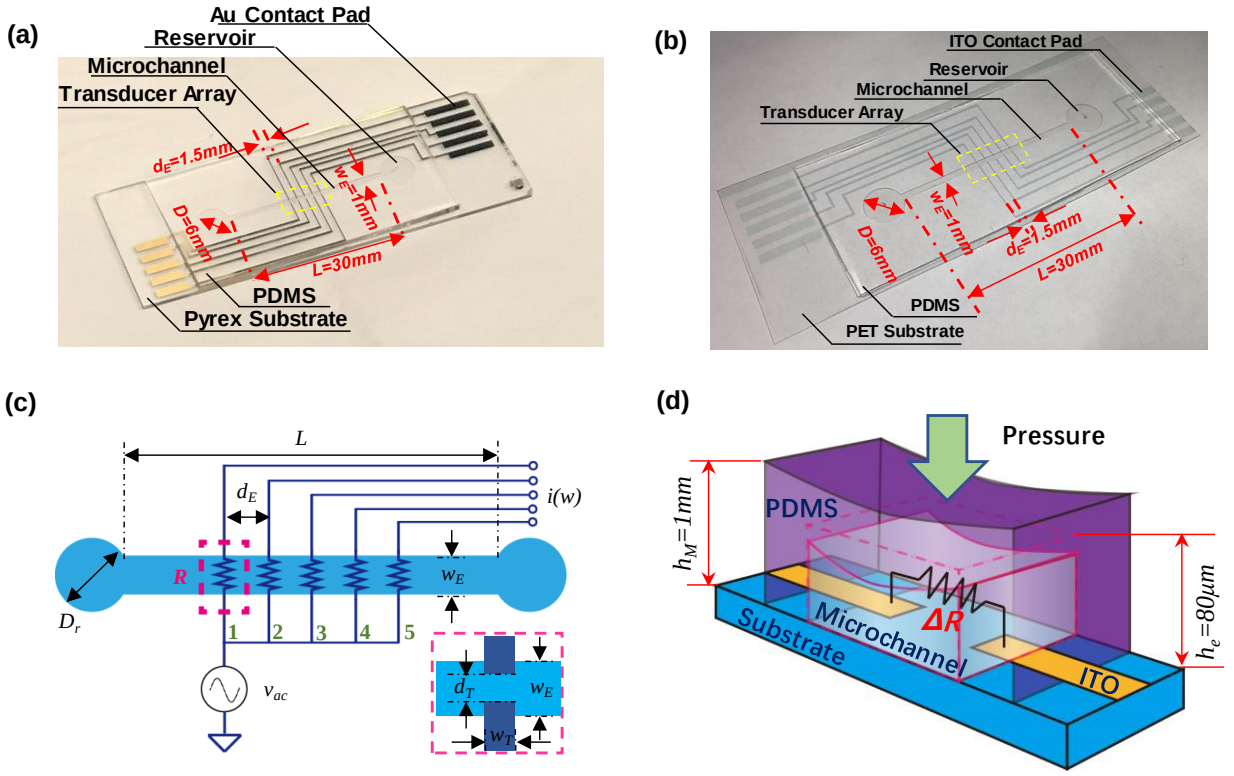


Figure 2.1 Microfluidic-based tactile sensor for arterial pulse waveform measurement: (a) tactile sensor built on Pyrex substrate; (b) tactile sensor built on PET substrate; (c) resistive transducer array realized by the electrolyte in the microchannel and five electrode pairs, with the transducers labeled by numbers; (d) working principle (out of proportion for clear illustration).

To monitor resistance changes in the transducer array, a function generator is used to apply an Alternating Current (AC) signal (100kHz, peak-peak amplitude: 200mv) as the input signal for all the transducers (Figure 2.1c). The output of a transducer is connected to its electronics implemented on PCB for both amplifying the AC signal coming out from the transducer and converting the AC signal to a Direct Current (DC) output, which is recorded by a

LabVIEW program. Note that the same design of electronics is used for all the transducers, but they are implemented on separate PCBs. The detailed circuit design can be found in our previous work [48, 49].

Table 2.1 Key design parameters and their values of the microfluidic-based tactile sensor.

| Key Parameters | Symbol | Value |
|---|---|---|
| Microchannel width | $w_E$ | 1mm |
| Microchannel height | $he$ | 80μm |
| Microchannel length | $L$ | 30mm |
| Reservoir diameter | $D$ | 6mm |
| Transducer resolution | $d_E$ | 1.5mm |
| Distance between electrodes | $d_T$ | 400μm |
| Transducer width | $w_T$ | 200μm |
| Microstructure thickness | $h_M$ | 1mm |

The sensor built on a Pyrex substrate is fabricated by photolithography techniques, which can be found in our previous publication [48, 49]. The electrolyte 1-ethyl-3-methylimidazolium dicyanamide (EMIDCA) is injected into the fabricated sensor built on a Pyrex slide. The fabrication process for PET-based sensor is described below using wet etching techniques. A low-cost, two-mask fabrication process for realizing the PET-based sensor is illustrated in Figure 2.2. The process starts with a commercial ITO/PET sheet (a 0.2mm-thick PET substrate coated with 120nm~160nm-thick ITO layer). To pattern ITO electrodes on the PET substrate, a 15μm-thick dry film (Alpho NIT 215, NichigoMorton Co., Ltd.) is laminated onto the PET substrate. Via the first mask, the electrode pattern is transferred to the dry film, which is followed by wet etching of the ITO layer to form ITO electrodes. Afterward, the dry film is removed using ethanol. Via the second mask, a SU8 mold is created on a Pyrex substrate. Then, a mixture of curing agent to PDMS elastomer with a weight ratio of 1:10 is poured over the SU8 mold. After being cured at room temperature over 24hrs, the microstructure is peeled off from the SU8 mold and a hole is punched into each reservoir using a needle [50].

To strengthen the bonding strength between the PDMS microstructure and the PET substrate with patterned ITO electrodes, a chemical gluing strategy is adopted. First, the photoresist is placed onto the microchannel of the microstructure. Then, the patterned ITO electrodes and the microstructure are activated with hydroxyl groups by an oxygen plasma treatment for 1 minute, which are followed by immersing the microstructure and ITO electrodes into 1% (v/v) 3-Glycidyloxypropyltrimethoxysilane (GOPTS) and 5% (v/v) 3-Aminopropyltriethoxysilane (APTES) for 20 minutes, respectively. Afterward, the microstructure is rinsed with acetone, isopropanol and DI water, and, sequentially, the PET substrate with patterned ITO electrodes is washed with ethanol and DI water. Finally, the microstructure and the PET substrate are aligned and bonded under a contact pressure at 100℃ for 5 minutes, then at 50℃ for 24hrs. Electrolyte, 1-ethyl-3-methylimidazolium tricyanomethanide (EMIM TCM), is injected into the microchannel via a reservoir using a syringe. Two reservoirs are then sealed with PDMS with a weight ratio of 1:10. Conductive epoxy is used to make electrical connection between the contact pads of the sensor and the associated electronics on PCBs [50].

The PDMS as a biocompatible material is contacted with the skin surface of an individual. For a safety concern and assure the sensor is well designed for experiments on subjects, the bonding strength between the PDMS microstructure and the substrate need to be assessed before any measurements. To validate the bonding strength of the device, which is critical for avoiding electrolyte leakage between the microstructure and the substrate, a peel-off test on the sensor is conducted as follows. The sensor is first soaked in isopropanol alcohol for 24hrs, and then the PDMS microstructure is peeled off with a tweezer. As shown in Figure 2.3, the majority of the PDMS microstructure remains on the surface of the PET substrate with ragged edges, indicating

that the bonding between the microstructure and the substrate is strong enough for supporting arterial pulse measurement.

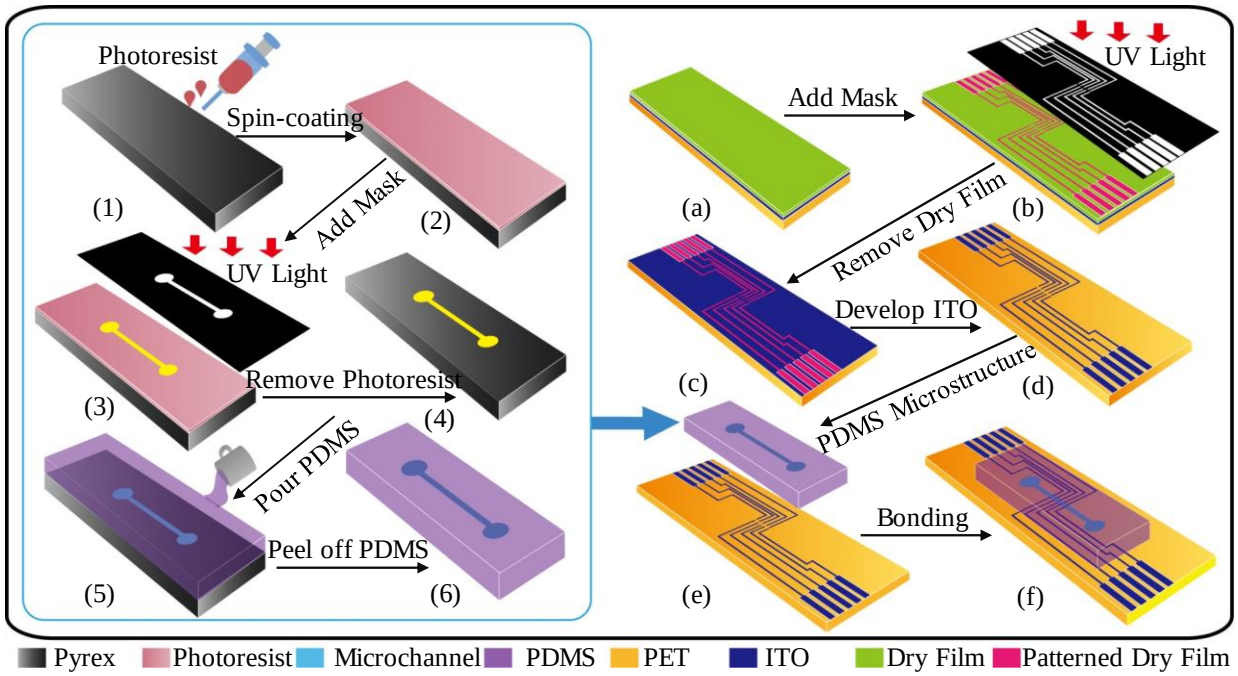


Figure 2.2 Fabrication process for the PET-based sensor. (1)-(6) fabrication process for PDMS microstructure with microchannel; (a) dry film lamination, (b) patterning of dry film under UV light, (c) patterned ITO electrodes, (d) develop ITO electrodes, (e) alignment and bonding with microstructure, (f) 3D view of the sensor.

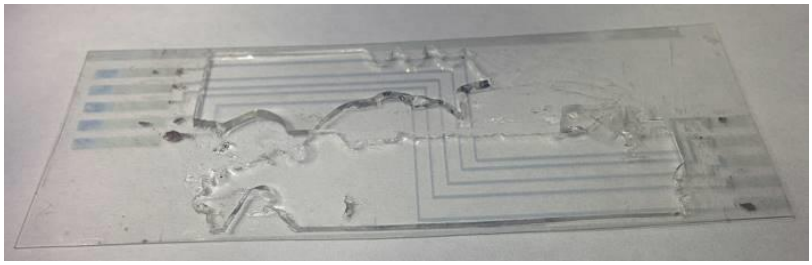

Figure 2.3 Picture of a fabricated PET-based sensor after a peel-off test being conducted.

## 2.2 Sensor Performance Characterization

The recorded parameter of a transducer is a DC voltage output, $V_{out}$, which is related to the resistance of a transducer by [48, 49]:

$$V_{\text{out}} = \frac{v_{pp}^2 R_F^2}{8R^2} \tag{2.1}$$

where $v_{pp}$ is the peak-to-peak value of the AC signal, and $R_F$ is the feedback resistance of the electronics used. Therefore, the resistance of a transducer can be obtained by:

$$R = \frac{v_{pp} R_F}{2\sqrt{2V_{out}}} \tag{2.2}$$

The bottom deflection at a transducer is represented by the resistance change:

$$\Delta R = \frac{v_{pp} R_F}{2\sqrt{2}} \left( \frac{1}{\sqrt{V_{out}}} - \frac{1}{\sqrt{V_{out0}}} \right) \tag{2.3}$$

where $V_{out0}$ is the DC voltage of a transducer, when it is free of deflection.

Owing to fabrication variation in transducer height, $h_e$, (the smallest design parameter), the original resistance (defined as the resistance of a transducer when it is free of deflection) may vary among the transducers. The original resistance of the $i^{th}$ transducer is roughly calculated as:

$$R_{0\text{-}i} = \frac{\rho \cdot w_e}{d_e / 2 \cdot h_{e-i}} \tag{2.4}$$

where ρ is the electrical conductivity of electrolyte, $d_e$, $w_e$ and $h_{e\text{-}i}$ are the length, width, and height of the $i^{th}$ transducer, respectively. The resistance of a transducer after being pressed against an artery is defined as its initial resistance, $R_{0\text{-}i}'$. As such, the resistance change is calculated relative to the initial resistance, instead of the original resistance:

$$\begin{aligned} \Delta R &= R_i - R_{0-i}' \\ &= \frac{\rho \cdot w_e}{d_e / 2 \cdot h_{e-i}'} \cdot \left[ \left( 1 - \frac{z_{s-i}}{h_{e-i}'} \right)^{-1} - 1 \right] \\ &= \frac{\rho \cdot w_e}{d_e / 2 \cdot (h_{e-i}')^2} \cdot z_{s-i} = \frac{(R_{0-i}')^2 \cdot d_e / 2}{\rho \cdot w_e} \cdot z_{s-i} \end{aligned} \tag{2.5}$$

where $z_{s\text{-}i}$ is the deflection for the $i^{th}$ transducer, $h_{e\text{-}i}$ is the initial height of the transducer.

According to Equation (2.5), the sensor deflection at the $i^{th}$ transducer can be obtained:

$$z_{s-i} = \frac{\Delta R}{(R_{0-i}')^2} \cdot \frac{\rho \cdot w_e}{d_e / 2} \tag{2.6}$$

The same experimental setup for characterizing the performance of Pyrex-based sensor [48, 49] is utilized to characterize the performance of PET-based sensor, which is shown in Figure 2.4. Briefly, a rigid cylinder probe is used to exert distributed load to the sensor, via a pre-defined probe displacement pattern. The resistances of the transducers are recorded using a custom LabVIEW program. Meanwhile, the overall load accompanying the probe displacement is monitored by a six-axis load cell (Nano 17, ATI INDUSTRIAL AUTMATION), which is attached on a micromanipulator (MP-285 motorized micromanipulator, SUTTER INSTRUMENT).

The resistance changes of the sensor and the overall load as a function of the probe displacement are plotted in Figure 2.5 (a) and (b). Since the probe is rigid, the probe displacement coincides with the deflection of the top surface of the PDMS microstructure in the sensor. The linear relation between the overall load and the deflection indicates that the microstructure works in the linear range. Resistance changes vary nonlinearly with the deflection of the microstructure in PET-based sensor when large probe displacement exerted on the top of the microstructure.

Response time determines how quickly the sensor responds to stimuli. The response of the sensor and the overall load as a function of time, in response to a step input of 100μm at a ramp-up speed of 3mm/s, respectively, shown in Figure 2.5 (d) and (e). These fluctuations are believed to result from the experimental noise. Evidently, the sensor responds to the step input as fast as the load cell used for load readout, with no noticeable time delay.

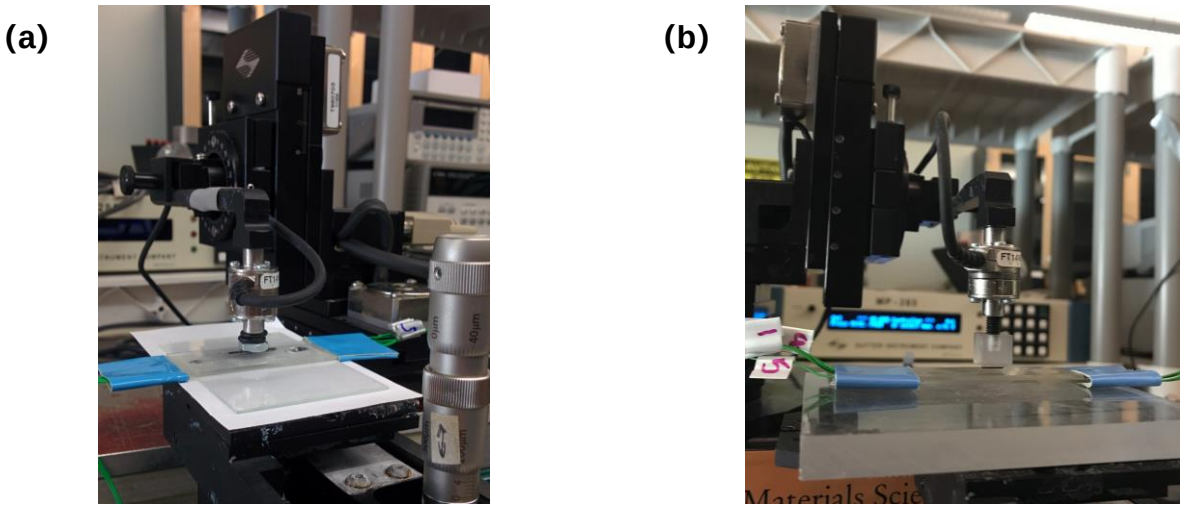


Figure 2.4 Experimental setup for characterization of (a) the PET-based tactile sensor and (b) Pyrex-based tactile sensor.

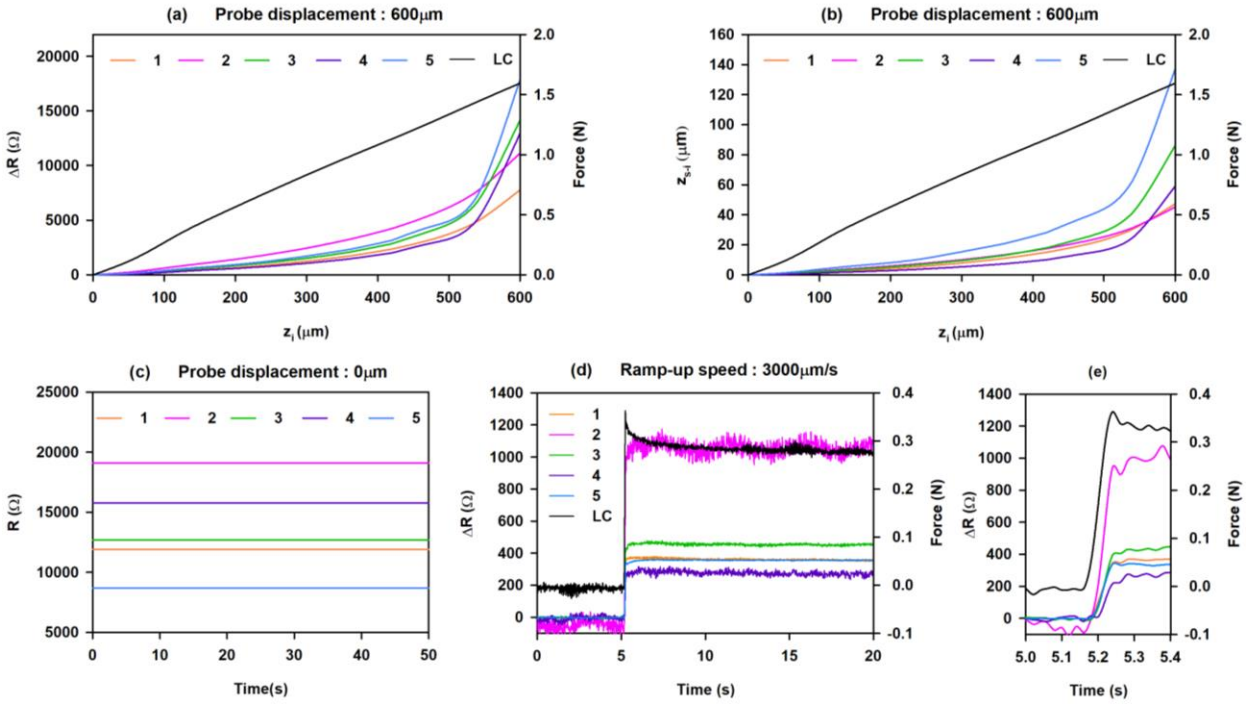


Figure 2.5 Resistance changes (a) and deflection (b) with the overall load of the PET-based tactile sensor as a function of the probe displacement. (c) Absolute resistance of the sensor free of displacement. (d) Resistance changes of the sensor and the overall load as a function of time, in response to a step input of 100μm at a ramp-up speed of 3mm/s, (e) zoom in picture of (d).

## 2.3 Technical Issues

The performance characterization of the sensor indicates its potential capability for capturing arterial pulse signals. There are three technical issues that need to be considered for implementing the sensor for arterial pulse measurement.

### 2.3.1 Variation Between Transducers

There is a slight difference in readouts from the five transducers of a fabricated tactile sensor. It is difficult to keep an absolute uniform surface of SU-8 mold and maintain the same height during the fabrication process. Hence, the variation in the height of microchannel for PDMS microstructure occurs in the replica molding procedure via a SU-8 mold. Further, the variation of resistance among the five transducers is an indication of varying cross-sections of the microchannel. As shown in Figure 2.5 (c), the original resistance of the five transducers are slightly different from each other under free probe displacement. Because the resistance change will be used as the measured results from each transducer, this variation is trivial for arterial pulse measurement. In some cases, the normalized arterial pulse signals may be utilized to compare the difference in the extracted parameters from the measured arterial pulse signals on subjects. Therefore, the variation between transducers plays a relatively unimportant role during arterial pulse measurement.

### 2.3.2 Ease of Use and Robustness

The sensor would be able to withstand handling by technicians and untrained individuals or patients for arterial pulse measurement. Motion artifact caused by the handing, shaking, or moving is inevitable during a pulse measurement. An effective algorithm for canceling this effect can enhance the accuracy and reliability of the sensor for extracting arterial pulse waveforms from measured signals. The PDMS microstructure is in contact with the arterial region owing to

its biocompatibility. The electrolyte inside the microchannel must be ensured without leakage for alleviating safety concerns. The electrodes for routing electrical signals of the sensor must be covered with non-conductive duct tape.

The physiological condition varies from subjects under different conditions, for example, exercise, then the sensor must be robust to variations. The sensitivity of the sensor must be high enough to meet the requirements under a dynamic situation. The sensor has potential in clinical trials. The repeatability of the sensor is critical and it must be evaluated for long-term reliability.

### 2.3.3 Interaction Between Sensor and Artery

The blood flow drives pulse waves to propagate along the radial and longitudinal direction through the arterial wall, connective tissue, transmit to the skin surface, then captured by the developed microfluidic-based tactile sensor. The blood pushes the inside of the arterial wall in the radial direction and the pressure exerts on the skin surface toward the arterial region making the overall system challenging in the practical use. The mechanism behind this propagation requires systematic study to provide a fundamental model for investigating the measured results from different subjects.

The sensor design requires to accommodate subject-specificity, such as BMI, to enhance the interaction between sensor and artery. The non-flat, curved surface of the human body may alter the measured results. The proposed sensor with five transducers can reduce this effect. While the arteries are different in size, depth from skin surface, mechanical properties, and length from the heart, the sensitivity of a sensor may affect the analysis of arterial pulse signals. Sensor design and optimization improve the sensor-artery interaction, especially in those who have thicker overlying/connective tissue.

The measured signal is a combination of motion artifacts, respiration, and the arterial pulse signal. These factors may affect the sensor-artery interaction. It is desired to be able to operate the sensor by untrained individuals and still get reliable results. The pressure exerted on the sensor may vary with time and may be affected by respiration. Thus, the effect of hold-down pressure needs to be studied.

## 2.4 Conclusion

In this chapter, the design, working principle, and performance characterization of the Pyrex-based/PET-based tactile sensor for its potential use in arterial pulse measurement were presented. A simple and cost-effective fabrication process for PET-based sensor was demonstrated. A cylinder probe was used to exert deflection on the top of PDMS at the transducer region for performance characterization. The fast response time and good dynamic performance prove its capability for tracking the rapid changes, such as arterial pulse signals. Technical issues associated with variation between transducers, ease of use and robustness, and interaction between sensor and artery for arterial pulse measurement were discussed. The variation of sensor readout in different transducers results from variability in sensor fabrication, which plays a relatively minor role in the measurement. Applying the sensor for arterial pulse measurement requires to consider the safety, repeatability, liability, and motion artifact. The interaction between sensor and artery affects the measured results, which needs to be studied in different perspectives. Factors, such as pressure exerted on the sensor, subject specificity, and respiration, may be taken into consideration in data analysis. The sensor design needs to be optimized to accommodate the change of arterial condition in subjects.

# CHAPTER 3

# EXTRACTION OF ARTERIAL PULSE WAVEFORM AND KEY PARAMETERS FROM MEASURED PULSE SIGNALS

This chapter describes the experimental setup, measurement protocol, and signal-processing algorithms for extracting arterial pulse waveforms and parameters from measured signals on five subjects. The working principle, procedure, and measurement method of the sensor on capturing the pulse signals are presented. The performance of the tactile sensor on arterial pulse measurement is evaluated from several perspectives, such as extraction of tonometric parameters, calculation of PWV and AI, and examination of the repeatability. The extracted key parameters from the measured signals on five subjects at RA and CA are analyzed.

## 3.1 Measurement Protocol and Signal Acquisition System

### 3.1.1 Measurement Protocol

Arterial pulse signals are measured on the following five subjects: 28yr-old female (28yr-F), 29yr-old female (29yr-F), 28yr-old male (28yr-M), 42yr-old female (42yr-F), and 50yr-old male (50yr-M). The same PET-based tactile sensor is used to measure the radial and carotid pulse signals on the right side of a subject. All the measurements are conducted in a quiet and temperature-controlled (~24°C) room. Before measuring the pulse signal, a subject is required to take a 30min rest. During pulse measurement, the subject needs to keep calm and remain still in a sitting position. Each measurement takes approximately 1min. The subject may feel slight pressure at the artery region; it is similar to pulse-taking by a nurse during a doctor visit. This small amount of pressure is aimed to get the pulse signal in the artery transmitted to the sensor. Then the investigator holding the sensor with two fingers also needs to remain still until the measurement is finished, so that the sensor position and finger positions are unchanged. These

protocols are mainly aimed at minimizing motion artifacts in a recorded pulse signal [43]. At any given time, the same sensor is used to measure the radial and carotid pulse signals on the right side of a subject. Thus, the measurement at the carotid artery in the neck will not affect the subject's respiration. To measure the carotid-radial PWV, the pulse signals at the carotid and radial arteries of a subject need to be recorded simultaneously on one side of the body. Another sensor with the same design is brought in for this purpose.

As illustrated in Figure 3.1, the sensor is placed on either the RA or the CA and two fingers are used to hold the sensor and press the sensor against the artery for acquiring its pulse signal using PET-based tactile sensor. Owing to the small curvature of the wrist and the neck, the sensor is bent slightly due to the hold-down pressure applied for measuring a pulse signal. Despite being not very flexible, the ITO electrodes do not suffer from cracks and compromise the quality of the measurement. In this work, the hold-down pressure against an artery is roughly controlled by varying the finger-holding strength. Although hold-down pressure cannot be quantitatively controlled by the fingers, it does serve well the purpose for an untrained individual to use this sensor as a point-of-care diagnostic tool whenever needed.

As illustrated in Figure 3.2, the Pyrex/PET-based tactile sensor should be placed on an artery with its transducer array normal to the artery for recording its pulse signal. The mean diameter of the right RA is 2.3±0.4mm [51], and the mean diameter of the CA is 6.10±0.80mm in women and 6.52±0.98mm in men [52]. The 6mm-long and 1.5mm-resolution transducer array allows an untrained individual to easily align at least one transducer at the site of an artery. Then, the arterial pulse sends a time-varying load on the top of the microstructure and registers as a resistance change by the transducer at the artery site. The resistance changes are captured by the sensor via LabVIEW programs.

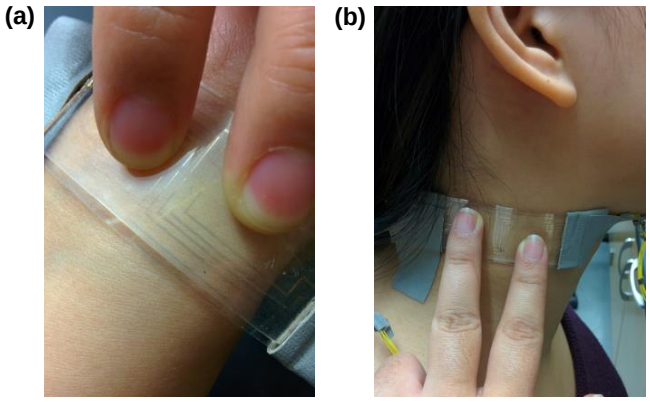


Figure 3.1 Photographs of the sensor for measuring the (a) radial and (b) carotid pulse signals on the right side of a subject with two fingers on top of the PET substrate.

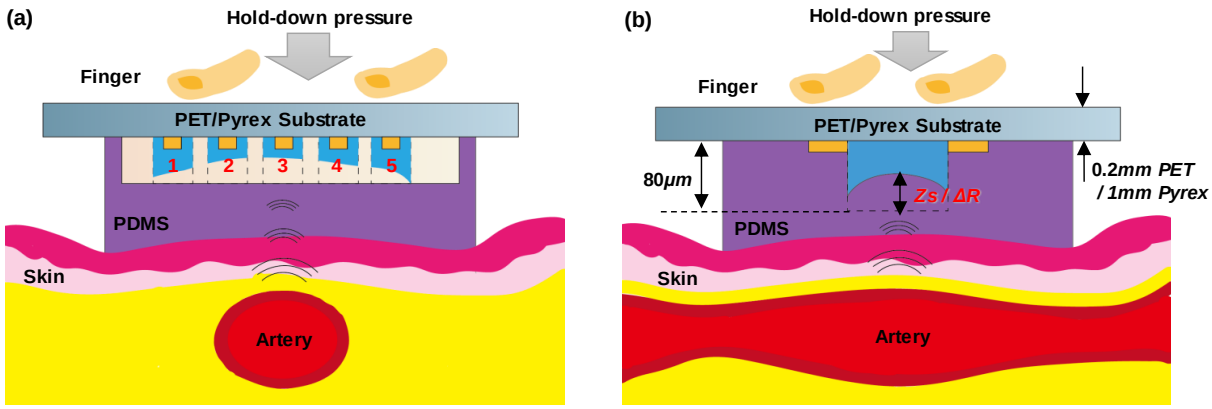


Figure 3.2 Rationale for arterial pulse measurement: an arterial pulse signal deflects the microstructure and registers as a resistance change by the transducer at the artery site. (a) The transducer array is aligned normal to the artery (b) Hold-down pressure influences the sensor-artery interaction and blood flow at the artery.

### 3.1.2 Signal Acquisition System

The signal acquisition system for recording a pulse signal as a resistance signal via the Pyrex/PET-based tactile sensor is illustrated in Figure 3.3. To monitor the resistances of the transducer array, a high-frequency AC voltage (100kHZ, Vpp: 200mv) signal from the function generator serves as the input of the transducer array. The other side of the transducers serve as outputs for the sensor, which are connected to electrical components. Connected to DC power

supplies, interface electronics implemented on Printed Circuit Board (PCB) are used to amplify and demodulate the output of a transducer, which further feeds into a LabVIEW program for real-time examination via a DAQ (Data Acquisition) board [43]. The sampling frequency is 1kHz, which is high enough to obtain the key feature of a pulse signal. The original measured data from LabVIEW are further processed by Matlab algorithms for de-noising, extracting arterial pulse waveforms, and extracting key parameters.

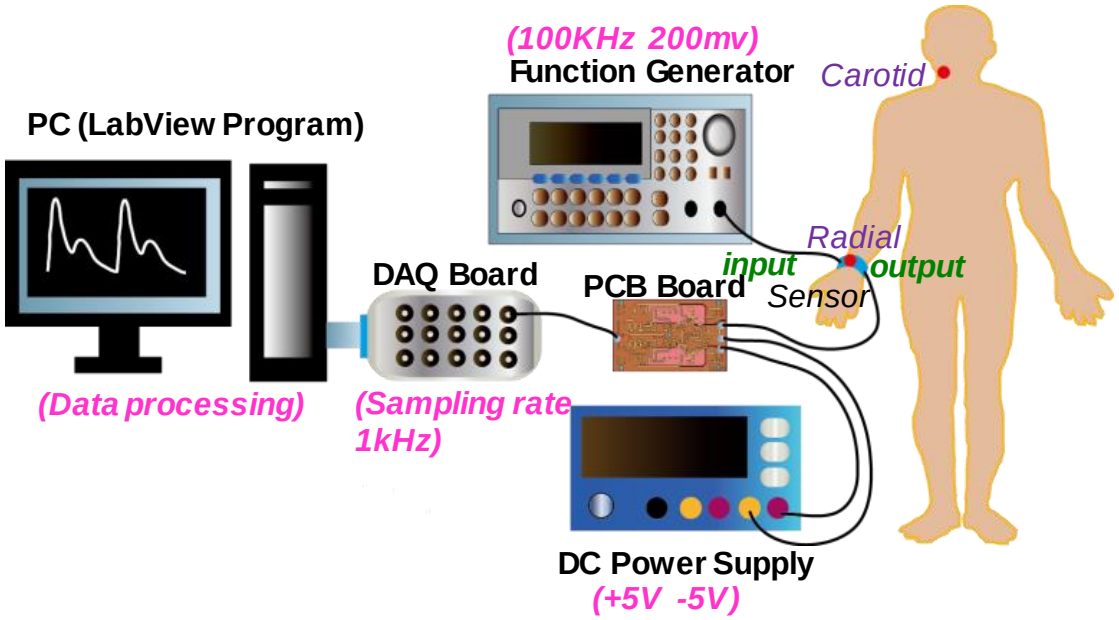


Figure 3.3 Experiment setup of measuring an arterial pulse signal via the tactile sensor, with the signal flow of one transducer being illustrated.

**3.2 Data-Processing Algorithms for Extracting Pulse Waveform and Key Parameters**

3.2.1 Extraction of Arterial Pulse Waveforms

Motion artifacts (i.e., fluctuation of the initial resistance over time, motion of the sensor and the respiration and body motion of a subject during measurement) can introduce baseline drift to a recorded pulse signal. The Discrete Meyer Wavelet Transformation (DMWT) and Cubic Spline Estimation (CSE) has been proven to be very effective in removing baseline drift

from the recorded data. In this sense that this algorithm has the capability of restoring a pulse signal recorded when a subject is breathing heavily post-exercise.

The originally recorded data for a pulse signal via the sensor is the resistance, *R(t)*, of a transducer as a function of time, as shown in Figure 3.4 (a). When the sensor is not placed on an artery (i.e., free of load), the height of a transducer is defined as the original height, $h_e$ [43]. Owing to fabrication variation, the original height varies among the transducers. Its resistance is

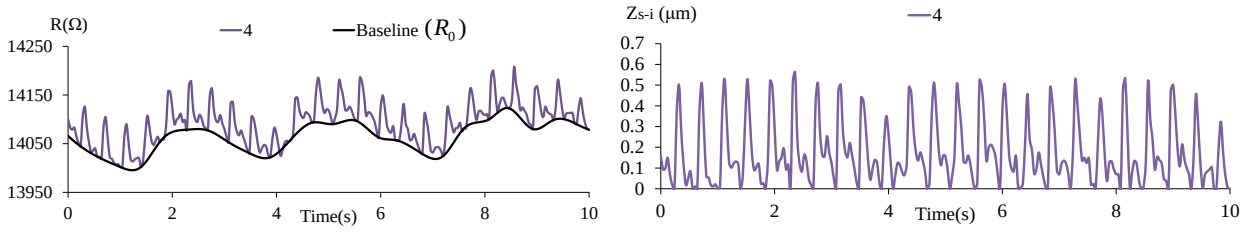


(a)




(b)

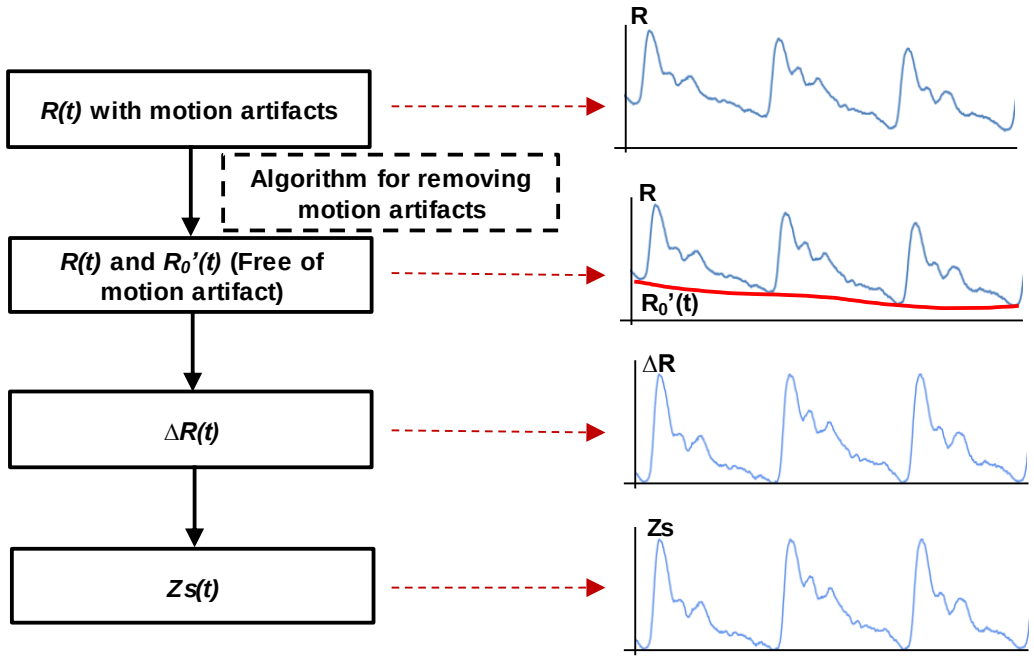


(c)

Figure 3.4 Demonstration of signal-processing algorithm using DMWT and CSE for a recorded pulse signal (a) absolute resistance, *R*, with estimated baseline (or estimated initial resistance, $R_0$); (b) drift-free sensor deflection representing the pulse waveform; (c) steps for obtaining the drift-free pulse waveform from an originally recorded pulse signal.

defined as the original resistance, $R_0$. The corresponding resistance of the transducer is defined as the initial resistance, $R_0'$. Thus, the resistance change ($\Delta R=R-R_0'$) of a transducer relative to its initial resistance, instead of its original resistance, corresponds to the sensor deflection caused by a pulse signal. The signal processing steps for obtaining the de-noised, drift-free pulse signal is demonstrated in Figure 3.4 (c) and the drift-free signal is shown in Figure 3.4 (b).

### 3.2.2 Tonometric Parameter Extraction from Arterial Pulse Waveforms

The key tonometric parameters of a pulse cycle are defined in Figure 3.5 (a). H1 and H5 are the systolic peak and diastolic peak, respectively. The ratio of systolic peak and diastolic peak (H1/H5) bears physiological significance and thus is extracted from a pulse signal here. The upstroke time, t1, is the duration between onset and the systolic peak. While the systolic time, t2, is the duration between onset and the diastolic notch (or incisura), the diastolic time, t3, is the duration between the diastolic notch and end. The duration of one pulse cycle is T [43].

As shown in Figure 3.5 (b), one algorithm is written in Matlab to extract these tonometric parameters, where findpeaks function is repeatedly used in different settings to obtain desired tonometric parameters. First, findpeaks function is applied to a pulse signal to find the location and the value of H1 of each pulse cycle in the pulse signal. By setting the pulse height right above the diastolic peak, the locations and the values of H1 and H5 in each pulse cycle are obtained. Then, setdiff function is applied to extract only the location and the value of H5 in each pulse cycle. To calculate the pulse duration, T, a pulse signal is multiplied by -1 and findpeaks function is applied to find the locations of the peaks, which corresponds to the onset of pulse cycles in the pulse signal. The time interval between two consecutive onsets is the pulse duration. Subtracting the location of the onset from the location of H1 in each pulse cycle gives rise to t1. To extract t2, a pulse signal is flipped by multiplied by -1. Findpeaks function is then applied to

the flipped signal to find all the locations of incisura, which is followed by applying findpeaks function to find the locations of all the onsets and the incisura. Then, t2 is extracted by applying setdiff function to the two sets of the peaks. Finally, t3 is calculated as T-t2. Note that a 10s pulse signal contains 10~15 pulse cycles. Each calculated tonometric parameter is the average value of all the pulse cycles of a 10s pulse signal [43].

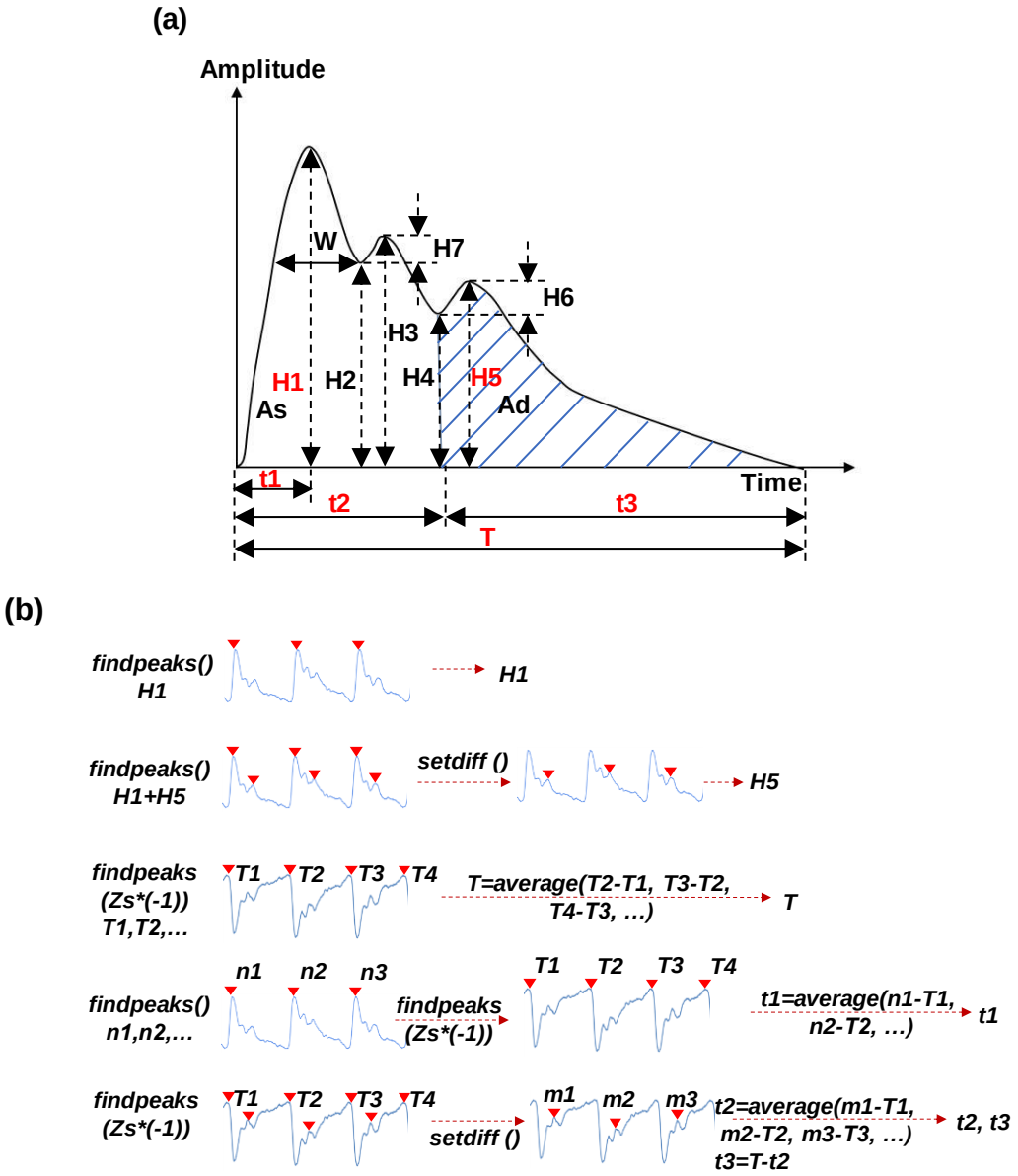


Figure 3.5 Key parameters of an arterial pulse waveform. (a) Tomometric parameters, (b) signal processing flow chart for extracting tonometric parameters from a measured pulse waveform.

## 3.3 Results

### 3.3.1 Measured Arterial Pulse Signals at RA and CA

To compare the measured pulse feature of the five subjects, the pulse signals are normalized by the sensor deflection divided by the amplitude of each pulse cycle. The normalized radial and carotid pulse waveforms measured via PET-based tactile sensor on the five subjects are illustrated in Figure 3.6. The signals from younger subjects, such as 28yr-M, indicate the lowest amplitude of diastolic notch at two arterial sites. The lowest heart rate also observed from the results since the male subject is physically active and do more exercise than other subjects. The signal from 29yr-F at CA is unclear compared with others; this may be related to her thicker connective tissue above the artery due to higher BMI.

The difference between radial and carotid pulse waveforms of a subject is compared. As illustrated in Figure 3.6, the diastolic notch in the radial pulse is deeper and smoother than the one in the carotid pulse; the upstroke swing is steep in the radial pulse, but is a little bit inclined in the carotid pulse. These two differences in the pulse shape between the radial and carotid pulses are consistent with the literature [53]. Furthermore, in the radial pulse waveform, the descending limb for the systolic peak is less steep than the ascending limb [53]. The duration of a pulse cycle stays the same at the radial and carotid arteries since the heart rate determines the pulse cycle duration.

Overall, the measured difference between radial and carotid pulse waveforms of a subject is consistent with the related findings in the literature, the difference in the measured pulse waveform among the subjects also reveals related physiological significance. The capability of the sensor for measuring the arterial pulse signals at different arterial sites on different subjects is validated.

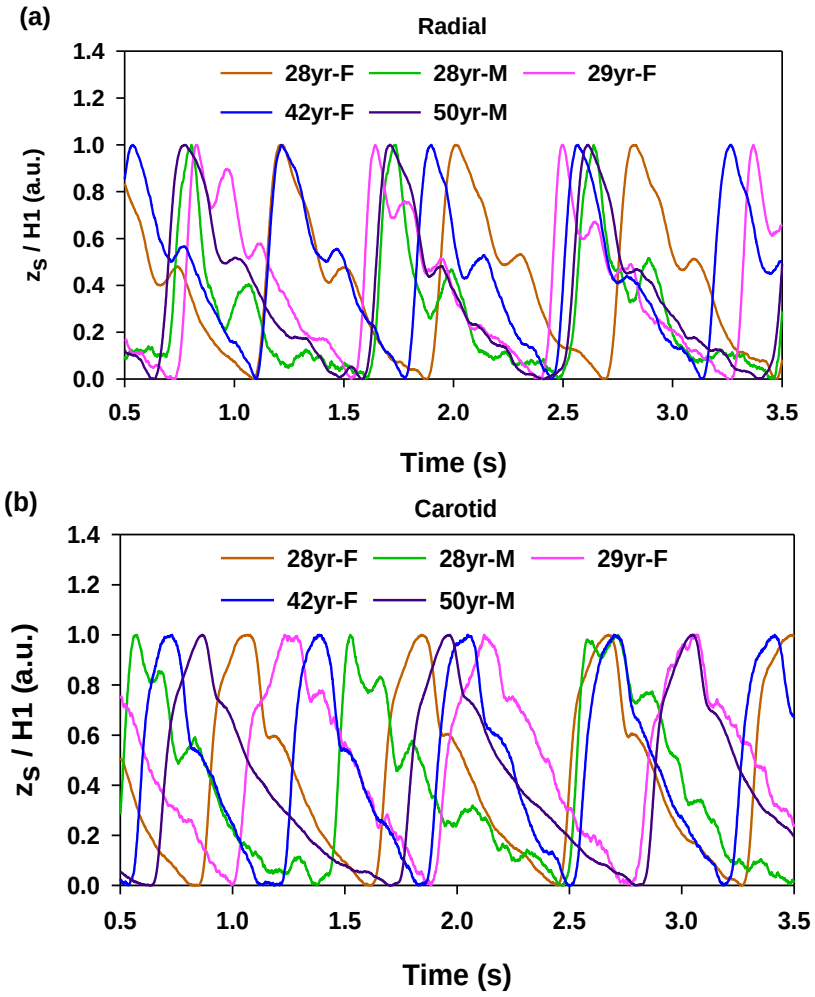


Figure 3.6 Normalized (a) radial and (b) carotid pulse waveforms of the five subjects.

### 3.3.2 Key Tonometric Parameters

To validate the accuracy in capturing the physiological significance of a pulse signal, the key tonometric parameters of these pulse waveforms are summarized in Table 3.1, for comparison with the related findings in the literature. As the blood pressure wave travels from the highly elastic central arteries to the stiffer brachial artery, the upper portion of the wave becomes narrower, the systolic peak becomes more prominent and systolic pressure increases [53, 54]. Therefore, H1/H5 goes up from the carotid pulse to the radial pulse. As shown in Table 3.1, H1/H5 of all the five subjects increases from carotid to radial. The upstroke time, t1, goes up from radial to carotid for the five subjects, which is also in agreement with the literature [53].

Table 3.1 Key tonometric parameters of the measured (a) radial and (b) carotid pulse waveforms of the five subjects.

(a)

| Parameters | 28yr-F | 29yr-F | 28yr-M | 42yr-F | 50yr-M |
|---|---|---|---|---|---|
| H1/H5 | 1.96 | 2.02 | 1.78 | 1.96 | 1.74 |
| t1 | 0.13 | 0.12 | 0.13 | 0.13 | 0.15 |
| t2 | 0.35 | 0.35 | 0.31 | 0.30 | 0.34 |
| t3 | 0.46 | 0.53 | 0.62 | 0.38 | 0.62 |
| T | 0.81 | 0.88 | 0.93 | 0.69 | 0.92 |

(b)

| Parameters | 28yr-F | 29yr-F | 28yr-M | 42yr-F | 50yr-M |
|---|---|---|---|---|---|
| H1/H5 | 1.66 | 1.32 | 1.59 | 1.57 | 1.38 |
| t1 | 0.22 | 0.25 | 0.14 | 0.21 | 0.24 |
| t2 | 0.32 | 0.34 | 0.34 | 0.31 | 0.31 |
| t3 | 0.48 | 0.56 | 0.70 | 0.37 | 0.71 |
| T | 0.80 | 0.90 | 1.04 | 0.68 | 1.02 |

The measured systolic ejection duration, t2, is slightly longer in the radial pulse than the carotid pulse [53]. Except the 28yr-M and 42yr-F subject, the rest of the four subjects exhibit this trend. The systolic ejection duration, t2, decreases with increasing heart rate. The 42yr-F has the fastest heart rate and thus registers the shortest t2 among the subjects. However, although the 50yr-M has a slow heart rate, his systolic ejection duration is relatively short, as compared with the other three subjects. Women have a shorter diastolic duration, t3, than men [55], which is also observed in Table 3.1.

### 3.3.3 Pulse Wave Velocity and Augmentation Index

Owing to its transit path spanning the artery of the upper limb [56], carotid-radial PWV serves as a non-invasive direct indicator of arterial stiffness, and can be easily obtained from the pulse signals measured at the body surface. The transit distance is measured on the body surface of a subject using a flexible ruler. The PWV of a subject is measured only once. The measured strongest pulse signals of the radial and carotid arteries are used for calculating the PWV. To

find the onset of a carotid pulse cycle or a radial pulse cycle, a pulse signal is multiplied by -1, and then findpeaks function is applied to the flipped pulse signal to find the location of the onset. The time difference between a carotid pulse cycle and its corresponding radial pulse cycle is the time delay [43]. The calculated time delay on a subject is the average value from all the pulse cycles of the two 10s pulse signals.

As illustrated in Figure 3.7 (b), this PWV is estimated by the transit distance, $L$, between the carotid artery and radial artery divided by the time delay, $\Delta t$, from the simultaneously measured pulse signals at the two arteries [57]:

$$PWV = L / \Delta t \tag{3.1}$$

The measured carotid-radial PWV of the three subjects: 29yr-F, 28yr-M, and 50yr-M, is summarized in Table 3.2 (a), together with the related data in the literature. The pulse signals measured on the other two subjects are not clear for unknown reasons, and thus their PWV is not available. The calculated carotid-radial PWV for the two subjects without hypertension is in line with the PWV values in the literature: a normal distribution of 9.01±1.2 m/s of 17 individuals with an age distribution of 32.8±9.5 years [58]. The measured carotid-femoral PWV on 204 apparently healthy subjects (88 men and 116women, age: 19-76 years) in the literature [59] shows that women have a lower PWV than men. As shown in Table 3.2 (a), the 29yr-F exhibits a lower carotid-radial PWV than the 29yr-M. Aortic wave velocity increases with age, and is more than doubled from age 20 to 100, because of the increase in pulse pressure and systolic pressure. It is accentuated by hypertension and by arterial degeneration [60]. Thus, it is reasonable that the 50yr-M exhibits the highest carotid-radial PWV, 15.36 m/s.

Augmentation is a manifestation of early wave reflection and the boost of pressure from the systolic shoulder to the systolic pressure peak [12, 61]. Increased radial AI and carotid AI

have been directly linked with several risk factors, such as diabetes, hypertension, and end-stage renal failure and have a significant effect on the future cardiovascular diseases. As illustrated in Figure 3.7 (c), the radial AI is calculated as the ratio of the first systolic peak to the second systolic peak (or inflection point) [13]:

$$radial\ AI(\%) = P2 / P1 \times 100\% \tag{3.2}$$

Conversely, the carotid pulse waveform can be divided into four types: A, B, C, and D, with the observed augmentation accordingly [62]. Among the four types, there are two wave types that clearly distinguish elastic (Type C) and stiffer (Type A) arteries, as can be seen in Figure 3.7 (d) and Figure 3.7 (e). In a Type A subject, the peak systolic pressure occurs in late systole after a well-defined inflection point. In contrast, in a Type C subject, the peak systolic pressure precedes a well-defined inflection point.

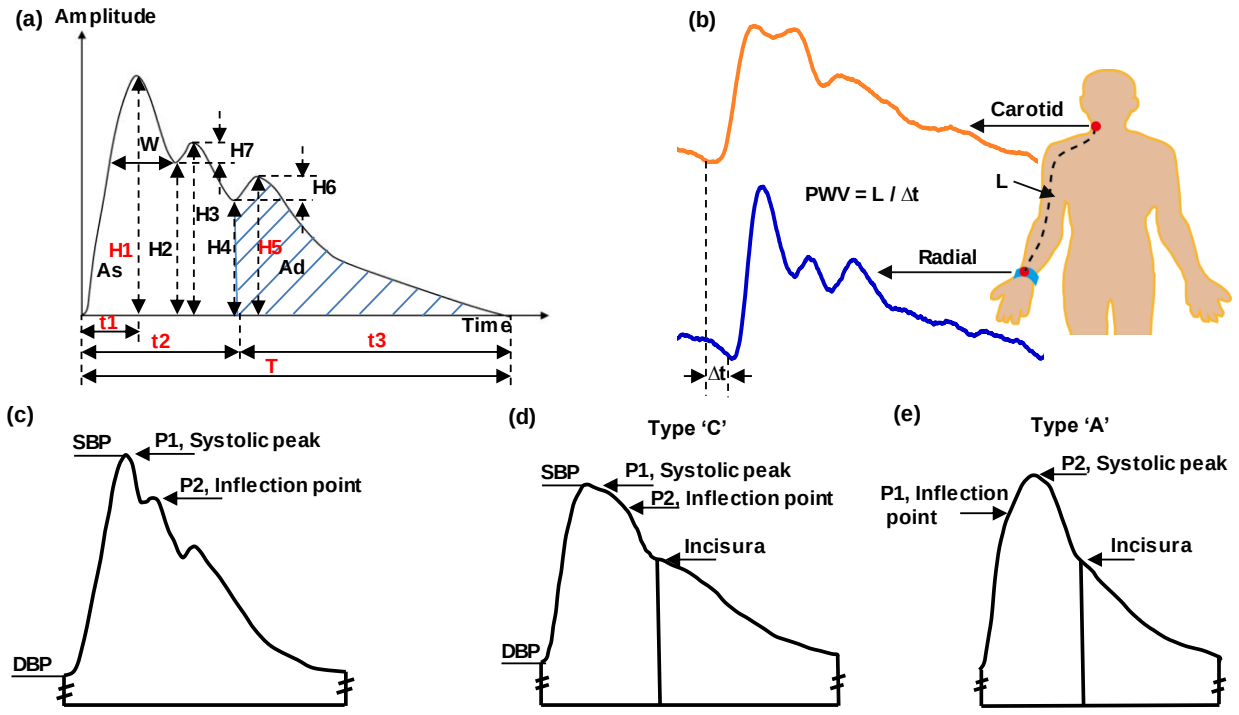


Figure 3.7 Key parameters of an arterial pulse waveform, (a) tonometric parameters, (b) PWV, (c) radial AI [63], (d) carotid AI for Type C and (e) carotid AI for Type A [55, 62].

The carotid AI is calculated at the ratio of the difference between the inflection point of the waveform and peak systolic pressure as a percentage of the pulse pressure [64]:

$$carotid\ AI(\%) = \frac{P2 - P1}{SBP - DBP} \times 100\% \tag{3.3}$$

To extract the carotid or radial AI from a pulse signal, the key is on determining the locations and values of inflection points, P2. Toward this, the fourth-order derivative [55, 63] is first applied to the pulse signal to obtain its fourth-order derivative, as illustrated in Figure 3.8. Then, the locations of zero points in the fourth-order derivative are extracted by diff function. The pink point indicates the corresponding reflection point of a pulse cycle. Representing inflection points, the locations of zero points are matched to the pulse signal to obtain the values of inflection points, P2. The value of systolic peak, P1, is easily found by applying findpeaks function to the pulse signal. As to carotid AI, SBP is the same as P1, DBP can be found by using findpeaks function to the flipped pulse signal.

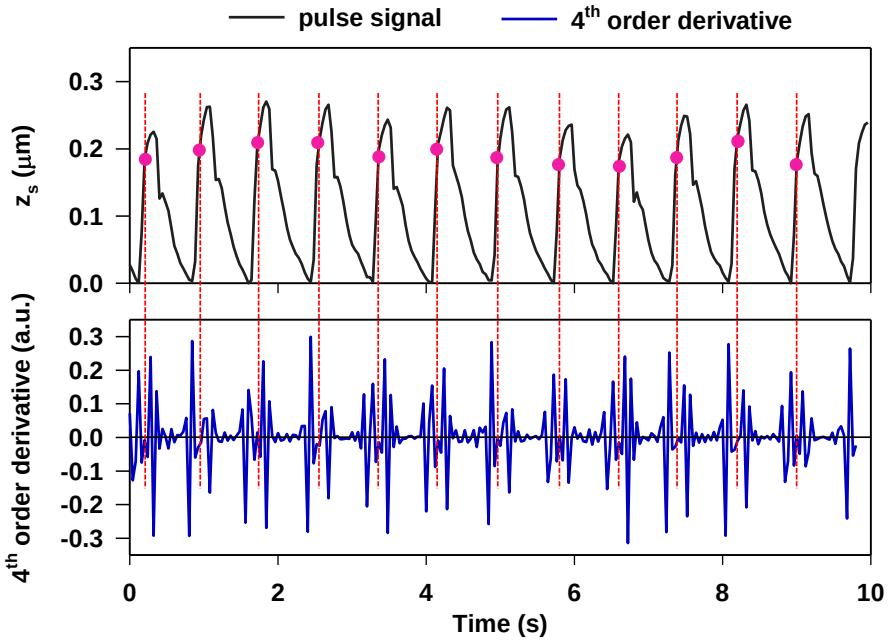


Figure 3.8 The fourth-order derivative of a carotid arterial pulse signal for determining the locations and values of inflection points, P2.

The carotid AI and radial AI of the five subjects are summarized in Table 3.2(b), together with the related data in the literature. At any age, the late systolic pressure wave is lower in the radial artery than in the carotid artery [60] and thus the radial AI is always positive. In contrast, carotid AI can be negative or positive. A positive carotid AI implies an early wave reflection, while a negative carotid AI indicates a late wave reflection (occurring in late systole) [64]. With aging or increasing cardiovascular risk, arteries stiffen and AI becomes increasingly positive [65]. The radial AI measured on 632 subjects with no CVD in the literature [66] shows that the radial AI is significantly higher in women than in men (81.1±16.1 versus 69.5±16.3), and the radial AI in men increases slightly faster with age from 20's to 70's than the radial AI in women.

Table 3.2 Comparison of the (a) PWV and (b) radial AI (rAI) and carotid AI (cAI) among the subjects.

(a)

| | This work Carotid-radial PWV | | | Aortic-femoral PWV [59] | | Carotid-radial PWV | |
|---|---|---|---|---|---|---|---|
| | | | | | | [67] | [54] |
| Subject | 29yr-F | 28yr-M | 50yr-M | Male | Female | | |
| PWV (m/s) | 6.72 | 10.19 | 15.36 | 10.5±2.2 | 9.5±1.9 | 8.76±1.65 | 9.01±1.2 |

(b)

| | This work | | | | | [59] | | [66] | |
|---|---|---|---|---|---|---|---|---|---|
| | 28yr-F | 29yr-F | 28yr-M | 42yr-F | 50yr-M | Male | Female | Male | Female |
| cAI (%) | 13.19 | 28.65 | -10.86 | 16.79 | 29.46 | 7.1±20.2 | 18.6±16.9 | -- | -- |
| rAI (%) | 81.21 | 75.44 | 63.03 | 85.93 | 89.27 | 73.8±18.5 | 84.5±17.1 | 69.5±16.3 | 81.1 ±16.1 |

According to another publication [59], the radial AI is higher than the carotid AI regardless of sex (7.1±20.2 versus 73.8±18.5 for men and 18.6±16.9 versus 84.5±17.1 for women); and both the radial AI and carotid AI are higher in women than men. These two trends are both manifested in our measurements. As the healthiest subject, the 28yr-M registers a

negative carotid AI and the lowest radial AI. The 50yr-M subject exhibits the highest carotid AI and radial AI, validating the principle: AI is positively correlated with age, blood pressure, and PWV.

3.3.4 Repeatability

To evaluate the repeatability of the sensor, three trials are carried out to measure the same pulse signal of a subject. In each trial, the sensor is realigned above an artery and similar finger-holding strength felt by the individual is used to press the sensor against the artery. Thus, the location of the transducer array relative to an artery and the location of the fingers relative to the transducer array vary among the three trials.

Table 3.3 Comparison of the parameters of the pulse signals of the 28yr-F and 28yr-M subjects measured under similar hold-down pressure.

(a)

| | 28yr-F | | | | | |
|---|---|---|---|---|---|---|
| | Hold-down pressure (Ω) | | | | H1/H5 | AI(%) |
| | Pressure | $R_0$ | Avg($R'_0$) | $R_0$-Avg($R'_0$) | | |
| RA | Trial 1 | 6004 | 5165 | 848 | 1.72 | 80.25 |
| | Trial 2 | 6938 | 5684 | 1254 | 1.99 | 77.61 |
| | Trial 3 | 6938 | 5676 | 1262 | 1.90 | 77.64 |
| CA | Trial 1 | 5788 | 4898 | 890 | 1.66 | 16.66 |
| | Trial 2 | 5788 | 4927 | 861 | 1.74 | 15.46 |
| | Trial 3 | 5788 | 4927 | 861 | 1.55 | 15.49 |

(b)

| | 28yr-M | | | | | |
|---|---|---|---|---|---|---|
| | Hold-down pressure (Ω) | | | | H1/H5 | AI(%) |
| | Pressure | $R_0$ | Avg($R'_0$) | $R_0$-Avg($R'_0$) | | |
| RA | Trial 1 | 6004 | 5471 | 533 | 1.80 | 62.43 |
| | Trial 2 | 6004 | 5355 | 649 | 2.15 | 46.34 |
| | Trial 3 | 6938 | 6177 | 761 | 2.09 | 48.77 |
| CA | Trial 1 | 5788 | 4764 | 1024 | 1.70 | -16.79 |
| | Trial 2 | 5788 | 4759 | 1029 | 1.58 | -11.33 |
| | Trial 3 | 5788 | 4745 | 1043 | 1.52 | -10.95 |

The measured H1/H5 and AI of the radial and carotid pulse signals of the 28yr-F and 28yr-M subjects from three trials are summarized in Table 3.3. Evidently, the hold-down pressure varies modestly among the trials, despite similar finger-holding strength. The fluctuation of the measured H1/H5 ratio and AI among the trials is comparable to that among the three hold-down pressures.

### 3.4 Conclusion

This chapter investigated the feasibility of arterial pulse measurement using microfluidic-based tactile sensors on five subjects. The sensor entails a PDMS microstructure embedded with a 5×1 transducer array and 1.5mm spatial resolution, which can be easily aligned by an untrained individual over the arterial region. The arterial pulse signals are captured by holding the sensor toward the arterial sites with certain hold-down pressure. Pulse signal exerted on the top of the microstructure registered as resistance change and captured by the transducers. The entire experimental setup and measurement protocol for capturing the arterial pulse signals are described. The readout from the sensor on pulse measurement is real-time viewed and recorded by the LabVIEW program. Data-processing algorithms for extracting arterial pulse waveforms and key parameters were demonstrated.

The comparison of tonometric parameters, PWV, and AI among the five subjects indicate that the older subjects have a higher PWV due to the stiffer artery during aging, the female has larger AI than male, and the older subject has larger AI than the young subjects. The results are consistent with the related findings in the literature. The repeatability of the sensor on pulse measurement was also described. The results show that the sensor is robust with good repeatability. Overall, the feasibility of the sensor on tracking the key features of the arterial pulse signals is validated.

# CHAPTER 4

# ANALYSIS OF ARTERIAL WALL MOTIONS AND MODEL-BASED METHOD OF ESTIMATING ARTERIAL WALL PARAMETERS

Analysis of radial and longitudinal motion of the arterial wall in the context of pulsatile pressure and flow can help to understand their physiological implications to the cardiovascular system. The motion of the arterial wall accompanies the pulsatile pressure and flow in the artery plays a critical role in blood circulation throughout the arterial tree [15, 68-70]. Therefore, the motion of the arterial wall has been investigated for its clinical implications of CVDs and vascular diseases [71-74].

This chapter re-examines the 1D governing equations of axial blood flow in the artery and the constitutive equation of the arterial wall and derives the governing equations for the radial and longitudinal motion of the arterial wall with consideration of their coupling. Owing to the time-harmonic nature of its radial motion, the arterial wall is modeled as a second-order dynamic system. By combining this dynamic model with a hemodynamic model of blood flow in the artery, the arterial wall parameters: elasticity, viscosity, and radius, were represented by spring constant and damping coefficient. The details about the derivation of those equations will be described in this chapter.

## 4.1 Radial and Longitudinal Motion of the Arterial Wall

As the main focus of extensive research, the radial motion of the arterial wall has formed the basis for estimation of the arterial wall stiffness, mostly in terms of PWV, with the longitudinal motion being neglected [3, 71]. Nowadays, PWV is a well-established independent risk predictor of adverse cardiovascular events. However, current established methods for measuring the arterial wall stiffness cannot discern small preclinical atherosclerotic or

arteriosclerotic changes in a comprehensive manner [72]. Yet, detecting these preclinical aberrant changes in the arterial tree could be beneficial in developing novel strategies to prevent the progress of vascular diseases [72]. Compared with its radial motion, the longitudinal motion of the arterial wall has been suggested to be an earlier and more sensitive measure of vascular diseases [75, 76]. Experimental studies have recently found that the measured arterial wall stiffness solely based on the radial motion is correlated to the longitudinal motion amplitude of the arterial wall [74, 77, 78]. For the purpose of devising new clinic indices for detecting preclinical aberrant changes and finding its influence on the radial motion of the arterial wall, the longitudinal motion of the arterial wall needs to be studied.

The longitudinal motion of the arterial wall was investigated for the purpose of complimenting the arterial wall stiffness based on the radial motion and developing new clinic indices for vascular diseases [72, 73, 79, 80]. Toward this end, several studies were conducted on finding the underlying mechanism of the longitudinal motion pattern of the arterial wall, but the conclusions from different studies are contradictory [78, 79, 81]. For instance, Ahlgren et al. [81] found that the wall shear stress (i.e., local blood flow) is not the main driving force of the longitudinal motion, while Au et al. [78] found that the local blood flow is closely related to the first anterograde motion of the longitudinal motion. These studies [78, 79, 81] investigated the longitudinal motion of the arterial wall purely from the physiological perspective (by altering one or two factors through drug administration and utilizing statistical analysis and/or machine-learning to establish their correlation to the longitudinal motion). Yet, the determinants of the bidirectional pattern of the longitudinal motion of the arterial wall remain unclear [76, 79], although new clinical indices have been created from the measured longitudinal motion of the arterial wall via machine-learning techniques [80].

Since the pulsatile pressure and flow in the artery are adjacent to the arterial wall and accompany the motion of the arterial wall, intuitively, a direct relation should exist between these two parameters in the artery and the radial and longitudinal motion of the arterial wall. Then, the question arises: how are pulsatile pressure and flow related to the radial and longitudinal motion of the arterial wall? From the mechanical perspective, the governing equations of the radial and longitudinal motion of the arterial wall will be discussed, and analyze how the radial ($u_r$) and longitudinal ($u_x$) motion of the arterial wall is related to the pulsatile pressure ($\Delta p$) and flow rate ($Q$) in the artery. Comparison of the analyzed results with some recent experimental findings in the literature [72, 78, 81] sheds insights on the physiological implications of the radial and longitudinal motion of the arterial wall to the cardiovascular system. As such, they may serve as the basis for developing model-based clinical indices from the measured radial and longitudinal motion of the arterial wall for inferring the cardiovascular system condition, instead of machine-learning-based clinical indices.

### 4.1.1 Role of the radial motion of the arterial wall in pulsatile pressure and flow in the artery

#### 4.1.1.1 Governing equations for axial blood flow in the artery and the radial motion of the arterial wall

The blood circulation in the arterial tree involves complex 3D fluid-structure interaction between the blood flow in the artery and the motion of the arterial wall [82, 83]. To better understand the physiological implications of the hemodynamic parameters and arterial wall motion parameters to cardiovascular diseases, 1D modeling of the blood flow in an artery has been well established and validated by experimental studies to some extent [68]. The fundamental assumptions underlying the 1D modeling are summarized below [68, 83]:

1) The artery has a straight, uniform, circular shape and entails axisymmetric blood flow;

2) The blood in the artery is incompressible homogeneous Newtonian fluid;

3) The density, $\rho_b$, and viscosity, $\mu_b$, of the blood are constant;

4) Small disturbances (i.e., arterial pulses) with the angular frequency, ω, and the wavelength, $\lambda$, take place in an artery with the radius being much smaller than the wavelength (i.e., $r_0 \ll \lambda$) and thus no blood flow along the radial direction occurs;

5) As to large arteries (e.g., common carotid artery and aorta), the Womersley number $\alpha = r_0 \cdot \sqrt{\rho_b \omega / \mu_b}$ is much larger than 1. Then, the boundary layer is thin and the blood flow velocity profile is close to plug flow. Therefore, the pressure and velocity are assumed to be uniform over the entire cross-section.

As shown in Figure 4.1, the 1D governing equations of axial pulsatile flow in a distensible artery are then derived from conservation of mass (equation of continuity) and conservation of momentum (Navier-Stoke equation) along the axial direction (x-axis) of the artery [68]:

$$\frac{\partial A}{\partial t} + \frac{\partial (AU)}{\partial x} = 0 \tag{4.1}$$

$$\underset{\text{(TA)}}{\frac{\partial U}{\partial t}} + \underset{\text{(CA)}}{U \cdot \frac{\partial U}{\partial x}} = \underset{\text{(PG)}}{-\frac{1}{\rho_b} \cdot \frac{\partial p}{\partial x}} + \underset{\text{(VF)}}{\frac{f}{\rho_b A}} \tag{4.2}$$

where $U(x, t)$ and $p(x, t)$ denote the blood flow velocity and blood pressure averaged over the entire cross-section, respectively; $A(x,t)$ is the cross-section area of the lumen; and $f$ denotes the friction force in the blood flow. The blood flow rate, $Q=AU$, is the product of the average blood flow velocity and the cross-section area. The terms in the Navier-Stoke equation are the temporal acceleration (TA), convective acceleration (CA), pressure gradient (PG) and the viscous force (VF). Given the small disturbances and the plug flow, the CA is negligible [68]. When the

Womersley number is much larger than 1, the VF is also small, relative to the TA and the PG [68, 83].

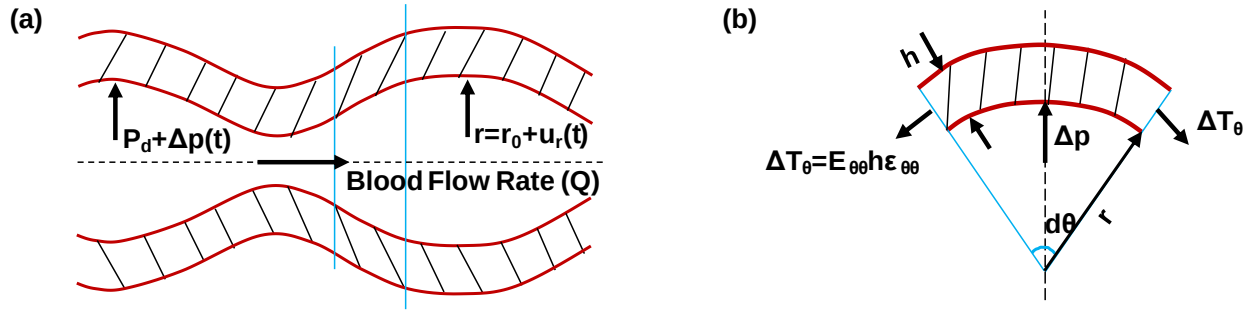


Figure 4.1 Schematics of (a) pulsatile pressure $\Delta p(t)$ and axial blood flow $Q$ in the artery and (b) circumferential tension force $\Delta T_\theta$ in the arterial wall due to its radial dilation $u_r$.

The above two equations contain three time-varying parameters: blood pressure ($p$), blood flow velocity ($U$), and cross-section area ($A$) of the artery, which varies with radial dilation of the arterial wall. To complement the above two equations, the constitutive equation of the arterial wall (or arterial wall compliance) [3] is included in Eq. (4.1):

$$C_A = \frac{\partial A(t)}{\partial p(t)} = \frac{2\pi r_0 \partial u_r(t)}{\partial p(t)} \tag{4.3}$$

where $u_r(t)$ is the radial displacement of the arterial wall and $r_0$ is the artery radius at diastolic pressure, $P_d$. Both $r_0$ and $C_A$ are related to the transmural pressure in the arterial wall: $P_T=P_{ext}-P_d$, with $P_{ext}$ being the pressure outside the arterial wall.

In Eq. (4.3), a purely elastic, linear relation between the pulsatile pressure and the radial displacement is assumed for the arterial wall. Furthermore, the radial displacement amplitude, $u_{r0}$, is assumed to be much smaller than the arterial radius $r_0$ (i.e., $u_{r0}/r_0 \ll 1$). By taking the first-order derivative of Eq. (4.3) with respect to $t$ and $x$, respectively, the following relations between the radial displacement and the pulsatile pressure is obtained:

$$\frac{\partial p}{\partial t} = \frac{1}{C_A} \cdot \frac{\partial A}{\partial t} = \frac{2\pi r_0}{C_A} \cdot \frac{\partial u_r}{\partial t} \tag{4.4}$$

$$\frac{\partial p}{\partial x} = \frac{1}{C_A} \cdot \frac{\partial A}{\partial x} = \frac{2\pi r_0}{C_A} \cdot \frac{\partial u_r}{\partial x} \tag{4.5}$$

4.1.1.2 Pulsatile pressure wave in the artery

Substituting Eq. (4.4) into Eq. (4.1), yields the following relation:

$$C_A \cdot \frac{\partial p}{\partial t} + \frac{\partial (AU)}{\partial x} = 0 \tag{4.6}$$

Now, we take the derivative of Eq. (4.6) with respect to *t* and take the derivative of Eq. (4.2) with respect to *x*, add the two equations up, and neglect the two small terms (CA and VF):

$$\frac{\partial^2 p}{\partial t^2} = \frac{A}{\rho_b C_A} \cdot \frac{\partial^2 p}{\partial x^2} \tag{4.7}$$

Eq. (4.7) indicates that there is a pulsatile pressure wave in the artery propagating along the arterial tree with the propagation velocity, commonly referred to as the PWV:

$$PWV^2 = \frac{A}{\rho_b C_A} \tag{4.8}$$

By treating the arterial wall as a stretched thin-walled membrane in a circular shape with constant thickness, *h*, and constant density, $\rho_w$, the radial displacement, $u_r$, gives rise to a circumferential tension force, $\Delta T_\theta$, as shown in Figure 4.1(b). This tension force can be expressed using an effective incremental circumferential modulus, $E_{\theta\theta}$, of the arterial wall:

$$\Delta T_\theta = E_{\theta\theta} \cdot h \cdot \frac{u_r}{r_0} = r_0 \cdot \Delta p \tag{4.9}$$

Note that this circumferential tension force needs to counterbalance the radial force arising from the pulsatile pressure, $\Delta p$. Then, the arterial wall compliance is related to the physical properties and geometries of the arterial wall by:

$$C_A = \frac{\partial A}{\partial p} = \frac{2r_0 A_0}{E_{\theta\theta} h} \tag{4.10}$$

Substituting Eq. (4.10) into Eq. (4.8) leads to the well-known Moens-Korteweg formula [71] as Eq. (1.1).

4.1.1.3 Radial displacement wave in the arterial wall

Now, we derive the governing equation for the radial motion of the arterial wall by replacing the pulsatile pressure with the radial displacement in Eqs. (4.1) and (4.2). Substituting Eq. (4.5) into Eqs. (4.1) and (4.2) gives rise to the following two equations:

$$2\pi r_0 \cdot \frac{\partial u_r}{\partial t} + \frac{\partial (AU)}{\partial x} = 0 \tag{4.11}$$

$$\frac{\partial U}{\partial t} + U \cdot \frac{\partial U}{\partial x} = -\frac{1}{\rho} \cdot \frac{2\pi r_0}{C_A} \frac{\partial u_r}{\partial x} + \frac{f}{\rho A} \tag{4.12}$$

By neglecting the two small terms (CA and VF) in Eq. (4.12) and combining the above two equations, the governing equation for the radial motion of the arterial wall is obtained:

$$\frac{\partial^2 u_r}{\partial t^2} = \frac{A}{\rho_b C_A} \cdot \frac{\partial^2 u_r}{\partial x^2} \tag{4.13}$$

Eq. (4.13) indicates that there is a radial displacement wave in the arterial wall (similar to a transverse wave in a string) propagating along the arterial tree. Comparison of Eqs. (4.7) and (4.13) shows that the radial displacement wave in the arterial wall and the pulsatile pressure wave in the artery propagate simultaneously (Windkessel effect) along the arterial tree with the same propagation velocity. Mathematically, the coincidence of the two waves arises from the definition of the arterial wall compliance in Eq. (4.10) and explains why the propagation velocity combines the physical properties and geometries of the blood and the arterial wall. The experimentally observed similarity between arterial radius waveform and pulsatile pressure waveform [84] is consistent with in the arterial wall compliance.

4.1.1.4 Driving force for the pulsatile flow in the artery

Based on Eqs. (4.2) and (4.12), the driving forces for the pulsatile flow velocity ($U$) or pulsatile flow rate ($Q$) in the artery include the pressure gradient $\partial p/\partial x$ and the radial displacement gradient, $\partial u_r/\partial x$. According to Eqs. (4.5) and (4.10), the pressure gradient is related to the radial displacement gradient by:

$$\frac{\partial p}{\partial x} = \frac{E_{\theta\theta} h}{r_0^2} \cdot \frac{\partial u_r}{\partial x} \tag{4.14}$$

The pressure gradient is commonly related to the pulsatile flow rate, $Q$, by the vascular resistance, $R$ [85]:

$$Q = \frac{1}{R} \cdot \frac{\partial p}{\partial x} = \frac{E_{\theta\theta} h}{r_0^2 \cdot R} \cdot \frac{\partial u_r}{\partial x} \text{ with } R = \frac{8 L \mu_b}{\pi r_0^4} \tag{4.15}$$

where $L$ is the arterial length.

4.1.2 Radial Motion of Arterial Wall

The arterial wall is treated as a stretched thin-walled membrane in a circular shape with a constant thickness, $h$, and the constant density, $\rho_w$. The wall thickness is much smaller than the wall radius, $h / r_0 \ll 1$. A small segment of angle $d\theta$ and length $dx$ of the arterial wall is shown in Figure 4.2, which is at the transmural pressure, $P_T$, and is axially pre-stretched along its longitudinal direction. The circumferential and longitudinal tension forces in the arterial wall at diastolic pressure are $T_{0\theta}$ and $T_{0x}$, respectively. As such, the arterial wall is analogous to a stretched spring moving along both directions, whereas the arterial wall is treated as a stretched thin-walled membrane with a purely elastic, linear relation of the pulsatile pressure to the radial displacement, and undergoes only radial motion. The wall segment undergoes radial motion, $u_r(t)$ and longitudinal motion, $u_x(t)$ in a pulse cycle.

The arterial wall segment in Figure 4.2 is subject to the following forces along the radial direction:

1) A radial force results from the pulsatile pressure:

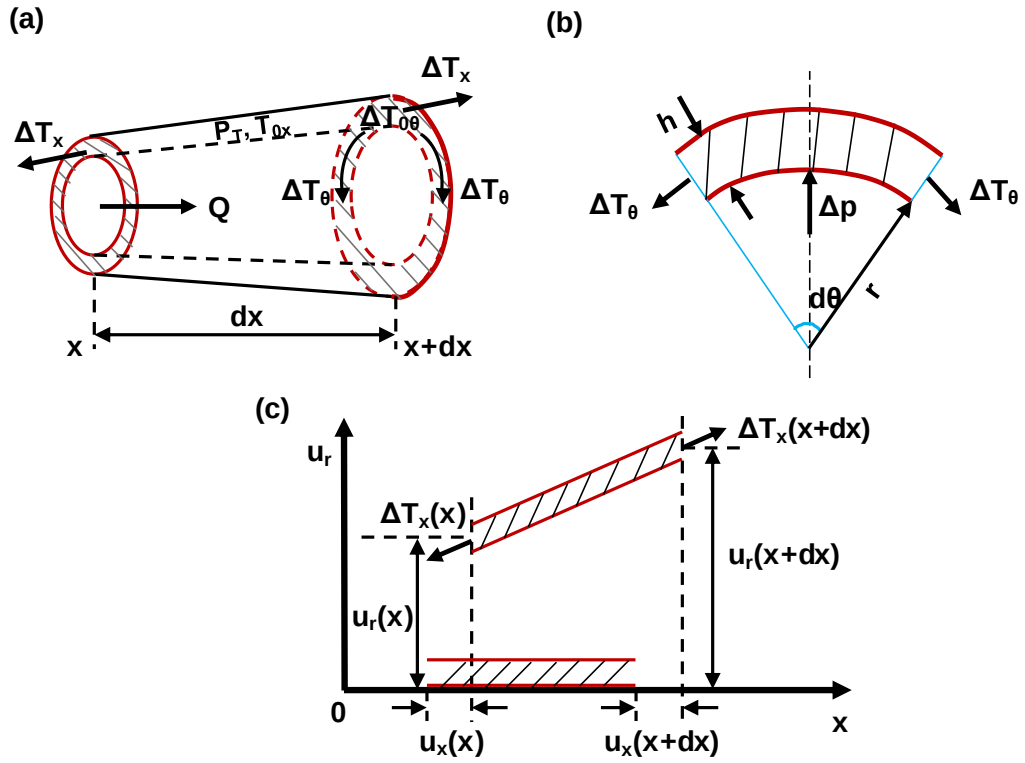


Figure 4.2 Coupled radial motion ($u_r$) and longitudinal motion ($u_x$) of a small segment of angle $d\theta$ and length $dx$ of the arterial wall (a) a segment of an artery of length $dx$. $Q$: the blood flow rate in the artery, $P_T$: the transmural pressure in the arterial wall, $T_{0x}$: the longitudinal tension force in the arterial wall at diastolic pressure, $T_{0\theta}$: the circumferential tension force in the arterial wall at diastolic pressure, $\Delta T_\theta$: the circumferential force due to the radial displacement (b) radial direction. $h$: arterial wall thickness, $\Delta p$: pulsatile pressure, $r=r_0+u_r$: the arterial wall radius. (c) longitudinal direction. $u_x(x)$ and $u_x(x+dx)$: longitudinal displacements at the positions of $x$ and $x+dx$, respectively, $u_r(x)$ and $u_r(x+dx)$: radial displacements at the positions of $x$ and $x+dx$, respectively.

$$F_{p-r} = \Delta p \cdot r_0 \cdot d\theta \cdot dx \tag{4.16}$$

2) The arterial wall experiences a circumferential strain: $\varepsilon_{\theta\theta}=u_r/r_0$. Then, the restoring force from the arterial wall along the radial direction becomes:

$$F_{\theta-r} = -(E_{\theta\theta} h \varepsilon_{\theta\theta} d\theta \cdot dx + \eta_{\theta\theta} h \frac{d\varepsilon_{\theta\theta}}{dt} d\theta \cdot dx) \tag{4.17}$$

where the second term is the viscous term with $\eta_{\theta\theta}$ being the effective damping modulus of the arterial wall.

3) Because of its radial motion, the arterial wall deforms along its longitudinal direction. The radial component from the longitudinal tension force of the wall segment is [86, 87]:

$$\Delta T_{x-r} = E_{xx} \cdot h \cdot r_0 \cdot d\theta \cdot \frac{\partial}{\partial x} \left\{ \left[ \frac{\partial u_x}{\partial x} + \frac{1}{2} \cdot \left( \frac{\partial u_r}{\partial x} \right)^2 \right] \frac{\partial u_r}{\partial x} \right\} \cdot dx \tag{4.18}$$

where $E_{xx}$ is an effective incremental longitudinal modulus of the arterial wall. Since the second term is small relative to the first term in the square brackets, the overall radial component from the longitudinal tension force becomes:

$$F_{x-r} = E_{xx} \cdot h \cdot r_0 \cdot d\theta \cdot \frac{\partial}{\partial x} \left( \frac{\partial u_x}{\partial x} \cdot \frac{\partial u_r}{\partial x} \right) \cdot dx \tag{4.19}$$

According to Newton's second law, the governing equation of the radial motion of the arterial wall segment is:

$$\rho_w h r_0 d\theta dx \cdot \frac{d^2 u_r}{dt^2} = F_{\theta-r} + F_{x-r} + F_{p-r} \tag{4.20}$$

Substituting the expressions for the radial forces into Eq. (4.20) gives rise to:

$$\frac{d^2 u_r}{dt^2} + \frac{E_{\theta\theta}}{\rho_w r_0^2} \cdot u_r + \frac{\eta_{\theta\theta}}{\rho_w r_0^2} \cdot \frac{du_r}{dt} = \frac{E_{xx}}{\rho_w} \cdot \frac{\partial}{\partial x} \left\{ \frac{\partial u_x}{\partial x} \cdot \frac{\partial u_r}{\partial x} \right\} + \frac{\Delta p}{\rho_w h} \tag{4.21}$$

When the time-variant terms in Eq. (4.21) are zero and the longitudinal motion term is neglected, the above equation reduces to Eq.(1.1) and consequently the arterial wall compliance:

$$\frac{E_{\theta\theta}}{\rho_w r_0^2}\cdot u_r = \frac{\Delta p}{\rho_w h} \rightarrow C_A = \frac{\Delta A}{\Delta p} = \frac{2r_0 A_0}{E_{\theta\theta} h} \tag{4.22}$$

As such, the measured arterial wall stiffness (PWV) in Eq. (1.1) ignores the viscous nature of the radial motion of the arterial wall and the influence of the longitudinal motion on the radial motion. After removing the inertial term and the longitudinal motion term, Eq. (4.22) becomes the commonly used Kelvin-Voigt material model for the arterial wall [70]:

$$\frac{E_{\theta\theta}}{\rho_w r_0^2}\cdot u_r + \frac{\eta_{\theta\theta}}{\rho_w r_0^2}\cdot\frac{du_r}{dt} = \frac{\Delta p}{\rho_w h} \tag{4.23}$$

Based on this equation, the elasticity and viscosity of the arterial wall are currently extracted from simultaneously measured pulsatile pressure waveform and artery radius waveform at the same arterial location. Comparison of Eq. (4.23) with Eq. (4.21) indicates that while the driving force for the quasi-static radial motion is the pulsatile pressure, the dynamic radial motion (acceleration) of the arterial wall arises from the radial force component of the longitudinal motion of the arterial wall.

By replacing the pulsatile pressure with the radial displacement, Eq. (4.21) becomes:

$$\frac{d^2 u_r}{dt^2} + \left(\frac{E_{\theta\theta}}{\rho_w r_0^2} - \frac{2\pi r_0}{C_A \rho_w h}\right)\cdot u_r + \frac{\eta_{\theta\theta}}{\rho_w r_0^2}\cdot\frac{du_r}{dt} = \frac{E_{xx}}{\rho_w}\cdot\frac{\partial}{\partial x}\left\{\frac{\partial u_x}{\partial x}\cdot\frac{\partial u_r}{\partial x}\right\} \tag{4.24}$$

Accordingly, the arterial wall at any axial position behaves as a second-order dynamic system and undergoes radial vibrations, with the driving force from the longitudinal motion.

By replacing the radial displacement in Eq. (4.21) with the pulsatile pressure, the governing equation for the pulsatile pressure acting on the arterial wall is obtained:

$$\frac{d^2\Delta p}{dt^2}+\left(\frac{E_{\theta\theta}}{\rho_w r_0^2}-\frac{2\pi r_0}{C_A\rho_w h}\right)\cdot\Delta p+\frac{\eta_{\theta\theta}}{\rho_w r_0^2}\cdot\frac{d\Delta p}{dt}=\frac{E_{xx}r_0^2}{E_{\theta\theta}\rho_w h}\cdot\frac{\partial}{\partial x}\left\{\frac{\partial u_x}{\partial x}\cdot\frac{\partial u_r}{\partial x}\right\} \tag{4.25}$$

The pulsatile pressure variation on the arterial wall is caused by the radial force component of the longitudinal motion of the arterial wall. Comparison of Eq. (4.25) with Eq. (4.24) suggests that the pulsatile pressure acting on the arterial wall and the radial motion of the arterial wall accompanies each other and exhibits the same dynamic nature. Taken together, locally at any axial position, the radial motion of the arterial wall and pulsatile pressure variation in the artery accompany each other and are both caused by the longitudinal motion of the arterial wall; systemically along the arterial tree, the radial displacement wave and pulsatile pressure wave propagation are driven by the pressure gradient and the radial displacement gradient.

4.1.3 Longitudinal Motion of Arterial Wall

The arterial wall segment in Figure 4.2 is subject to the following forces along the longitudinal direction:

1) The longitudinal motion of the arterial wall gives rise to the overall tension force:

$$F_{x-x}=E_{xx}\cdot h\cdot r_0\cdot d\theta\cdot\frac{\partial^2 u_x}{\partial x^2}\cdot dx \tag{4.26}$$

2) Owing to the radial motion of the arterial wall, the pulsatile pressure results in a longitudinal force:

$$F_{p-x}=-\Delta p\cdot\frac{\partial u_r}{\partial x}\cdot r_0\cdot d\theta\cdot dx=-\frac{2\pi r_0}{C_A}\cdot u_r\cdot\frac{\partial u_r}{\partial x}\cdot r_0\cdot d\theta\cdot dx \tag{4.27}$$

Note that the pulsatile pressure is further expressed in terms of the radial displacement.

3) The blood flow rate causes the wall shear stress, $\tau_w$, on the arterial wall. The overall shear force caused by the blood flow rate becomes [84]:

$$F_{Q-x} = \tau_w r_0 d\theta dx = \frac{4\eta_b Q}{\pi r_0^3} r_0 d\theta dx \tag{4.28}$$

By summarizing the above equations, the governing equation for the longitudinal motion of the arterial wall becomes:

$$\frac{d^2 u_x}{dt^2} = \frac{E_{xx}}{\rho_w} \cdot \frac{\partial^2 u_x}{\partial x^2} - \frac{\pi E_{\theta\theta}}{A_0 \cdot \rho_w} u_r \cdot \frac{\partial u_r}{\partial x} + \frac{4\eta_b Q}{\rho_w \cdot \pi r_0^3 \cdot h} \tag{4.29}$$

$$\frac{d^2 u_x}{dt^2} = \frac{E_{xx}}{\rho_w} \cdot \frac{\partial^2 u_x}{\partial x^2} - \frac{\Delta p}{h\rho_w} \cdot \frac{\partial u_r}{\partial x} + \frac{4\eta_b Q}{\rho_w \cdot \pi r_0^3 \cdot h} \tag{4.30}$$

Eq. (4.29) and Eq. (4.30) indicate that there is a longitudinal elastic wave in the arterial wall propagating along the arterial tree, with the propagation velocity solely related to the physical properties of the arterial wall. There are two driving forces for the longitudinal motion: one associated with the radial motion (or pulsatile pressure) and the other associated with the blood flow rate. The force associated with the blood flow rate is in the opposite direction to the force associated with the radial motion. Thus, a high blood flow rate may cause a large longitudinal motion, but the force associated with the radial motion counteracts the force associated with the blood flow rate to reduce the longitudinal motion amplitude.

### 4.1.4 Correlation of the Longitudinal Motion of the Arterial Wall to the Radial Motion of the Arterial Wall

Taivainen et al. [74] recently found that the longitudinal motion amplitude of the common carotid wall was directly correlated with its distensibility and inversely correlated with its PWV. Based on Eq. (4.24), the driving force for the radial motion is the longitudinal motion. Then, high longitudinal motion amplitude translates to high distensibility. As explained below, high distensibility indicates low circumferential modulus and thus is accompanied by low PWV, according to Eq. (1.1).

Elastic arteries are significantly pre-stretched along their axial (longitudinal) direction, setting up their tension state ($T_{0r}$ and $T_{0\theta}$) at diastolic pressure. With this axial pre-stretch, the radial motion of the arterial wall and the pulsatile pressure variation happen at any axial position, and enable the propagation of the radial displacement wave and the pulsatile pressure wave along the arterial tree. It was found [88] that high axial pre-stretch (or high longitudinal modulus $E_{xx}$) translates to a large radial motion and thus a high distensibility, which is possibly due to the axial pre-stretch may align collagen fibers to the axial direction and then lead to a low circumferential modulus ($E_{\theta\theta}$). According to Eq. (4.24), the combination of high longitudinal modulus and low circumferential modulus translates to high distensibility. Conversely, low axial pre-stretch corresponds to low longitudinal modulus and high circumferential modulus. Furthermore, given the same mean blood pressure, highly axially pre-stretched arterial wall can exhibit higher distensibility than less axially pre-stretched arterial wall [88]. Since a change in axial pre-stretch is typically accompanied by changes in artery radius and mean blood pressure, all these factors adjust the circumferential and longitudinal modulus of the arterial wall, and consequently its radial and longitudinal motion.

As the arterial wall stiffness increases from the aorta to the periphery [89], axial pre-stretch and artery radius decrease with more distal arterial locations [90]. Low axial pre-stretch in a peripheral artery translates to a low longitudinal modulus and a high circumferential modulus. Based on Eq. (4.24), the driving force for the radial motion is reduced, but the stiffness in the radial motion, which is proportional to the ratio of the circumferential modulus to the squared artery radius, is increased. Consequently, Eq. (4.24) explains the reason that the arterial wall distensibility decreases from the aorta to the periphery [89, 90]. Based on Eq. (4.25), the

pulsatile pressure amplitude increases from the aorta to the periphery, because of the accompanying increased ratio of longitudinal modulus to the circumferential modulus.

Thus, the radial motion of the arterial wall and the pulsatile pressure variation in the artery arises from the radial force component of the longitudinal motion of the arterial wall, establishing the correlation of the measured arterial wall distensibility with the longitudinal motion amplitude and explaining the decreasing trend of the arterial wall stiffness and the increasing trend of pulsatile pressure amplitude from the aorta to the periphery.

### 4.2 Rational of Model-Based Analysis for Estimating Arterial Wall Parameters

Typically, the available models may be divided into two classes: lumped parameter models (Windkessel) and distributed-parameter models (1D blood flow) for systemic analysis the cardiovascular system and extracting key parameters [91]. As mentioned in Section 1.2.2, the models for estimating arterial wall parameters from pulse signals measured using current instruments are complex, time-consuming, and not suitable for home use.

Toward this end, we propose a solution to at-home monitoring of arterial stiffness and damping. An arterial pulse waveform acquired by the sensor is used to represent the radial displacement of the arterial wall. The governing equation for the radial wall motion is first derived, revealing that the radial wall motion can be treated as time-harmonic vibration. Then, the arterial wall is modeled as a second-order dynamic system. Consequently, the spring stiffness and damping coefficient of the arterial wall are representative of the elasticity and viscosity of the arterial wall. Meanwhile, the effective longitudinal stiffness is defined to evaluate the driving force for the radial wall motion. By extracting the key features of the radial displacement, its $1^{st}$-order, and $2^{nd}$-order derivatives, and interpreting them in the context of vibrations, the above-

mentioned three physical properties of the arterial wall are obtained. In this study, two models are developed to estimate arterial wall parameters.

The rationale of model-based analysis of a measured pulse signal for tracking arterial wall parameters is depicted in Figure 4.3, where two different models are utilized to interpret the physiological meanings of these key features for estimating arterial wall parameters.

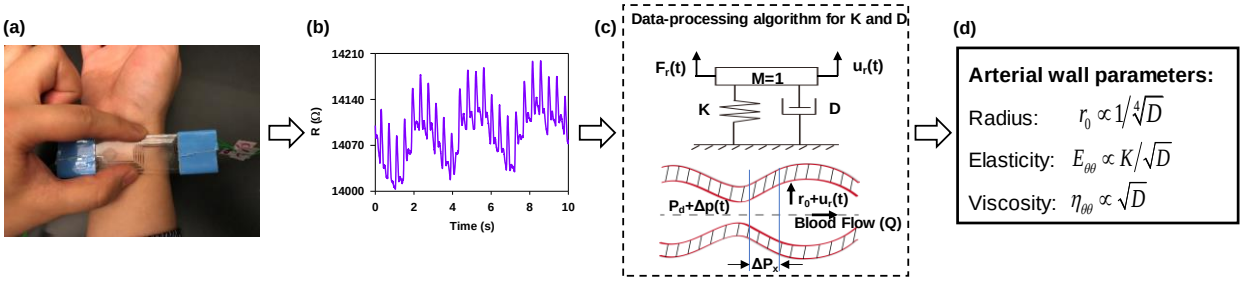


Figure 4.3 Flowchart of tracking changes of arterial wall parameters: (a) arterial pulse signal measurement by a microfluidic-based tactile sensor (b) a measured pulse signal (c) model-based analysis: dynamic system model of the arterial wall ($M$=1, $K$: spring stiffness, $D$: damping coefficient) and hemodynamic model of the blood flow ($Q$: blood flow rate, $\Delta P_x$: pressure gradient) (d) estimation of arterial wall parameter.

### 4.3 Dynamic Model of Radial Wall Motion

The governing equation of the radial wall motion is first derived, indicating that longitudinal stretching of the arterial wall is the driving force for the radial wall motion. Based on the derived equation and time-harmonic nature of its radial motion, the arterial wall is modeled as a second-order dynamic system. A microfluidic-based tactile sensor is used to acquire the arterial pulse waveform, which is used to represent the radial displacement of the arterial wall. Consequently, the 1$^{st}$-order and 2$^{nd}$-order derivatives of the radial displacement are the wall velocity and wall acceleration. In the context of time-harmonic vibration, the key features in the radial displacement and its two derivatives are interpreted to obtain the three

physical properties of the arterial wall: spring stiffness, damping coefficient, and the effective longitudinal stiffness associated with the driving force.

An arterial radius waveform cycle (radius displacement, $u_r$) and its 1st-order (velocity, $v$) and 2nd-order (acceleration, $a$) derivatives, together with their key features are illustrated in Figure 4.4.

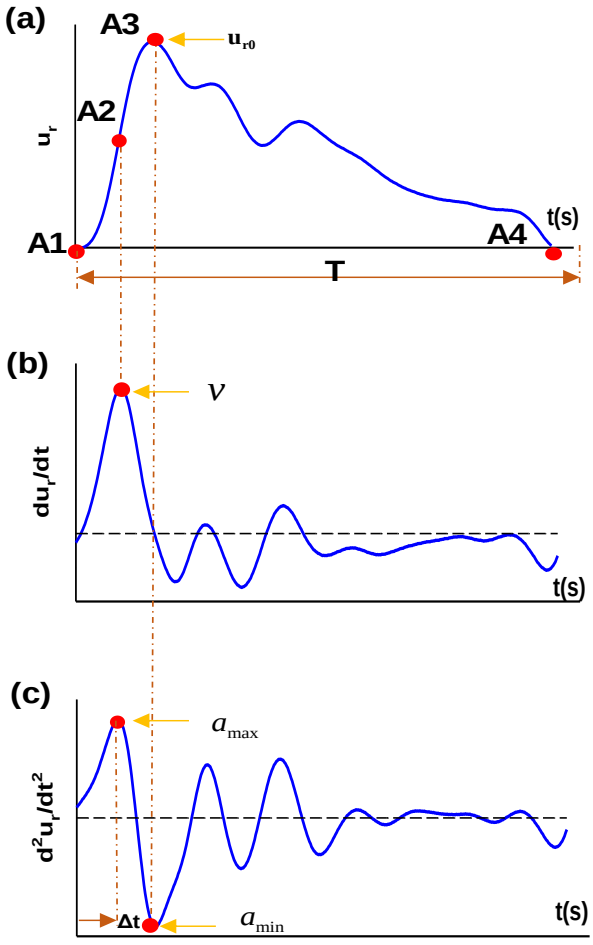


Figure 4.4 (a) One arterial radius waveform cycle ($u_r$); (b) its 1st-order derivative (velocity); (c) its 2nd-order derivative (acceleration), with their key features being labeled.

Owing to time-harmonic nature of its radial motion, the arterial wall is modeled as a second-order dynamic system with a unit mass ($M$=1) and a driving force ($F_r$) [92]:

$$M \cdot \frac{d^2 u_r}{dt^2} + D \cdot \frac{du_r}{dt} + K \cdot u_r = F_r \tag{4.31}$$

The damping coefficient ($D$) and the spring stiffness ($K$) of the dynamic system are related to the physical parameters of the arterial wall by the following relations [92]:

$$D = \frac{\eta_{\theta\theta}}{\rho_w r_0^2}, \; K = \frac{E_{\theta\theta}}{\rho_w r_0^2} \tag{4.32}$$

where $\rho_w$ is the arterial wall density; $r_0$ is the arterial wall radius at diastolic pressure ($P_d$); and the $E_{\theta\theta}$ and $\eta_{\theta\theta}$ are the effective incremental elasticity and viscosity of the arterial wall, respectively.

An arterial radius waveform cycle (radius displacement, $u_r$) and its 1st-order (velocity, $v$) and 2nd-order (acceleration, $a$) derivatives, together with their key features are illustrated in Figure 4.4 (a)-(c). As shown in Figure 4.4, in one radial vibration (or pulse) cycle, the radius waveform is separated by four points, A1, A2, A3, and A4, and is divided into three regions. Point A1 is the start of a vibration cycle. At Point A2, the arterial wall reaches its maximum velocity ($v_{max}$). At Point A3, the arterial wall achieves its vibration amplitude ($u_{r0}$). Point A4 is at the end of a cycle. In the A1-A2 region, the dominant force is the driving force (resulting from the axial blood flow in an artery) and the acceleration reaches its maximum ($a_{max}$) in this region. In the A2-A3 region, the driving force diminishes and the spring force in the arterial wall reaches its maximum, yielding the minimum acceleration ($a_{min}$). The A1-A2-A3 region arises mostly from the percussion wave and is used for estimating arterial wall parameters. Beyond Point A3, the radius waveform contains the complex reflective wave and is not used.

Because of the following two reasons: 1) the acceleration of the arterial wall shows a great similarity with the force pattern of the axial blood flow [71] and 2) the axial blood flow plays a critical role in driving the radial motion of the arterial wall, the difference between the

maximum and the minimum of the acceleration is used to approximate the driving force amplitude ($F_{r0}$):

$$F_{r0} = a_{\max} - a_{\min} \tag{4.33}$$

According to Eq. (4.31), the driving force amplitude is expected to be linearly proportional to the maximum damping force and the maximum spring force:

$$F_{r0} \propto K \cdot u_{r0}, \; F_{r0} \propto D \cdot v_{\max} \tag{4.34}$$

It was observed that a change in heart rate is accompanied by change of arterial wall parameters. It was found that factoring in the heart rate as shown in the above-mentioned equation can explain the experimental data reasonably. Then, Eq. (4.34) is modified to factor in the heart rate change:

$$F_{r0} \cdot \frac{\Delta t}{T} \propto K \cdot u_{r0}, \; F_{r0} \cdot \frac{\Delta t}{T} \propto D \cdot v_{\max} \tag{4.35}$$

where $\Delta t$ is the time duration between $a_{max}$ and $a_{min}$, and $T$ is the pulse duration. Consequently, the damping coefficient and the spring stiffness are estimated as:

$$K \propto \frac{a_{\max} - a_{\min}}{u_{r0}} \cdot \frac{\Delta t}{T} \tag{4.36}$$

$$D \propto \frac{a_{\max} - a_{\min}}{v_{\max}} \cdot \frac{\Delta t}{T} \tag{4.37}$$

In Eq. (4.36) and Eq. (4.37), the spring stiffness and damping coefficient are estimated by the ratio of the radius displacement and its two derivatives, thus no calibration is needed for obtaining the absolute values of the pulse amplitude. According to Eq. (4.31), the elasticity and viscosity of the arterial wall can be estimated as:

$$E_{\theta\theta} \propto K \cdot r_0^2 \tag{4.38}$$

$$\eta_{\theta\theta} \propto D \cdot r_0^2 \tag{4.39}$$

Note that the dynamic system parameters and the physical properties of the arterial wall estimated by the above expressions are all relatives, not absolute values. Therefore, they have no units.

**4.4 Hemodynamic Model of the Blood Flow**

The 1st-order and 2nd-order derivatives of the arterial radius waveform are representative of the blood flow rate ($Q$) and the rate of the pressure gradient change ($\partial(\Delta P_x)/\partial t$), respectively [34]:

$$v \propto Q \ , a \propto \frac{\partial}{\partial t}(\Delta P_x) \tag{4.40}$$

Then, we use the maximum velocity and the maximum change in the acceleration to represent the blood flow rate and the rate of the pressure gradient change, respectively:

$$Q \propto v_{\max} \tag{4.41}$$

$$\frac{\partial}{\partial t}(\Delta P_x) \propto \frac{\Delta(\Delta P_x)}{\Delta t / T} \propto a_{\max} - a_{\min} \tag{4.42}$$

Similar to Eq. (4.35), the pulse duration (T) is included in to factor in the heart rate change accompanying a change of arterial wall parameters. The pressure gradient ($\Delta P_x$) becomes:

$$\Delta P_x \propto \left(a_{\max} - a_{\min}\right) \cdot \Delta t / T \tag{4.43}$$

PVR is defined as the ratio of the pressure gradient to the blood flow rate in an artery [46]:

$$PVR = \Delta P_x / Q \tag{4.44}$$

By substituting Eq. (4.40) and Eq. (4.43) into Eq. (4.44), PVR is estimated as:

$$PVR = \frac{\Delta P_x}{Q} \propto \frac{a_{\max} - a_{\min}}{v_{\max}} \cdot \frac{\Delta t}{T} \tag{4.45}$$

Meanwhile, PVR is related to the arterial length ($L$), arterial radius ($r_0$) at the diastolic pressure ($P_d$), and blood viscosity ($\eta_b$) by [46]:

$$PVR = 8L\eta_b / \pi r_0^4 \tag{4.46}$$

Thus, the arterial wall radius can be inferred from the estimated PVR:

$$r_0 \propto 1/\sqrt[4]{PVR} \tag{4.47}$$

The governing equation for the arterial pulsatile pressure propagation is given by:

$$\partial^2 p / \partial t^2 = A_0 / \rho_b C_0 \cdot \partial^2 p / \partial x^2 \tag{4.48}$$

where $\rho_b$ and $p$ are the blood density and the blood pressure, respectively; $A_0$ is the cross-section area of the artery at diastolic pressure; and $C_0$ is the arterial compliance, which is defined as the ratio of the maximum area change ($\Delta A$) to the pulsatile pressure amplitude ($\Delta p$) in the artery [3]:

$$C_0 = \Delta A / \Delta p = 2\pi r_0 u_{r0} / \Delta p \tag{4.49}$$

Based on Eq. (4.48), the pressure gradient in Eq. (4.43) is used to represent the pulsatile pressure amplitude. Then, arterial compliance is estimated as:

$$C_0 \propto \frac{2\pi r_0 u_{r0}}{\Delta P_x} \propto \frac{u_{r0} \cdot \left(v_{\max}\right)^{1/4}}{\left\{\left(a_{\max} - a_{\min}\right) \cdot \frac{\Delta t}{T}\right\}^{5/4}} \tag{4.50}$$

The Pulse Wave velocity (PWV) is related to the arterial compliance by:

$$PWV = \sqrt{\frac{A_0}{\rho_b C_0}} \tag{4.51}$$

Consequently, the PWV is estimated as:

$$PWV \propto \left[\frac{a_{\max} - a_{\min}}{v_{\max}} \cdot \frac{\Delta t}{T}\right]^{-1/8} \cdot \left[\frac{\left(a_{\max} - a_{\min}\right) \cdot \Delta t / T}{u_{r0}}\right]^{1/2} \tag{4.52}$$

The PWV is related to the effective incremental elasticity by Eq. (1.1):

Thus, the effective incremental elasticity is estimated as:

$$E_{\theta\theta} \propto PWV^2 \cdot r_0 \tag{4.53}$$

Based on Eq. (4.32), (4.45), (4.47), and (4.53), the three arterial wall parameters: radius, elasticity, and viscosity can be estimated from the damping coefficient and spring stiffness:

$$r_0 \propto 1/\sqrt[4]{D} \tag{4.54}$$

$$E_{\theta\theta} \propto K \cdot r_0^2 \propto PWV^2 \cdot r_0 \propto \frac{K}{\sqrt{D}} \tag{4.55}$$

$$\eta_{\theta\theta} \propto D \cdot r_0^2 \propto \sqrt{D} \tag{4.56}$$

Based on Eq. (4.36) and (4.37), the damping coefficient and spring stiffness are estimated from the key features in the arterial radius waveform and its derivatives in Figure 4.4. Since only the ratios of the key features are used for estimation of *D* and *K*, no calibration is needed to obtain the absolute value of the radius waveform. Evidently, the estimated values of arterial wall parameters are relative, not absolute, and thus have no units. As long as these estimated relative values are capable of tracking changes of arterial wall parameters for early risk prediction of cardiovascular events, the goal of the proposed solution for home use is achieved [93].

## 4.5 Conclusion

In this chapter, the model-based method for estimating arterial wall parameters is presented. The analysis of radial and longitudinal motion of the arterial wall in the context of pulsatile pressure and flow is conducted. Due to the time-harmonic nature of the radial wall motion, the arterial wall is modeled as a second-order dynamic system. Combining the dynamic model with a hemodynamic model of the blood flow in the artery; the arterial wall parameters are expressed by the spring constant and damping coefficient.

# CHAPTER 5

# ESTIMATION OF ARTERIAL WALL PARAMETERS FROM MEASURED ARTERIAL PULSE SIGNALS

This chapter presents the estimation of arterial wall parameters from measured arterial pulse signals on subjects at different arteries by the model-based method. The arterial wall parameters were extracted from the measured pulse signals on seven subjects at RA and STA using a Pyrex-based tactile sensor. Subject-specificity and artery-site-specificity plays a role in the measurement, which makes parameters not suitable for comparison between subjects and arteries. Tracking changes in arterial wall parameters is then introduced via moderate exercise. The changes in arterial wall parameters before and post-exercise from five subjects at RA and CA were analyzed. There are still some factors that may influence the measured results in the arterial pulse measurement, the experiments were carried out for analyzing these factors separately.

## 5.1 Estimation of Arterial Wall Parameters from Measured Signals on Subjects At-Rest

### 5.1.1 Subject Recruitment and Measurement Protocol

Data collection from subjects and the protocol of arterial pulse measurement for this research is approved by institutional view boards (IRB) at Old Dominion University. Enrollment includes all male and female adults. All the individuals will be given enough time to read and understand the informed consent forms with opportunities to withdraw at any time during the experiment. Voluntary informed consent and a screening questionnaire are prerequisites for a subject's participation in this research. Subjects were all healthy, non-smoking, volunteers recruited from campus, with no history of severe disease or other clinically significant condition, no injuries and taking no regular medications in five days.

Pulse signals at RA and STA on the right side of seven healthy subjects in the sitting position were measured at-rest using a microfluidic-based tactile sensor built on Pyrex substrate. The measurement protocol and data acquisition system for obtaining arterial pulse signals is the same as the one described in Section 3.1. The demonstration for arterial pulse measurement at three arterial sites using the sensor built on a Pyrex substrate is shown in Figure 5.1. The Pyrex-based tactile sensor is placed at the site of three different locations: RA, CA, and STA with two fingers pressed against the artery region. The arterial pulse exerts a time-varying deflection on the top of the PDMS microstructure, which registers as a resistance change, $\Delta R$, by the transducer at the site of the artery. The sensor does not pose any risk to the subject, except slight pressure at the artery region, similar to pulse-taking by a nurse during a doctor visit. Note that the hold-down pressure against an artery is uncontrollable.

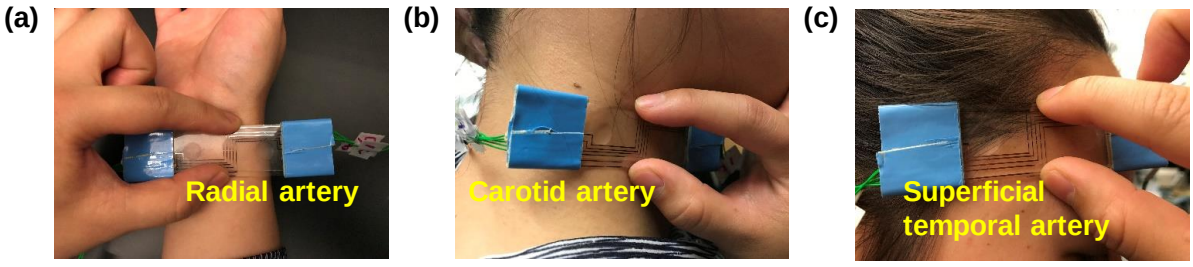


Figure 5.1 Demonstration of how the sensor is held for (a) RA (b) CA and (c) STA pulse measurement with two fingers holding the sensor above the artery.

5.1.2 Results

The arterial radius waveforms and derivatives measured on the 41yr-F subject are illustrated in Figure 5.2. Based on the dynamic modeling of the radial wall motion described in Chapter 4, a simple algorithm is written in Matlab to extract the key features from an arterial radius waveform and its derivatives. To minimize errors, the average of the extracted features from five pulse cycles were used.

The hold-down pressure influences the transmission of the pulsatile pressure signal in an artery to the sensor through the neighboring tissue. Thus, the amplitude of a measured pulse signal varies with the hold-down pressure used. However, since the three physical properties of the arterial wall are estimated by using the ratio of the radius waveform and its two derivatives, no calibration is needed for obtaining the absolute value of the pulse amplitude.

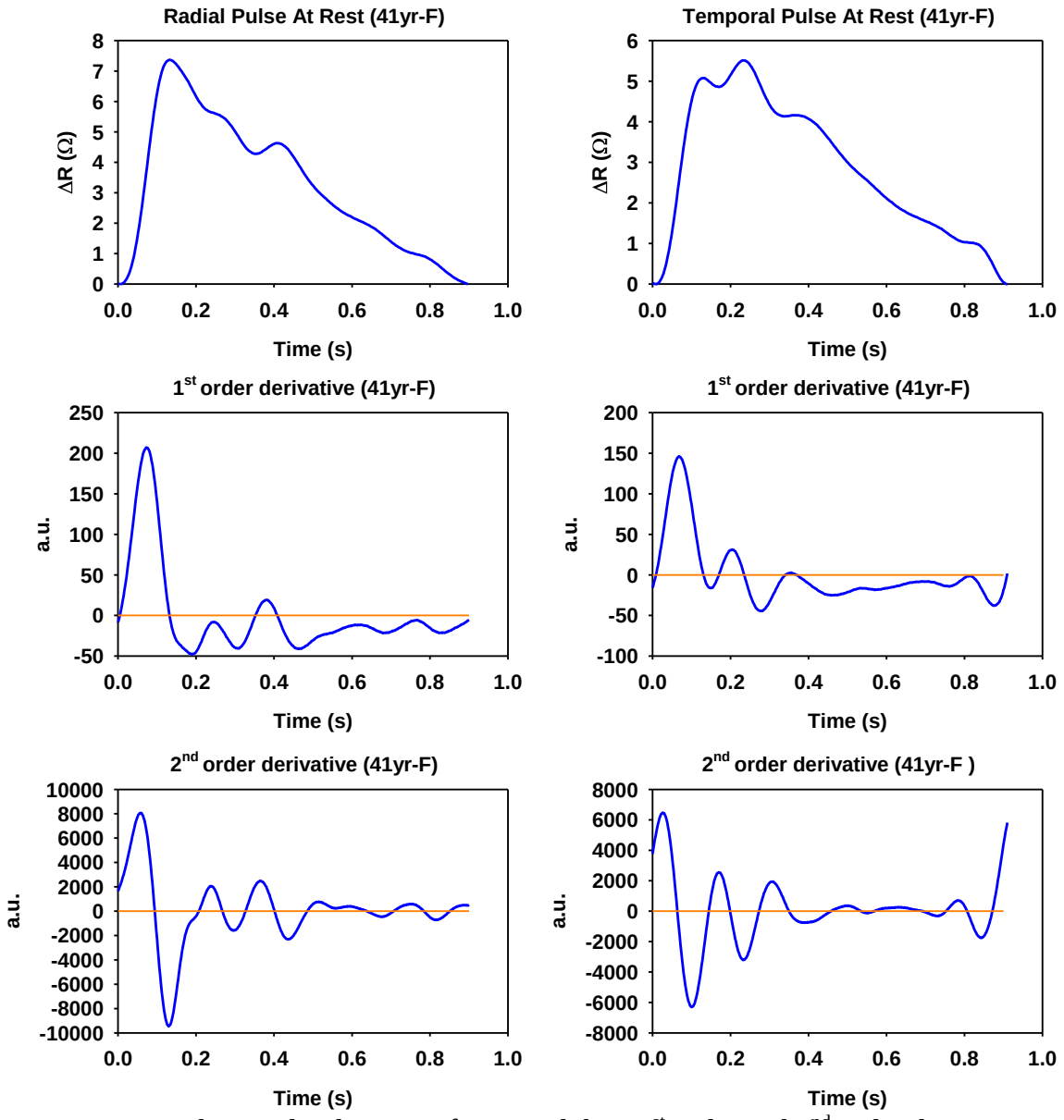


Figure 5.2 Measured arterial radius waveforms and their 1st-order and 2nd-order derivatives at the radial and superficial temporal arteries of the 41yr-F subject.

As shown in Figure 5.2, the measured radius waveform captured the expected difference in pulse waveform between RA and STA. The upstroke swing in the radial pulse is steep but is inclined in the superficial temporal pulse, owing to the proximity of the latter artery to the heart. The diastolic notch in the radial pulse is lower than the one in the superficial temporal pulse. Therefore, the estimated wall properties are expected to capture the difference between the RA and STA.

As summarized in Table 5.1, there is a moderate difference in $E_{\theta\theta}$ and $\eta_{\theta\theta}$ between the two arteries, but a large difference among the subjects. This is believed to be caused by the small absolute values of wall viscosity, relative to the value of wall elasticity. As shown in Figure 5.3, the measure wall elasticity and viscosity at RA and STA both reveal a relatively positive trending with BMI, but not age. Due to the small sample size (n=7), no positive correlation of the elasticity and viscosity with BMI can be obtained. In a study on 120 men and 276 women, the blood pressure was found to be influenced more by fatness than by age [94]. Since blood pressure is positively correlated to the wall elasticity, our results on seven subjects are consistent with the study on large sample size. It should be pointed out that fatness and age were also found to explain blood pressure values by only 3~30%, because socioeconomic factors and stress on hypertension could be important in an adult population [94].

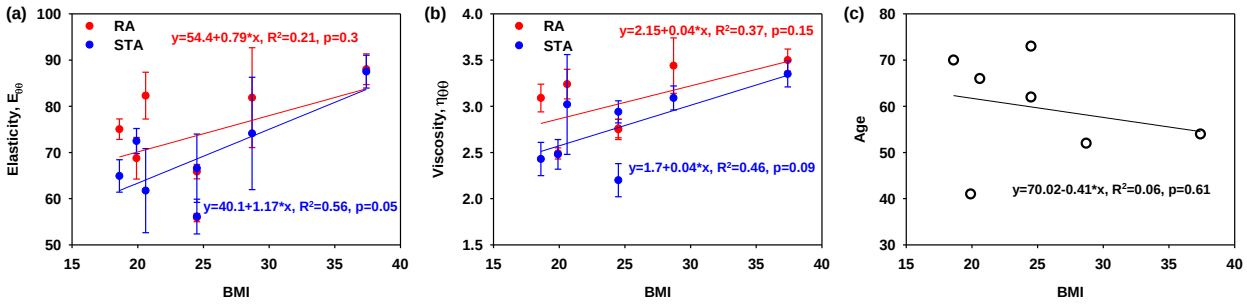


Figure 5.3 Correlation of (a) wall elasticity ($E_{\theta\theta}$) and (b) viscosity ($\eta_{\theta\theta}$) with BMI of seven subjects (c) no correlation of BMI with age.

The estimated values on the dynamic system parameters and the physical properties of the RA and STA of the seven subjects, together with their heart rates and BMI are summarized in Table 5.1. The spring stiffness, damping coefficient, and effective longitudinal stiffness all reveal differences between a superficial temporal artery and radial artery, and show the difference between the two subjects. The measured difference validates the feasibility of the proposed solution for monitoring the arterial stiffness and damping at-home.

Note that the estimated value in Table 5.1 of $r_0$ in is indicative of the viscous resistance at the arterial wall or peripheral vascular resistance (PVR), rather than the size of the arterial wall. In other words, a large $r_0$ implies a low PVR. This explains why the estimated $r_0$ is high at STA, but low at RA. In reality, the RA radius and STA radius are 1.2±0.2mm [51] and 0.7±0.2mm [95], respectively. The estimated $r_0$ is used in estimated wall elasticity and viscosity in order to factor in the change in $r_0$ accompanying the change in wall elasticity and viscosity in future studies.

Overall, both spring stiffness and damping coefficient reveal a moderate difference between the two arteries of each subject but a dramatic difference among the subjects. Spring stiffness is proportional to arterial wall elasticity and inversely proportional to the squared arterial radius. While the elasticity at STA is higher than that at RA, the radius at STA is smaller than that at RA. Moreover, overlying tissue at STA is thinner than that at RA. As such, spring stiffness at RA is expected to be higher than that at STA. This is observed in five subjects, while two subjects reveal the opposite. The opposite results in the two subjects are believed to be caused by large variation in $P_{HD}$ used, as compared with the rest subjects, since $P_{HD}$ affects transmural pressure, with the latter significantly affecting the arterial wall elasticity [96, 97].

$P_{HD}$ influences the transmission of the pulsatile pressure signal in an artery to the sensor through overlying tissue and the transmural pressure in the arterial wall. Thus, the amplitude of a measured pulse signal varied with the $P_{HD}$ used. Since the physical properties of the arterial wall were estimated by using the ratio of the radius waveform and its two derivatives, no calibration was needed for obtaining the absolute value of the pulse amplitude. However, $P_{HD}$ affects the measured values by affecting the transmural pressure in the arterial wall. Although the absolute value of the pulse amplitude is not needed in our method, $P_{HD}$ needs to be varied to achieve maximum pulse amplitude at an artery so that the measured values from the pulse waveform with the maximum pulse amplitude can be used for any changes at the same artery.

Table 5.1 Measured spring stiffness, damping coefficient, physical properties, BMI, and heart rate of the arterial wall on the seven subjects.

| Subject | Location | D | K | $\eta_{\theta\theta}$ | $E_{\theta\theta}$ | $r_0$ | HR | BMI |
|---|---|---|---|---|---|---|---|---|
| 66yr-M | RA | 10.53±1.04 | 267.31±27.07 | 3.24±0.16 | 82.31±5.07 | 0.556±0.014 | 86±5 | 20.6 |
| | STA | 9.34±3.58 | 188.80±56.97 | 3.02±0.54 | 61.73±9.10 | 0.581±0.047 | 77±1 | |
| 70yr-F | RA | 9.55±0.93 | 231.85±15.66 | 3.09±0.15 | 75.05±2.22 | 0.570±0.014 | 81±1 | 18.6 |
| | STA | 5.96±0.94 | 158.19±16.47 | 2.43±0.18 | 64.92±3.53 | 0.642±0.023 | 79±3 | |
| 41yr-F | RA | 6.20±0.28 | 171.15±11.88 | 2.49±0.06 | 68.76±4.50 | 0.634±0.007 | 67±2 | 19.9 |
| | STA | 6.15±0.80 | 179.59±15.23 | 2.48±0.16 | 72.49±2.72 | 0.636±0.022 | 67±2 | |
| 73yr-M | RA | 7.62±0.55 | 181.76±9.57 | 2.76±0.10 | 65.86±1.56 | 0.602±0.011 | 62±2 | 24.5 |
| | STA | 4.85±0.77 | 123.77±18.08 | 2.20±0.18 | 56.12±3.76 | 0.676±0.027 | 62±2 | |
| 54yr-F | RA | 12.25±0.86 | 307.78±9.48 | 3.50±0.12 | 88.03±3.33 | 0.535±0.009 | 99±2 | 37.4 |
| | STA | 11.21±0.95 | 293.02±22.30 | 3.35±0.14 | 87.50±3.55 | 0.547±0.012 | 95±3 | |
| 62yr-M | RA | 7.57±0.60 | 153.65±6.70 | 2.75±0.11 | 55.89±0.89 | 0.603±0.012 | 74±1 | 24.5 |
| | STA | 8.67±0.73 | 196.21±25.20 | 2.94±0.12 | 66.60±7.40 | 0.583±0.012 | 75±1 | |
| 52yr-M | RA | 11.89±2.05 | 281.94±47.11 | 3.44±0.30 | 81.87±10.81 | 0.541±0.024 | 92±5 | 28.7 |
| | STA | 9.56±0.83 | 230.28±48.07 | 3.09±0.13 | 74.12±12.16 | 0.568±0.014 | 84±2 | |

## 5.2 Changes in Arterial Wall Parameters from Measured Signals on Subjects At-Rest and Post-Exercise

A measured pulse signal is a combination of the sensor, $P_{HD}$, the subject-specific parameters (i.e., overlying tissue and blood pressure) and the arterial wall, the measured

difference in the two physical properties is not suitable for comparison between different arteries and different subjects unless $P_{HD}$ is well controlled and the influence of the sensor design and subject-specific parameters are considered. As such, the measured difference demonstrates the necessity of subject-specific and artery-site-specific measurements for arterial stiffness and damping. Due to the variations in overlying tissue thickness and sensor designs, the estimated arterial stiffness may be unpractical for representing the absolute arterial stiffness and comparing between subjects. Instead, the adaption of the estimated arterial stiffness to moderate exercise is proposed to capture the cardiovascular health of a subject and the difference in cardiovascular health among subjects.

### 5.2.1 Subject Recruitment and Measurement Protocol

This study was approved by the IRB of Old Dominion University for measuring the arterial pulse signals on subjects before and post moderate exercise. The age range of subjects for conducting the exercise session will be 18-50. A questionnaire form and informed consent document are provided before the arterial pulse measurement. Subjects who ever felt pain in their chest, or suffered from shortness of breath, or feel headedness and dizziness, when doing physical exercise will be excluded from the study.

Five healthy subjects gave written informed consent to participate in the study. Moderate exercise was used to introduce changes in arterial wall parameters from the measured signals on subjects. The subject characteristics are summarized in Table 5.2. Pulse signals at the radial and carotid arteries on the right side of the body were measured pre-exercise. Afterward, a subject did moderate exercise for 5min. His/her pulse signals were then measured at different times post-exercise, such as 1min, 5min, 10min, 15min, and 25min. In a pulse measurement, the sensor was placed on top of an artery. Then, the sensor was held and pressed against the artery by two

fingers. A LabVIEW program was turned on to record a pulse signal for 1min at a sampling rate of 1kHz. Owing to motion artifacts from a subject under measurement (e.g., respiration and body shifting) and jittering of the holding fingers, $P_{HD}$ varied unavoidably among pulse cycles in a recorded pulse signal. The transducer aligned above the artery gave rise to a pulse signal with the highest amplitude that was used for data analysis.

Table 5.2 Subject Characteristics.

| | Gender | Age (yr) | Height (m) | Weight (Kg) | BMI |
|---|---|---|---|---|---|
| 1 | M | 29 | 178.0 | 81.7 | 25.8 |
| 2 | M | 38 | 172.7 | 74.8 | 25.1 |
| 3 | M | 41 | 180.3 | 88.0 | 27.1 |
| 4 | M | 47 | 167.6 | 63.5 | 22.6 |
| 5 | F | 41 | 163.0 | 53.0 | 19.9 |

5.2.2 Results

The related data-processing algorithms were used to remove motion artifacts, extract arterial pulse waveform and heart rate [43]. The extracted pulse waveform was expressed in terms of resistance change ($\Delta R$) and was used to represent the arterial radius waveform [34]. The difference in the measured arterial radius waveform on the 29yr-M subject and its two derivatives at pre-exercise, 1min post-exercise and 5min post-exercise is compared in Figure 5.4, where the radius waveform and its two derivatives are normalized to their own amplitudes. The pulse cycles post-exercise was shortened due to increased heart rate. Based on Eq. (4.36) and (4.37), the key features of the radius waveform and its two derivatives were extracted to estimate $D$ and $K$. Consequently, the arterial wall parameters were estimated using Eq. (4.54), (4.55) and (4.56). The estimated values at an artery were expressed as mean ± standard deviation and were obtained from five consecutive pulse cycles of its recorded pulse signal. The amplitude and time duration of a pulse cycle was normalized to magnify the difference between pre-exercise and

post-exercise of measured pulse signals at RA and CA, which is shown in Figure 5.5. The arterial pulse signals tend to recover during the 5min post-exercise.

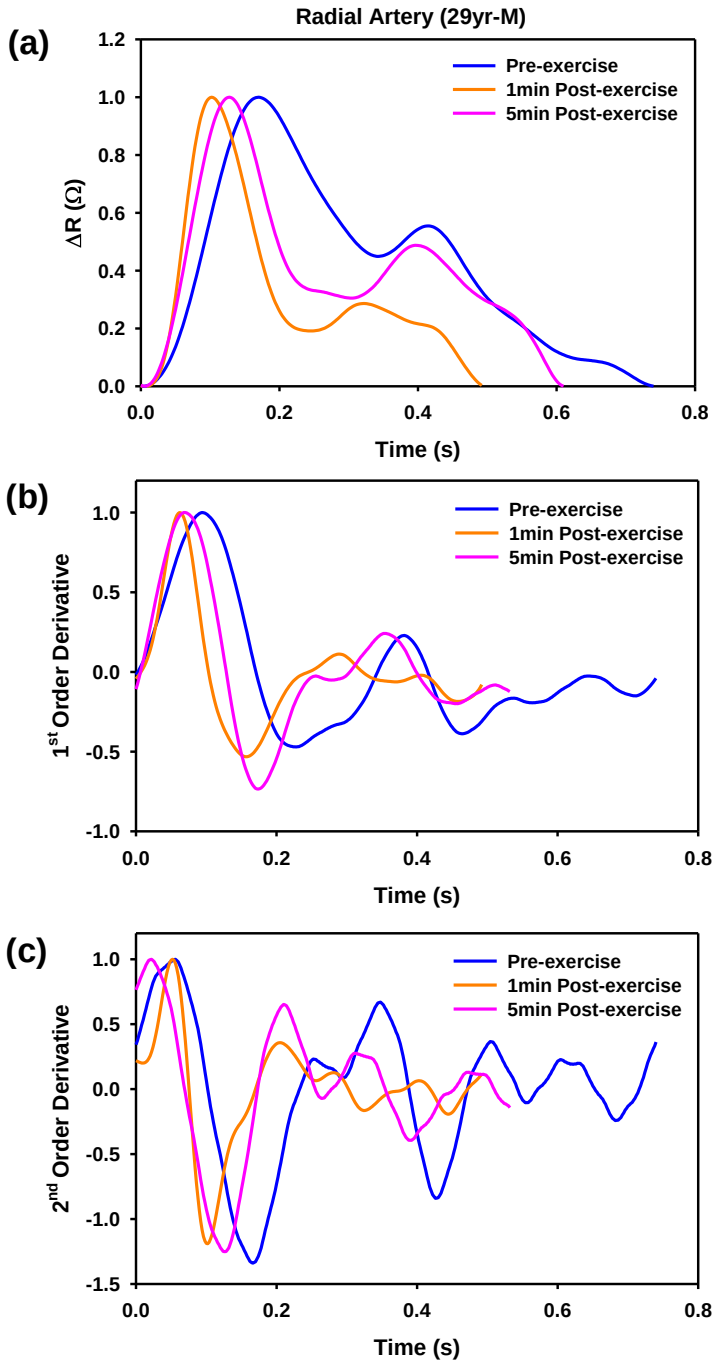


Figure 5.4 Comparison of (a) measured arterial radius waveforms at the radial artery of the 29yr-M subject; (b) its 1st-order derivatives; (c) 2nd-order derivatives between pre-exercise and post-exercise.

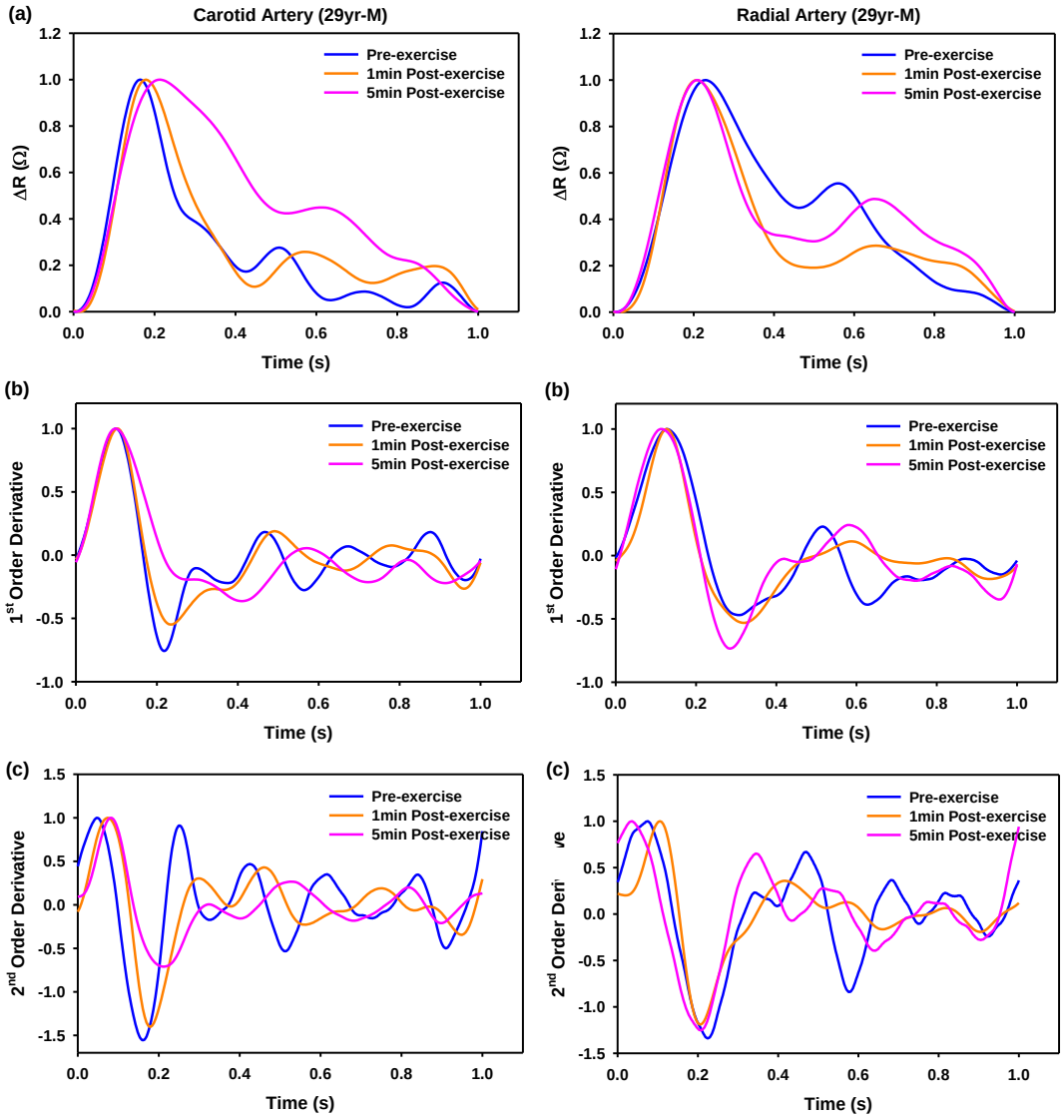


Figure 5.5 Normalized pulse signals for 29yr-M at carotid and radial artery pre-exercise, 1min post exercise, and 5min post exercise. (a) Normalized pulse signals, (b) normalized 1st order derivative signals, (c) normalized 2nd order derivative signals.

As illustrated in Table 5.3, as compared with the estimated values pre-exercise, the wall radius greatly decreased 1min post-exercise and then slowly went up over time post-exercise. In contrast, the wall elasticity and viscosity went up 1min post-exercise and then went down over time. The PWV, associated with the elasticity and the radius, also went up 1min post-exercise and then dropped over time. The two observed changing trends of the wall radius and elasticity

are consistent with the findings in the literature [98-101]. The change of the wall viscosity pre-exercise and post-exercise for humans could not be found in the literature for comparison [102, 103].

Table 5.3 Estimated values of arterial wall parameters, heart rate (HR), PWV and PVR at pre-exercise and their changes relative to pre-exercise at different times post-exercise of the five subjects (a) radial artery (b) carotid artery (values: mean ±standard deviation).

(a) Radial artery

| | Pre-exercise | 1min post-exercise | 5min post-exercise | 10min post-exercise | 15min post-exercise | 25min post-exercise |
|---|---|---|---|---|---|---|
| $r_0$ | 0.60±0.035 | -11%±4% | -8%±9% | -8%±6% | -9%±5% | -6%±6% |
| $E_{\theta\theta}$ | 84.42±13.43 | 55%±38% | 23%±26% | 18%±24% | 18%±22% | 13%±15% |
| $\eta_{\theta\theta}$ | 2.86±0.32 | 28%±11% | 23%±22% | 19%±14% | 23%±12% | 16%±15% |
| HR | 76.61±8.79 | 48%±12% | 25%±12% | 23%±12% | 20%±10% | 13%±10% |
| PWV | 11.85±0.92 | 31%±17% | 9%±24% | 12%±13% | 11%±14% | 8%±11% |
| PVR | 8.26±1.78 | 63%±28% | 54%±52% | 43%±32% | 53%±26% | 35%±33% |

(b) Carotid artery

| | Pre-exercise | 1min post-exercise | 5min post-exercise | 10min post-exercise | 15min post-exercise | 25min post-exercise |
|---|---|---|---|---|---|---|
| $r_0$ | 0.58±0.032 | -7%±3% | -9%±6% | 10%±5% | -5%±4% | -3%±5% |
| $E_{\theta\theta}$ | 88.33±14.43 | 36%±28% | 11%±29% | 14%±34% | 10%±22% | -3%±11% |
| $\eta_{\theta\theta}$ | 3.01±0.31 | 16%±8% | 22%±17% | 24%±13% | 11%±10% | 7%±11% |
| HR | 78.16±10.48 | 53%±11% | 25%±10% | 23%±7% | 21%±5% | 14%±5% |
| PWV | 12.30±1.27 | 20%±13% | 9%±15% | 12%±17% | 7%±12% | 0%±7% |
| PVR | 9.12±1.78 | 35%±18% | 52%±41% | 55%±30% | 25%±22% | 15%±23% |

The arterial wall parameters of three subjects at pre-exercise and different times post-exercise is shown in Figure 5.6. Despite moderately fluctuating over 1min~25min post-exercise, the wall elasticity experienced a sudden jump 1min post-exercise and decreased over time post-exercise, and the wall radius underwent a sudden drop 1min post-exercise and then increased over time for all the subjects. The observed fluctuation over the time duration post-exercise was believed to mainly arise from transmural pressure variation, as will be explained later on.

The estimated values at the radial and carotid arteries between pre-exercise, 1min post-exercise, and 25min post-exercise are compared in Figure 5.7. A significant increase in the wall elasticity and viscosity and a significant decrease in the wall radius were observed from pre-exercise to 1min post-exercise, indicating that the changes of the three wall parameters immediately post-exercise were significant. A significant increase in wall elasticity and HR from pre-exercise to 1min post-exercise, and a significant decrease in the two parameters from 1min post-exercise to 25min post-exercise indicates that the elasticity is proportional to HR, which is shown in Figure 5.7 (b). Although the wall elasticity and heart rate revealed a significant drop from 1min post-exercise to 25min post-exercise, no significant difference of the wall radius and viscosity was observed between 1min post-exercise and 25min post-exercise. This could imply that the wall elasticity and heart rate experience a larger change from exercise and thus take a longer time to recover than the wall radius and viscosity.

The pulse signal in an artery needs to be transmitted to the sensor through the neighboring tissues, which varies among different arteries [53-55] and among different subjects [104-106]. Then, the estimated values of the arterial wall parameters are both artery-site-specific and subject-specific. As such, the estimated values of these parameters are unsuitable for comparison among different arteries and among different subjects. For instance, the estimated values of the wall radius in Figure 5.7 should not be compared for finding which artery has a larger radius. Similarly, the estimated values of the wall elasticity in the Table 5.3 should not be compared for finding which artery is stiffer.

The correlation between the relative change in HR and relative change in wall elasticity at different time post-exercise to the parameters estimated pre-exercise for the four male subjects are shown in Figure 5.8. The linear regression equations for the five data points are presented in

Table 5.4. In the four male subjects, the 38yr-M subject is physically active (exercises regularly) while the 29yr-M subject is physically inactive (exercises less). The slope of the linear regression equation for the 29yr-M subject is found to be the largest, while, the data for the 38yr-M subject exhibits the smallest variation. This can be explained as the changes in HR and wall elasticity is small in the subjects who exercise daily or regularly. The heart adjusts the rapid changes via exercise in those who are physically active.

The correlation between the relative change in HR and relative change in wall viscosity and radius at different time post-exercise to the parameters estimated pre-exercise are shown in Figure 5.9 and Figure 5.10, respectively. The correlation of these parameters was found to be unobvious in the two figures because of the small change in viscosity and radius pre and post-exercise.

The statistical data for the relative change in HR and relative change in arterial wall parameter to the parameters estimated pre-exercise at carotid and radial artery are shown in Figure 5.11. The relative change in wall elasticity and relative change HR shows a slight increase trend at RA and STA in Figure 5.11 (a). But the relative changes in viscosity and radius are scattered randomly in the rest of two figures. The health condition for the four subjects is different from each other, which results in the high standard deviation in parameters estimated from the pulse signals measured post-exercise.

Owing to the variation in neighboring tissues and diastolic pressure between the radial and carotid arteries and among different subjects, the same $P_{HD}$ does not translate to the same $P_T$ for the two arteries and for the five subjects. As mentioned earlier, motion artifacts introduce further variation to the $P_T$ in different pulse cycles of a measured pulse signal. Therefore, it is

unpractical to quantitatively control the $P_T$ in a pulse measurement. As such, the estimated values in this study contain fluctuations resulting from the $P_T$ variation.

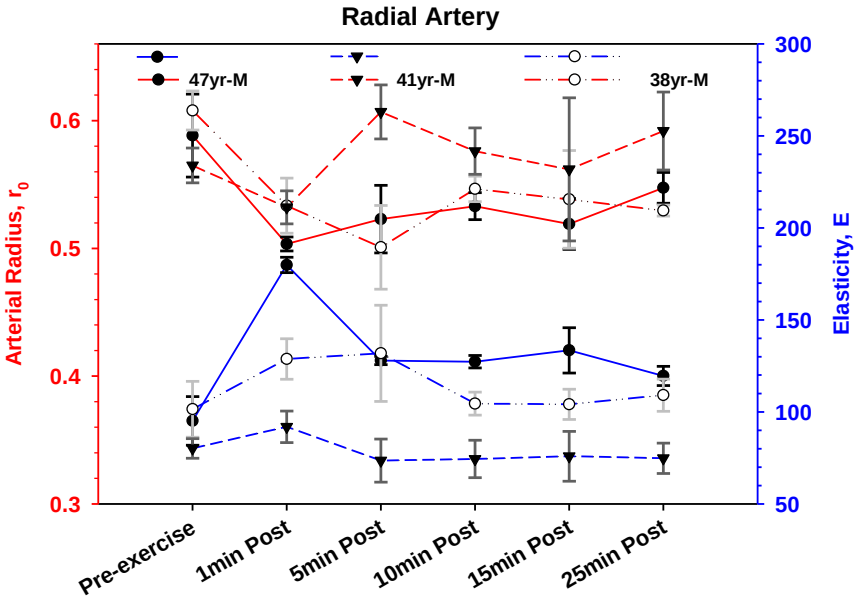


(a)

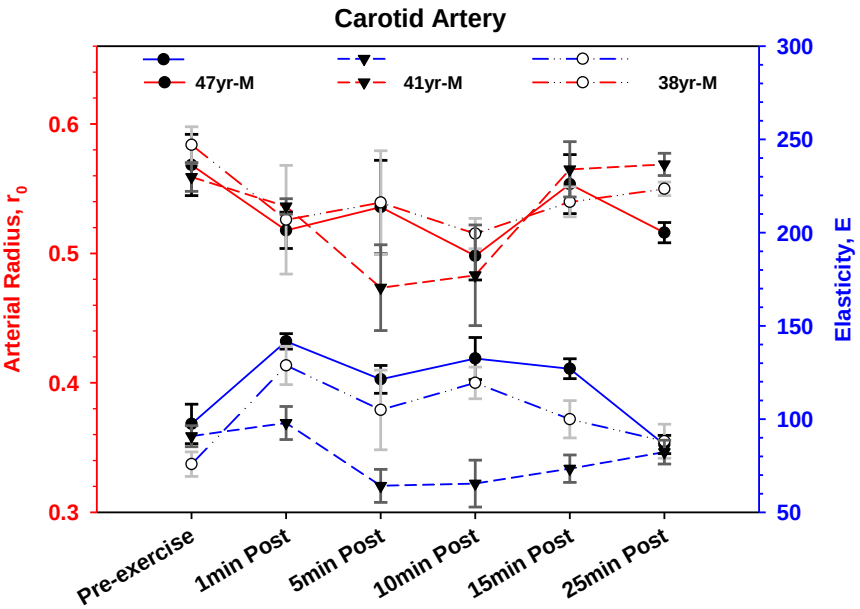


(b)

Figure 5.6 Arterial wall radius and elasticity at pre-exercise, 1min, 5min 10min, 15min, and 25 min post-exercise of the 47yr-M, 41yr-M, and 38yr-M subjects (a) radial artery (b) carotid artery (For clarity, only the values of three subjects are illustrated; values: mean ± standard deviation).

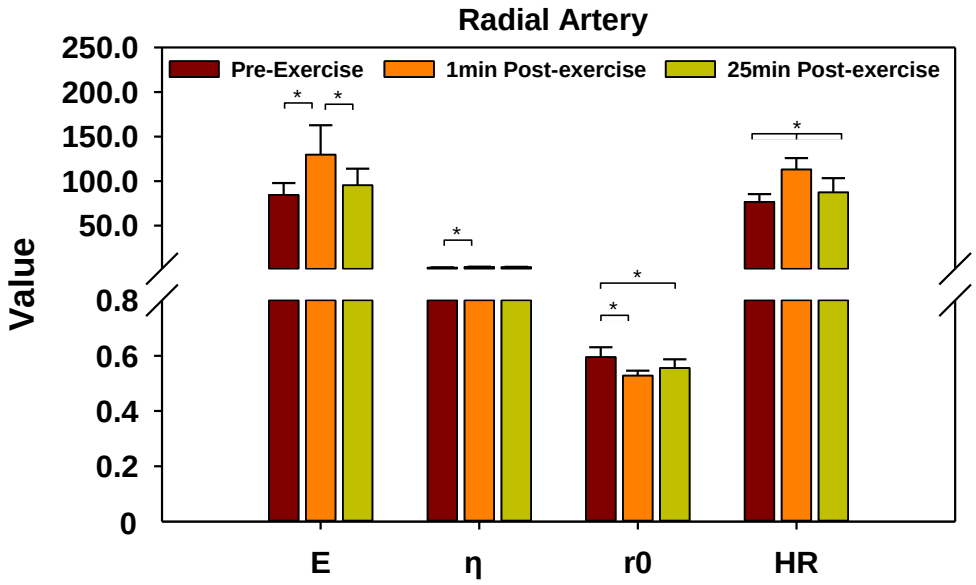


(a)

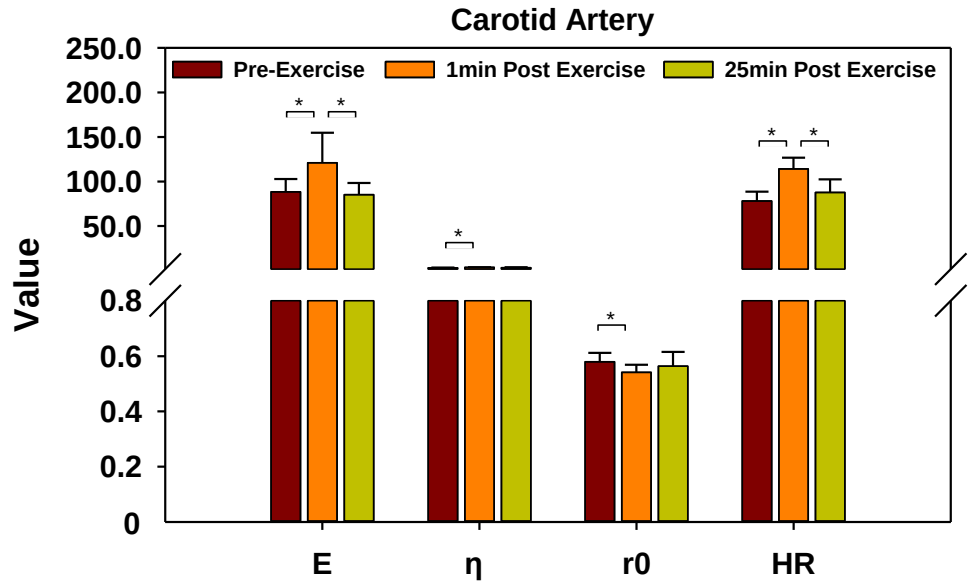


(b)

Figure 5.7 Comparison of arterial wall parameters and heart rate (HR) of the five subjects (n=5) between pre-exercise, 1min post-exercise, and 25min post-exercise (a) radial artery (b) carotid artery (values: mean ± standard deviation). Statistical significance was calculated using paired Student's t-test (*: $p<0.05$).

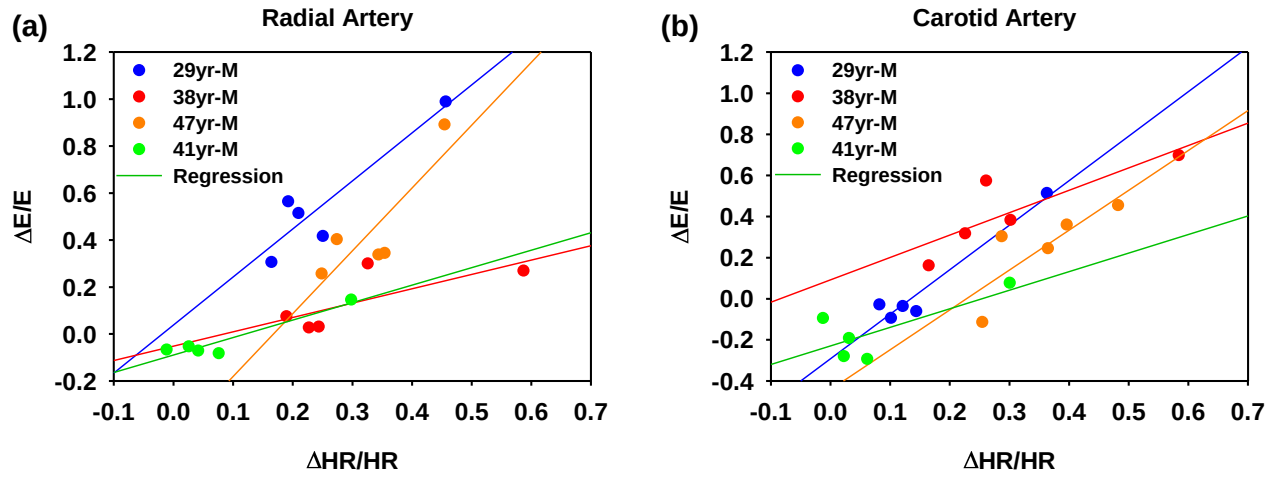


Figure 5.8 The correlation between the changes of heart rate and wall elasticity pre-exercise and post-exercise for four male subjects at radial and carotid artery.

Table 5.4 Linear regression equations for above figure.

| Subjects | Radial | Carotid |
|---|---|---|
| 29yr-M | y=0.0378+2.0444*x, $R^2$=0.84, p=0.0277 | y=-0.2920+2.1656*x, $R^2$=0.94, p=0.0058 |
| 38yr-M | y=-0.0521+0.6115*x, $R^2$=0.54, p=0.1582 | y=0.0925+1.0887*x, $R^2$=0.70, p=0.0779 |
| 47yr-M | y=-0.4479+2.6729*x, $R^2$=0.72, p=0.0698 | y=-0.4423+1.9405*x, $R^2$=0.65, p=0.0991 |
| 41yr-M | y=-0.0898+0.7448*x, $R^2$=0.89, p=0.0159 | y=-0.2295+0.9043*x, $R^2$=0.55, p=0.1508 |

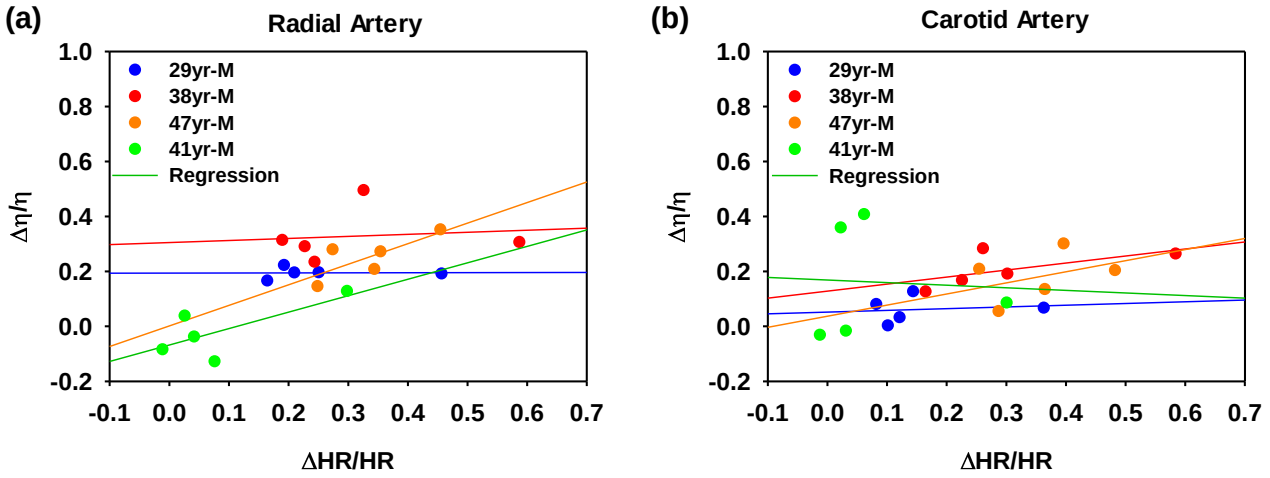


Figure 5.9 The correlation between the changes in heart rate and wall viscosity pre-exercise and post-exercise for four male subjects at radial and carotid artery.

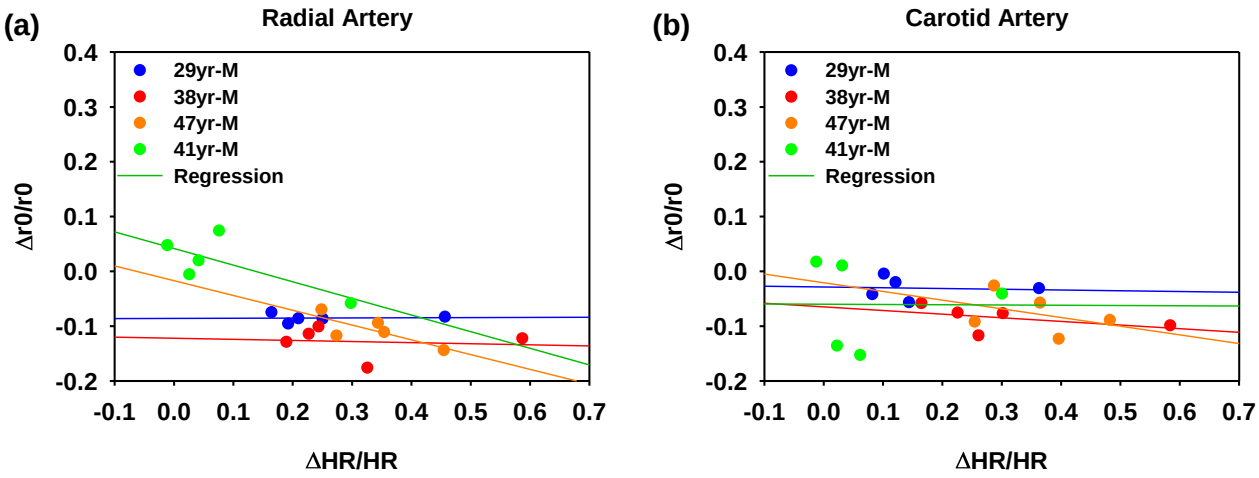


Figure 5.10 The correlation between the changes of heart rate and artery radius pre-exercise and post-exercise for four human subjects at radial and carotid artery.

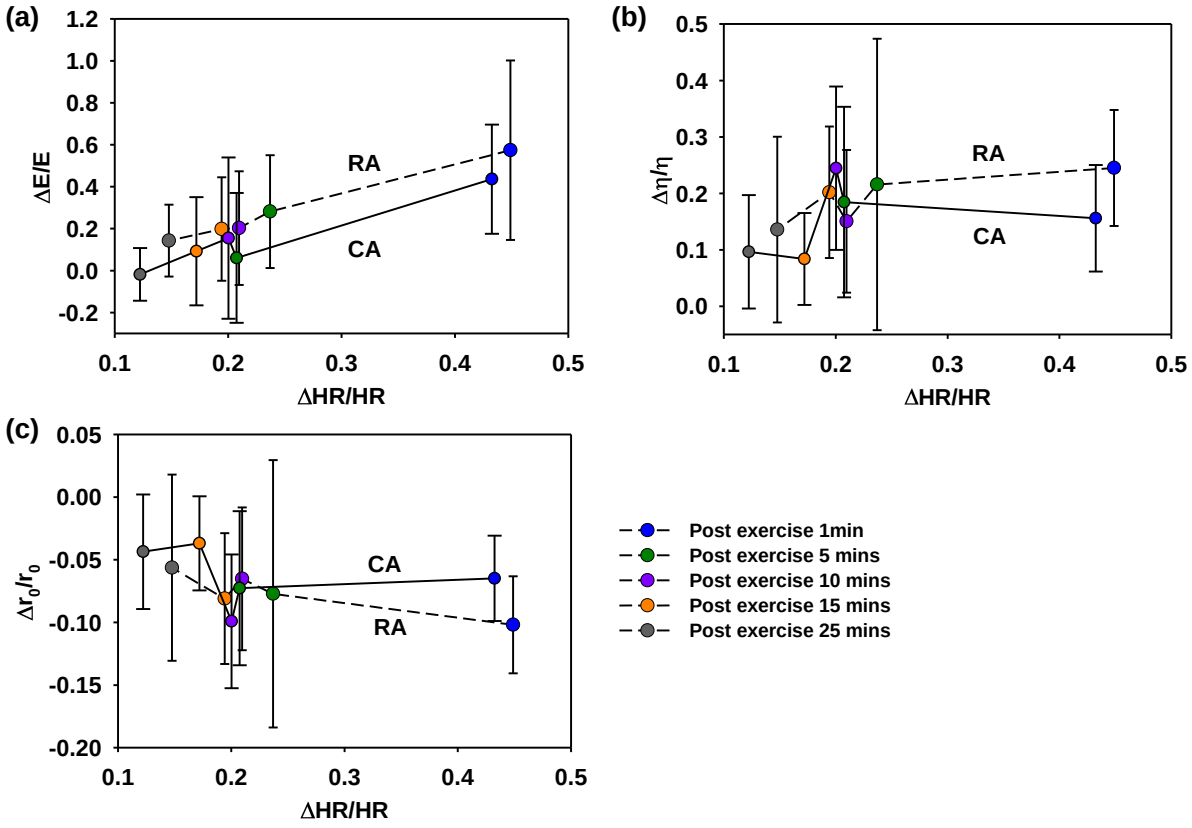


Figure 5.11 The changes of heart rate versus changes of wall elasticity (a), wall viscosity (b) and artery radius (c) at carotid and radial artery post-exercise 1min, 5mins, 10mins, 15mins, and 25mins.

## 5.3 Factors That Influence Arterial Pulse Measurement

### 5.3.1 Effect of Hold-Down Pressure

To examine the effect of hold-down pressure, an experiment is conducted by holding the sensor toward the artery at different strength level. The effect of hold-down pressure on the measured pulse signals at the radial and carotid arteries of the 28yr-F subject is shown in Figure 5.12. These signals are all from the $5^{th}$ transducer and have the same original resistance. Thus, a low resistance indicates high hold-down pressure. In Figure 5.12 (a), as the hold-down pressure goes up, the absolute resistance drops. However, as shown in Figure 5.12 (b), the high hold-down pressure does not result in a stronger pulse signal. In contrast, the low hold-down pressure yields the strongest pulse signal. As shown in Figure 5.12 (b), high hold-down pressure may block the blood flow, and then weaken the pulse signal. As the hold-down pressure is reduced, the blood flow can relatively freely flow through the radial artery and then strengthen the pulse signal. The normalized pulse waveforms in Figure 5.12 (c) show that the H1/H5 ratio in the strongest pulse signal is well above the one in the other two pulse signals. This indicates that the systolic peak is suppressed severely at high and medium hold-down pressure, but it is not suppressed much at low hold-down pressure. Also, owing to its weakness, the pulse signal at high hold-down pressure is noisier than the other two signals.

Interestingly, as to the carotid artery, a high hold-down pressure translates to a strong pulse signal, as shown in Figure 5.12 (d) and (e). From the normalized pulse waveforms in Figure 5.12 (f), it is clear that the stronger the pulse signal is, the less noisy it is. The difference in the effect of hold-down pressure on pulse signals between the radial and carotid artery can be explained by these three reasons: 1) the carotid artery has a diameter (~6.1mm) roughly three times larger than the diameter (~2.3mm) of the radial artery; 2) the radial artery is closer to the

skin, but the carotid artery is deep under the skin; and 3) further away from the heart than the carotid artery, the radial artery demands a higher systolic pressure for blood flowing through it. As such, a high hold-down pressure can easily suppress the blood flow and consequently weaken the pulse signal at the radial artery, while without interfering much with the blood flow in CA.

According to Eqs. (2.2) and (2.4), the difference between the original resistance and the initial resistance of a transducer is indicative of the hold-down pressure, $P_{HD}$:

$$P_{HD} \propto R_0 - R_0' \tag{5.1}$$

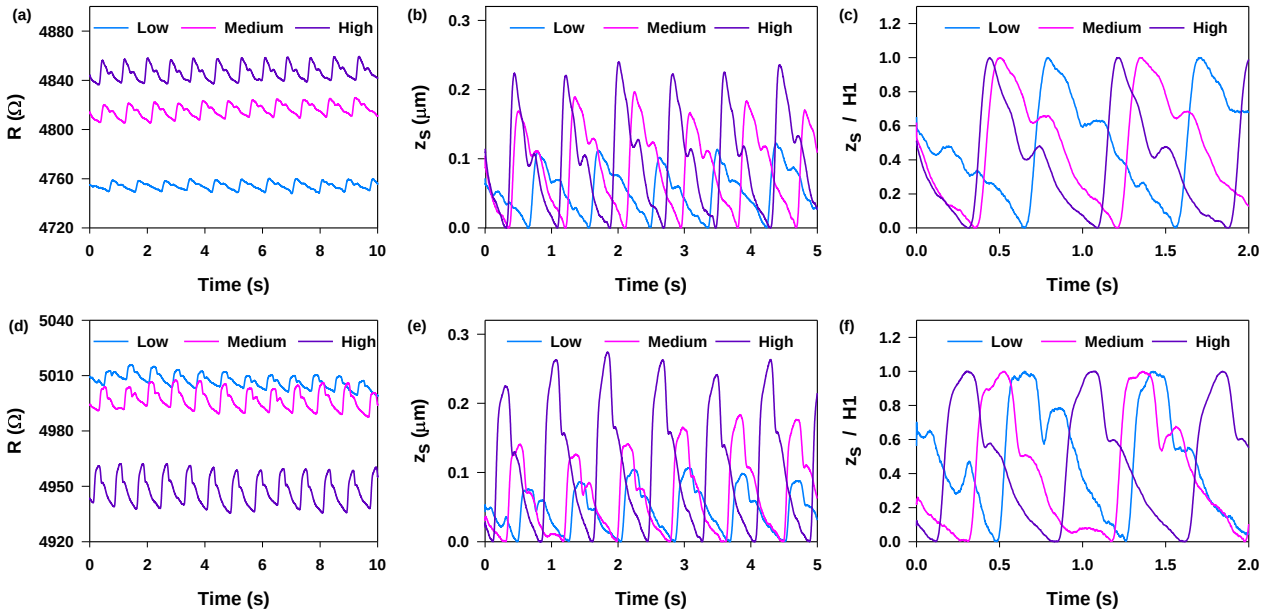


Figure 5.12 Absolute resistance, sensor deflection of pulse waveform and local enlarged view of the normalized pulse waveform under different hold-down pressure: Low, Medium, and High for radial artery (a)-(c) and carotid artery (d)-(f) of the 28yr-F subject.

The H1/H5 ratio and the AI of the radial and carotid pulse signals of the 28yr-F and 28yr-M subjects measured at different hold-down pressure are summarized in Table 5.5. Note that the radial H1/H5 ratio of the 28yr-M subject shows the same correlation with the hold-down

pressure as the 28yr-F subject, but his carotid H1/H5 ratio does not show correlation with the hold-down pressure variation, which happens to be very small.

The hold-down pressure inevitably fluctuates with time in a measured pulse signal. How the pulse strength (or amplitude) varies with the hold-down pressure in the radial and carotid pulse signals of the 28yr-F subject measured at low and high hold-down pressure is examined in Figure 5.13. As the hold-down pressure fluctuates, the pulse strength also varies with time. However, there is no direct correlation between them, which might be caused by nonlinear and viscoelastic tissues in between, through which a pulse signal needs to travel to reach the sensor.

Table 5.5 Comparison of the parameters of the pulse signals of the 28yr-F and 28yr-M subjects measured under different hold-down pressure.

(a)

| | 28yr-F | | | | | |
|---|---|---|---|---|---|---|
| | Hold-down pressure (Ω) | | | | H1/H5 | AI(%) |
| | P[a] | $R_0$ | Avg($R'_0$) | $R_0$-Avg($R'_0$) | | |
| RA | H[b] | 5788 | 4749 | 1039 | 1.53 | 81.21 |
| | M[c] | 5788 | 4808 | 980 | 1.48 | 85.65 |
| | L[d] | 5788 | 4839 | 949 | 1.96 | 79.83 |
| CA | H | 5788 | 4938 | 850 | 1.66 | 13.19 |
| | M | 5788 | 4990 | 798 | 1.60 | 10.29 |
| | L | 5788 | 5003 | 785 | 1.56 | 19.80 |

(b)

| | 28yr-M | | | | | |
|---|---|---|---|---|---|---|
| | Hold-down pressure (Ω) | | | | H1/H5 | AI(%) |
| | P | $R_0$ | Avg($R'_0$) | $R_0$-Avg($R'_0$) | | |
| RA | H | 6938 | 6476 | 462 | 1.78 | 63.03 |
| | M | 6938 | 6487 | 451 | 1.89 | 57.77 |
| | L | 6938 | 6510 | 428 | 2.01 | 60.70 |
| CA | H | 5788 | 4848 | 940 | 1.59 | -10.86 |
| | M | 5788 | 4852 | 936 | 1.43 | -7.07 |
| | L | 5788 | 4853 | 935 | 1.49 | -14.04 |

a: Pressure; b: High; c: Medium; d: Low

The H1/H5 ratio and the AI of the radial and carotid pulse signals of the 28yr-F and 28yr-M subjects measured at different hold-down pressure are summarized in Table 5.5. Note that the

radial H1/H5 ratio of the 28yr-M subject shows the same correlation with the hold-down pressure as the 28yr-F subject, but his carotid H1/H5 ratio does not show correlation with the hold-down pressure variation, which happens to be very small. Both the H1/H5 ratio and the AI of the two subjects fluctuate with the hold-down pressure.

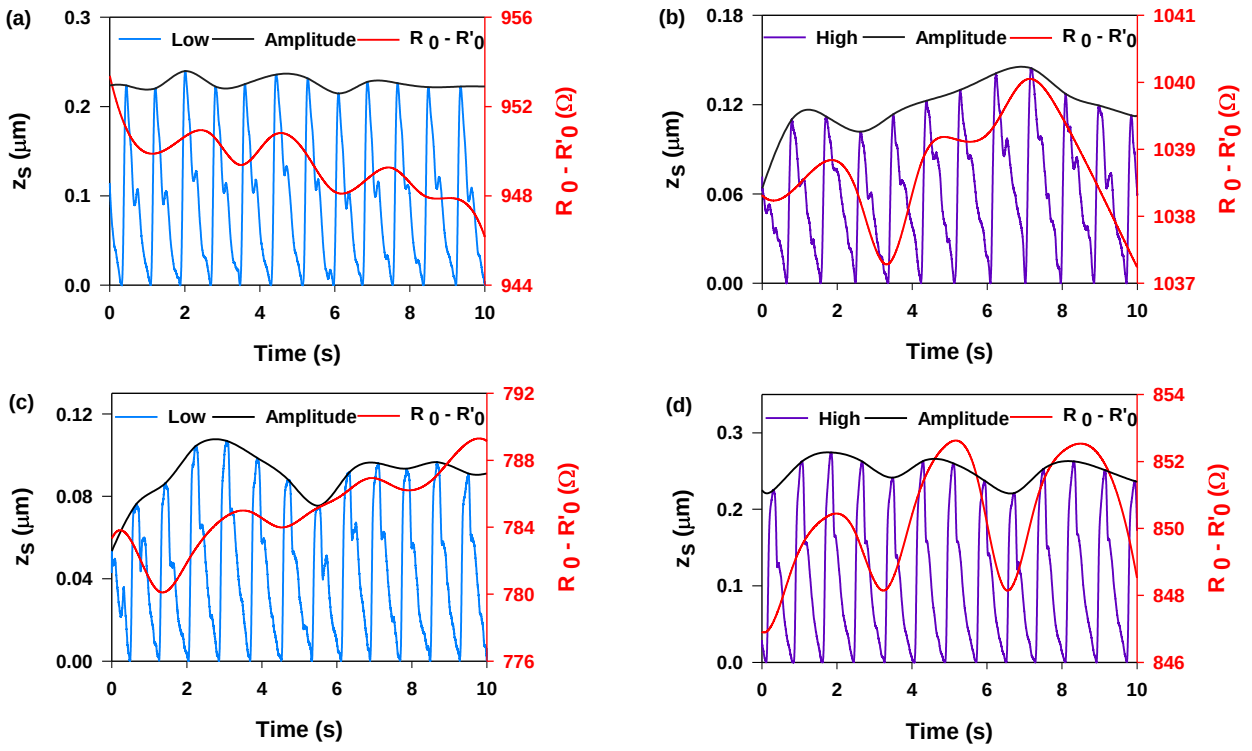


Figure 5.13 The amplitude of sensor bottom deflection versus resistance change between original resistance and initial resistance under Low and High hold-down pressure for radial artery (a) (b), and carotid artery (c) (d) of the 28yr-F subject.

Taken together, the hold-down pressure has a profound effect on a measured pulse signal, in terms of its strength and its waveform [107]. Then, the question arises: what hold-down pressure is appropriate for acquiring a good pulse signal. If a good pulse signal is deemed as a signal with minimum noise and minimum distortion from the sensor-artery interaction, then the best way to find an appropriate hold-down pressure is to measure the pulse signal at an artery at different hold-down pressure and identify the measured strongest pulse signal as the good pulse

signal. Certainly, measurements on a large number of subjects need to be carried out to validate this conclusion. Meanwhile, the appropriate hold-down pressure for acquiring a good pulse signal is expected to vary among subjects, simply because a large individual variability exists in tissues between the sensor and the artery and the pulse strength. The transmural pressure is the pressure difference between the two sides of the arterial wall. It is expressed as $P_T=P_{ext}-P_d$, where $P_{ext}$ is pressure outside the arterial wall and $P_d$ is the diastolic pressure. The wall exhibits the lowest elasticity when the artery is under zero transmural pressure. The transmural pressure is either negative or positive and will affect the measured results. The pulse signals need to be measured under zero transmural pressure to avoid the distortion of the pulse signals.

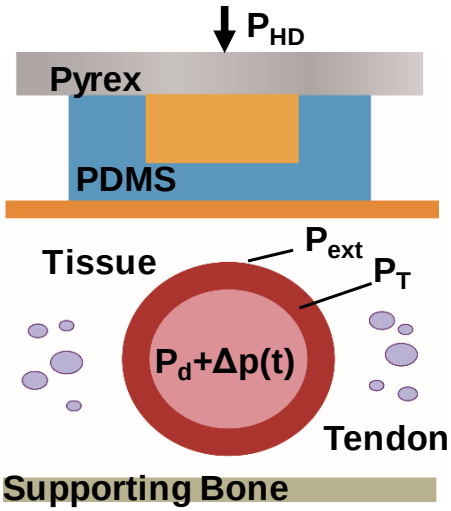


Figure 5.14 Demonstration of the forces exerted on the arterial wall.

5.3.2 Effect of Sensor Sensitivity

The sensitivity of the sensor affects the measured results. High sensitivity may lead to weak results, while sensor with relatively low sensitivity may capture clear pulse signals. To further analyze the effect of the sensitivity of the sensor on measured results, an experiment is designed to track the change of the cardiovascular system on the rabbit after drug injection using

a microfluidic-based tactile sensor. The primary objective is to conduct arterial pulse signal measurements on rabbits using a microfluidic-based tactile sensor and derive the associated physiological parameters from the measured pulse signals using signal-processing algorithms, for evaluating the effectiveness of the measured pulse signals in inferring changes in the cardiovascular system of a rabbit. Phenylephrine has been widely used in clinical practice to treat perioperative hypotension. It has a vasoconstriction effect on arteries, which increases the blood pressure and reduces the arterial radius.

The experiment collaborates with Eastern Virginia Medical School (EVMS). The approval and experiment related training are completed before the experiment. Female white New Zealand rabbits is used for the experiments described below. The experiments are all acute procedures in which the animals will be anesthetized with isoflurane (initial 5%, maintenance 1-3%) prior to testing non-invasive microfluidic-based tactile sensors. Acute or chronic animal impairment is not anticipated. If infection or complications do occur, the animals will be treated in consultation with the staff of the Division of Comparative Medicine. After reaching the surgical anesthesia plane, an IV line with saline drip will be placed in the ear vein. Then, baseline pressure cuff and pulse oximeter measurements are obtained.

After this initial measurement, the rabbit’s thigh will be shaved to permit the sensor to contact the skin. The test sensor will then be placed on the skin and held in place, which permits secure contact and can be removed without damaging the epidermis. After 3 baseline sensor measurements are made and comparison with a pulse oximeter and pressure cuff measurements has been confirmed, the next step will be to increase or decrease heart rate and blood pressure through the IV administration of short-acting drugs through the ear vein line.

Three injections were conducted in the experiment with 0.1mg, 0.3mg, and 0.4mg, respectively. The agents will be dissolved in sterile saline (0.9%) and administered IV bolus using a 27 gauge needle on a tuberculin syringe. At the completion of the experiment, isoflurane will be discontinued and the animal will be monitored until fully recovered, as determined by the ability to move freely about the cage.

The measured results from sensors with high or low sensitivity are demonstrated in Figure 5.15 and Figure 5.17, respectively. The measured signal from the sensor with high sensitivity exhibits fluctuating signals, while the other one captures a clear pulse wave. The sensor was placed on the right front thigh of the rabbit, the overlying tissue between the skin and artery is thinner than other parts. Therefore, the sensor with high sensitivity may result in distorted signals. A minor change of the hold-down pressure may lead to a large fluctuation of the pulse signals; thus, the pulse signal is diminished in the measurement. The first order and second order derivative of two arterial pulse cycles before drug injection are shown in Figure 5.18.

The estimated arterial wall parameters from the measured signals of a rabbit before and after each injection are presented in Table 5.6. The heart rate recorded by the tactile sensor is almost the same as the one measured with the medical instrument. While the medical instrument recorded an increase in heart rate and blood pressure, the tactile sensor captured a decreasing arterial radius, increasing PWV and increasing PVR. The results reveal that the tactile sensor is capable of tracking minimal changes in small animals with a higher heart rate. The sensor with high sensitivity may obtain distorted pulse signals, while the sensor with lower sensitivity may accommodate the high-frequency heartbeat for small animals.

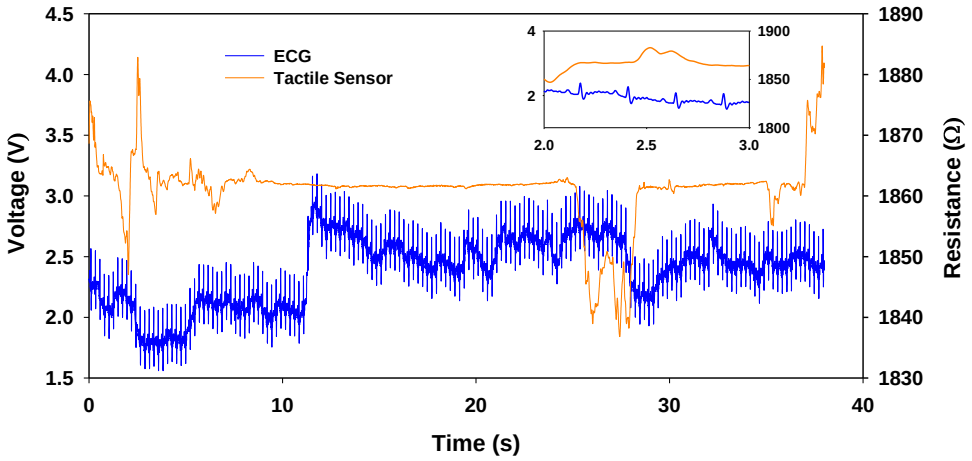


Figure 5.15 The measured results from microfluidic-based tactile sensor and ECG medical device before drug injection using sensor with higher sensitivity.

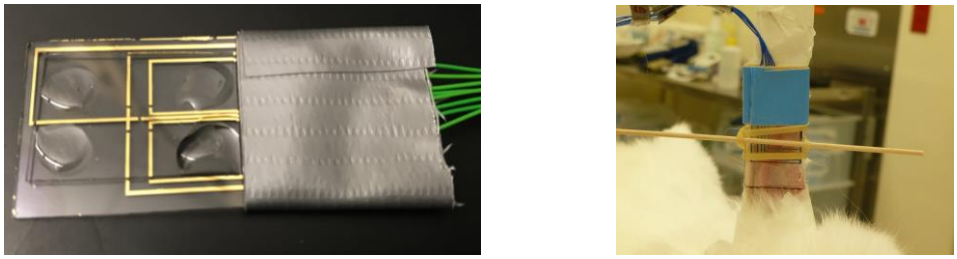

(a) (b)

Figure 5.16 (a) Schematic of sensor design with relatively high sensitivity, (b) the tactile sensor is attached on the front leg of a rabbit.

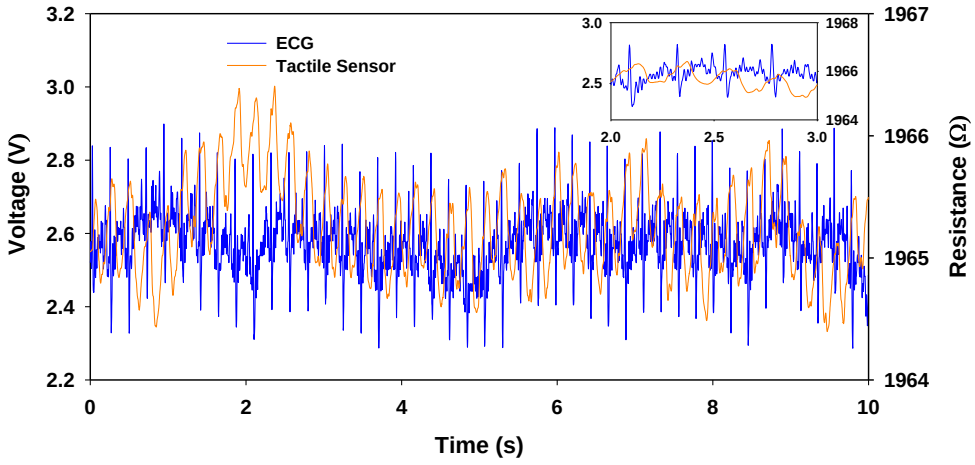


Figure 5.17 The measured results from a microfluidic-based tactile sensor and ECG medical device before drug injection using a sensor with relatively low sensitivity.

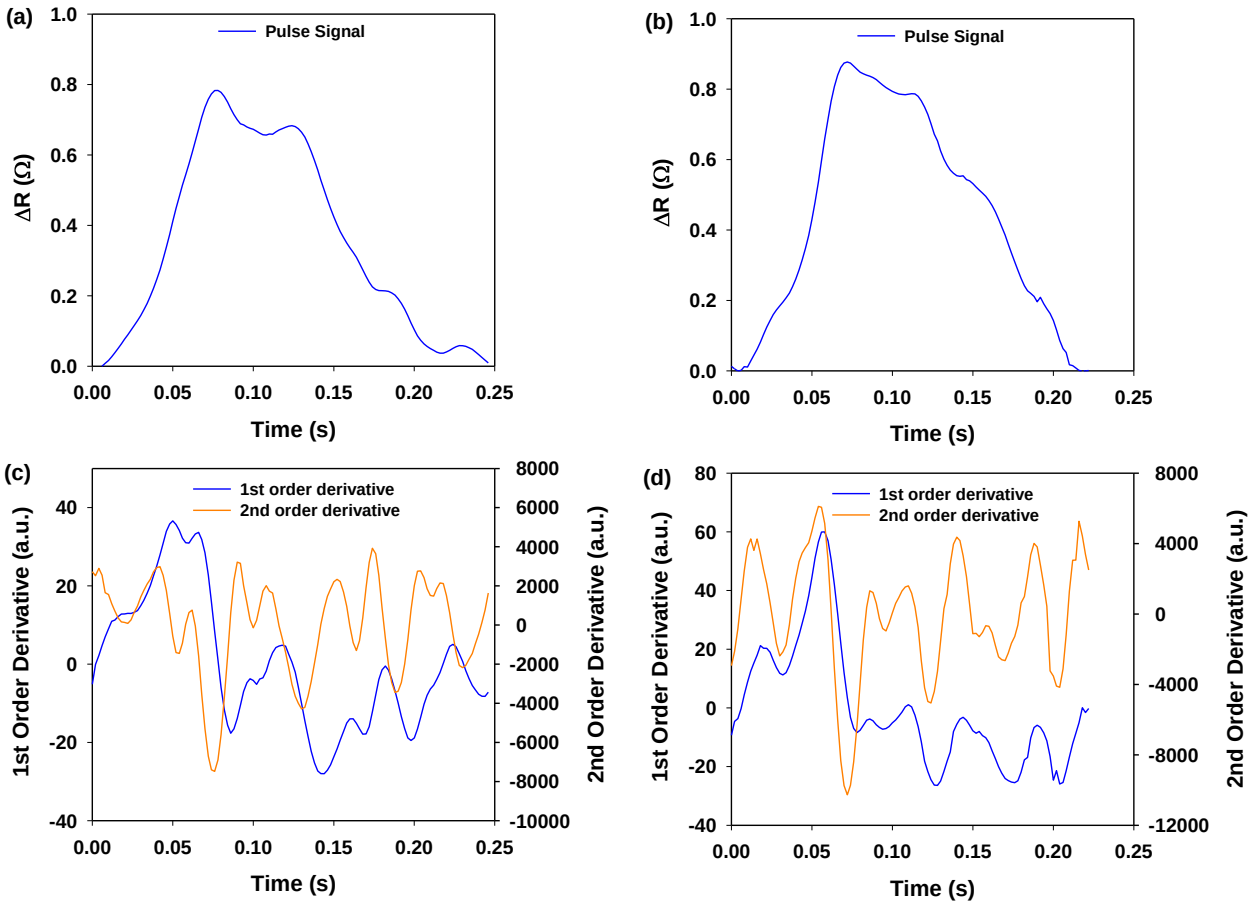


Figure 5.18 Demonstration of two pulse cycles with its first order and second order derivatives from rabbit before drug injection.

Table 5.6 Derived arterial wall parameter from two pulse cycles of the rabbit before and after 3 drug injections.

| | Elasticity | Viscosity | T | PWV | r0 | HR |
|---|---|---|---|---|---|---|
| Before Injection | 442.6<br>809.2 | 6.285<br>4.704 | 0.2459<br>0.2219 | 27.13<br>26.42 | 0.398<br>0.461 | 243.90<br>270.27 |
| Drug Injection 1 | 886.54<br>506.59 | 10.87<br>4.61 | 0.2520<br>0.2040 | 36.81<br>24.29 | 0.303<br>0.466 | 238.10<br>294.12 |
| Drug Injection 2 | 527.29<br>391.67 | 10.23<br>6.74 | 0.2603<br>0.2640 | 36.47<br>29.55 | 0.313<br>0.385 | 230.77<br>227.27 |
| Drug Injection 3 | 1034<br>590.08 | 13.2<br>9.45 | 0.258<br>0.290 | 44.94<br>39.25 | 0.275<br>0.325 | 232.56<br>206.90 |
| Post Injection | 573.90<br>563.71 | 8.06<br>9.073 | 0.264<br>0.254 | 32.70<br>32.96 | 0.352<br>0.332 | 227.27<br>236.22 |

### 5.3.3 Effect of Inter-subject Variation

Since the true pulse signal in an artery needs to be transmitted to the sensor through overlying tissue, its thickness significantly affects a measured pulse signal. As to subjects with different BMI (indicative of the overlying tissue thickness), the sensor design needs to be tailored to accommodate variations in overlying tissue thickness among subjects. For those who have a higher BMI, the measured signals are unclear and may be distorted in some cases. While, for those who have a lower BMI, the sensor may block the artery due to the thinner overlying tissue. Therefore, a trade-off between sensor sensitivity and BMI is encountered.

An experiment is conducted to examine the inter-subject variation on the measured results. 41yr-F subject (BMI: 19.9) and 54yr-F (BMI: 37.4) are recruited to participate in this study. The pulse signals were measured by varying the hold-down pressure toward the arterial region, the signals under maximum hold-down pressure are treated as the signals at zero transmural pressure. The sensor is initiated by contacting the skin, then increased with hold-down pressure approximate every 10 seconds at each strength level. After the maximum signals obtained, the sensor is then released at each hold-down strength until the sensor is detached.

The results from measured arterial pulse signals on two subjects with low/high BMI at RA are shown in Figure 5.19 and Figure 5.20. The results from the subject with low BMI indicate clear pulse signals with larger amplitude and increased indent depths, while the signals from the subject with high BMI indicates the smaller pulse amplitude and unclear indent depths. Under certain hold-down strength, the pulse signals are diminished from measured signals on 54yr-F subject. The overlying tissue between the skin and artery plays an important role in the pulse measurement. Therefore, an optimized sensor design to implement the sensor with different subjects and improve the sensor-artery interaction is highly needed.

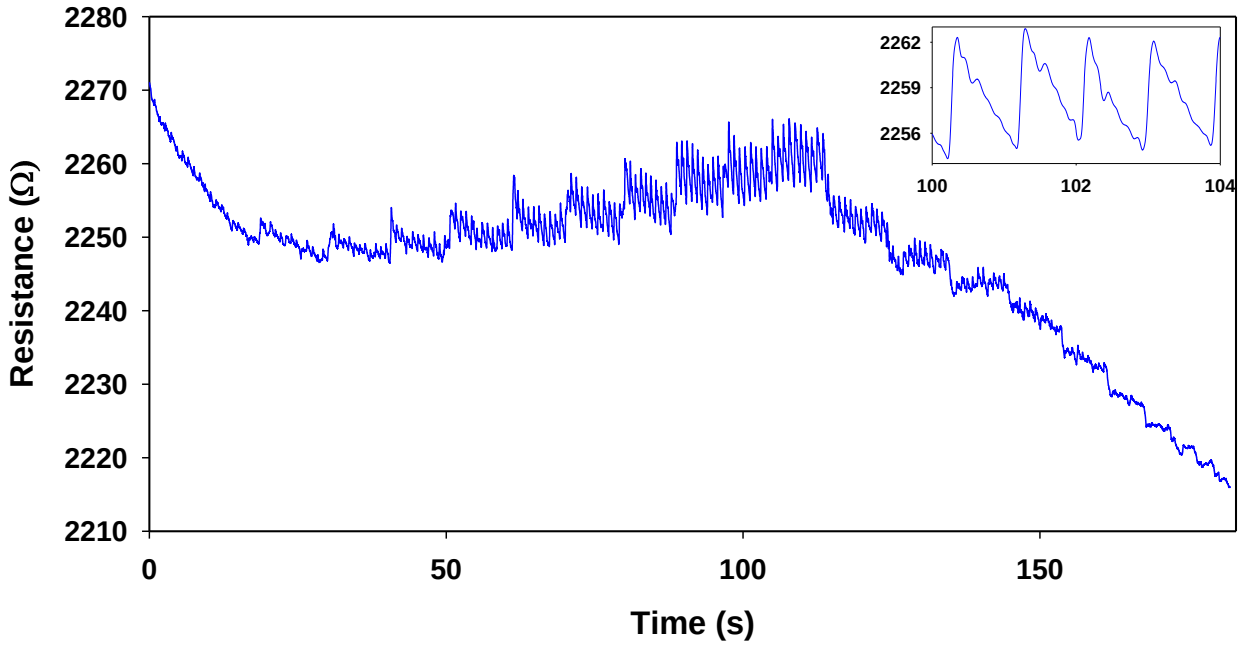


Figure 5.19 Absolute resistance of measure arterial pulse signals at RA under increased and decreased hold-down pressure from 41yr-F (BMI: 19.9).

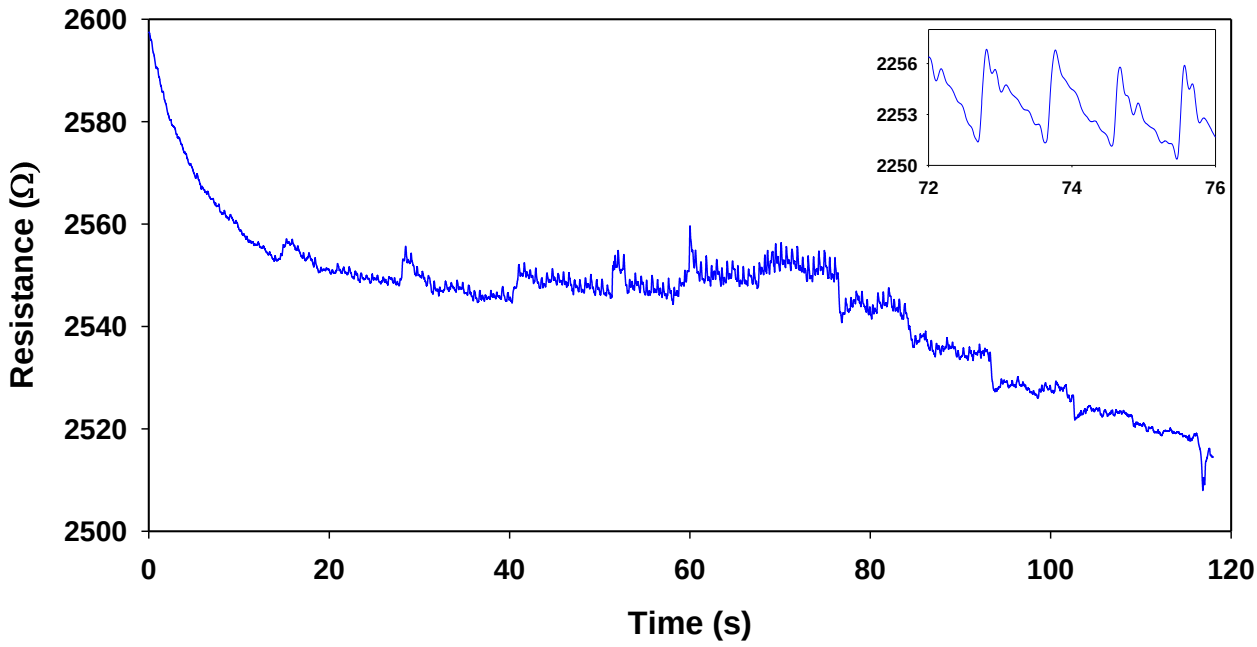


Figure 5.20 Absolute resistance of measured arterial pulse signals at RA under increased and decreased hold-down pressure from 54yr-F (BMI: 37.4).

## 5.4 Conclusion

The arterial wall parameters were extracted from the measured arterial pulse signals at rest on seven subjects at RA and STA. The absolute value of the parameters is unsuitable for comparison between subjects and arteries due to the subject-specificity and arterial-site-specificity. Changes in arterial wall parameters via moderate exercise was estimated from the measured pulse signals on five subjects. The arterial pulse signals were recorded before and after moderate exercise at 1min, 5mins, 10mins, 15mins, and 25mins from five subjects. The comparison between different subjects under the two conditions is carried out by t-test. The result from t-test indicates a significant change before and after moderate exercise. The estimated values reveal the difference between arteries and subjects, and thus validate the feasibility of estimating arterial wall parameters via model-based analysis. Hold-down pressure, sensor sensitivity and inter-subject variation are the three factors that may influence the measured results. Three experiments were conducted to analyze these factors separately. The experimental results indicate the sensor design needs to be optimized and the method for improving sensor-artery interaction need to be generated.

# CHAPTER 6

# OPTIMIZATION OF SENSOR DESIGN TO IMPROVE SENSOR-ARTERY INTERACTION AND ITS INFLUENCE OF ESTIMATING ARTERIAL WALL PARAMETERS

The performance of the sensor for arterial pulse measurement depends on several factors, such as hold-down pressure, the sensitivity of the sensor, and the inter-subject variation in overlying tissue. Arising from the sensor-artery interaction, a measured pulse signal is significantly affected by motion artifacts and overlying tissue above an artery. These two factors require optimizing the sensor design to obtain a clear measured pulse signal with minimum distortion for estimating arterial stiffness. Since the estimated arterial stiffness is subjected to inter-subject variations in overlying tissue thickness and sensor design, its adaptation to exercise is suggested to serve as a better assessment of cardiovascular health. This chapter is focused on optimizing the sensor design, improving the sensor-artery interaction and analyzing the influence on estimating arterial wall parameters on sensor design and subjects with high/low BMI.

## 6.1 Optimization of Sensor Design and Improvement of Sensor-artery Interaction

### 6.1.1 Optimization of Sensor Design

In a pulse signal measurement, the deformable microstructure is placed in contact with the skin surface above an artery. The sensor-artery interaction depends on sensor-design parameters (plunger geometry, and mechanism of optimal compression) and complex combination of interdependent factors including subject-specific parameters (wrist geometry, artery depth, skin thickness, the stiffness of arterial wall and surrounding tissue, and location of tendons) [97]. As mentioned in Section 5.3, a hold-down pressure on the sensor is needed to improve the coupling between the sensor and the artery so that the pulse signal in the artery can

be transmitted to the deformable microstructure and then recorded by the transducer. Motion artifacts (i.e., respiration and body shifting) causes fluctuations in hold-down pressure and thus affects the coupling. As such, a measured pulse signal results from the sensor-artery interaction involving the sensor design, overlying tissue above an artery, arterial wall, motion artifacts, and the true pulse signal in an artery. By measuring pulse signals with two different sensor designs, a sensor with high sensitivity was found to be very sensitive to motion artifacts and causes significant distortion in the measured pulse signal. In contrast, a sensor with relatively low sensitivity was more robust to motion artifacts. Since the true pulse signal in an artery needs to be transmitted to the sensor through overlying tissue, its thickness significantly affects a measured pulse signal. As to subjects with different BMI, the sensor design needs to be tailored to accommodate variations in overlying tissue thickness among subjects and the sensor-artery interaction needs to be improved.

According to the literature, flexible tactile sensors with [108] /without added structural features were invented to improve the conformal attachment of the sensor on skin surface [109]. These sensors are composed of multiple materials of varying strength and geometries, the interfacial stress among different materials experienced by these sensors during operation causes performance degradation and reduces long-term reliability of these sensors. Meanwhile, the extremely high sensitivity of a sensor may translate to a distorted pulse signal [110, 111], because the sensor is prone to operating beyond its linear range during pulse measurement. Furthermore, great conformity of a tactile sensor to the skin above an artery does not necessarily translate to a strong pulse signal, simply due to the complexity of tissue adjacent to an artery [97]. In contrast, conformal interaction between a tactile sensor and an artery is the key for obtaining a strong pulse signal.

A conformal interaction method is proposed to solve the above issue. A conformal layer is placed between the sensor and the arterial region to improve the sensor-artery interaction. Upon pressing the sensor against a conformal layer at an artery site with a hold-down pressure, the conformal layer can easily conform to the tissue adjacent to the artery so that the transmission of the pulse signal to the sensor is improved. Except for the PDMS microstructure, the rest of the sensor does not deform for conformity and thus translates to performance stability and long-term reliability.

The PDMS microstructure on the sensor is directly in contact with the skin; thus, the thickness and stiffness of the PDMS are critical to the performance of arterial pulse measurement. Uniform conformal layers of varying stiffness and damping were prepared by using PDMS materials of different mixing ratios (1:10, 1:20, and 1:30) of curing agent to the base (Sylgard ® 184 silicone elastomer kit, Dow Corning) and different thickness (1mm, 2mm, and 3.5mm). The pulse signal measured without the conformal layer is utilized as a reference for evaluating the influence of adding a conformal layer on a measured pulse signal.

The length of the sensor is tailored to 37mm for easy use, as shown in Figure 6.1. To further accommodate the sensor for subjects with high BMI, all the electrical contact pads are designed on the same side of the sensor for easily applying hold-down pressure and aligning the sensor on the artery region. According to Eq. (2.4), resistance, $R$, is reduced by an increased cross-sectional area. Thus, by increasing the width of each electrode from 200 μm to 400 μm, the output voltage is almost doubled. In the meantime, we assume the thickness and mechanical properties of the PDMS for the two sensors are identical. A conformal layer with 1:10 mixing ratio and $13\text{mm} \times 7\text{mm} \times 1\text{mm}$ in dimension is placed on top of the tactile sensor, which is presented in Figure 6.1 (b).

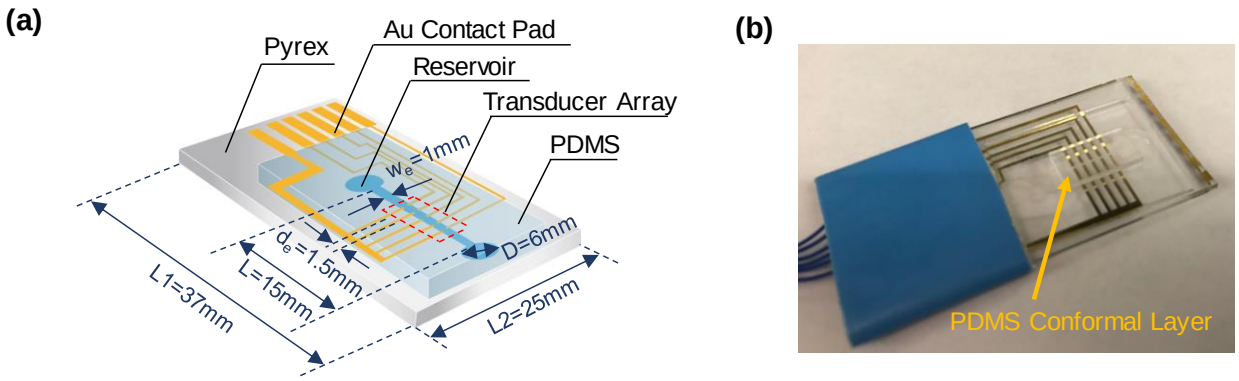


Figure 6.1 Schematic of an optimized microfluidic-based tactile sensor with labeled design parameters (a) and the picture of the sensor with PDMS conformal layer.

6.1.2 Performance Characterization of Optimized Sensor with Conformal Layers

The experimental setup for sensor characterization is the same as mentioned earlier in Section 2.2, except a conformal layer is added between the sensor and probe. A cylinder probe exerts displacement on top of a conformal layer for performance characterization. The performance characterization for the sensor without conformal layer served as a reference. The performance characterization of the sensor with a 3.5mm PDMS conformal layer is omitted due to the probe dimension being relatively small compared with the thickness of the conformal layer. The largest displacement is reached for each measurement hence the working range of the sensor with different designs are almost the same. The static performance characterization results for the optimized sensors with different conformal layers are shown in Figure 6.2. The results show good linearity of the sensor designs even under the largest displacement. Misalignment issues may be encountered in the experiment, which is the difficulty to achieve perfect normal contact of a probe with the sensor (non-ideal normal contact). The issue is also due to the alignment of the probe to the surface of the sensor with a non-contact point, which has a gap between them. This can be found in the 1$^{st}$, 2$^{nd}$, and 3$^{rd}$ transducers as they have a similar trend under probe displacement, but the outputs are not exactly the same. As shown in the Figure 6.2 (c)-(f), the

results from 1st and 5th transducers are lower than other transducers; this may be caused by the electrolyte flow from reservoirs to the sensing area, which may increase the sensing area at the 1st and 5th transducers, then decreased resistances are observed. Or it may be caused by a smaller length of the probe relative to the sensing region.

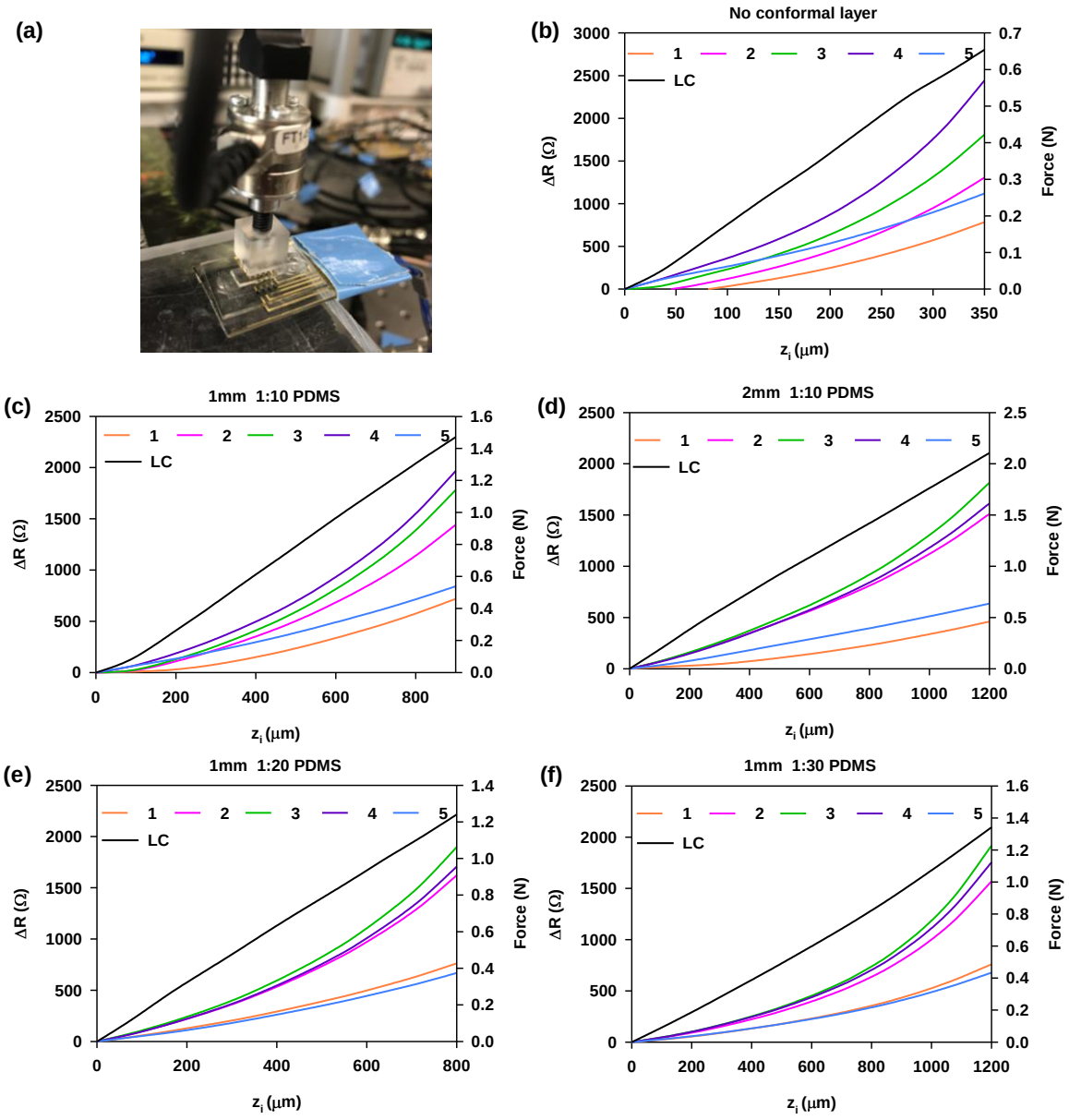


Figure 6.2 Sensor characterization setup (a) and the results under different conditions: without conformal layer (b), with 1mm (c), 2mm (d), 1:10 PDMS conformal layer, with 1mm 1:20 (e) and 1:30 (f) PDMS conformal layer, respectively.

The performance characterization of the optimized sensor with a conformal layer indicates its potential use in arterial pulse measurement. The schematic of pulse measurement using the sensor without a conformal layer and its equivalent mechanical model are illustrated in Figure 6.3, where the sensor is treated as a spring, $k_s$. Similar to an earthquake, the pulse signal in an artery which acts as an excitation source and excites an elastic wave propagating in the adjacent tissue. At the interface between the tissue and the sensor, part of the elastic wave transmits into the sensor and registers as the measured pulse signal by the sensor, while the rest reflected back into the adjacent tissue. As such, perfect conformal contact between the sensor and the skin surface does not translate to a strong pulse signal without a hold-down pressure for achieving conformal interaction between the artery and the sensor to improve the signal transmission.

The schematic of pulse measurement using the sensor with a conformal layer and its equivalent mechanical model is shown in Figure 6.4. While the sensor can be treated as a spring, $k_s$, the conformal layer needs to be treated as a spring $k_c$. The arterial wall can be treated as a spring $K$ with a damper $D$ due to its viscosity. Upon a hold-down pressure, their combined deformation will overpass the rigid tissue (Figure 6.4 c) and achieve a high conformal interaction between the sensor and the artery for improved signal transmission. Under the same hold-down pressure, a softer conformal layer yields a larger deformation to accommodate the rigid tissue and thus improves signal transmission, but in the meantime causes more attenuation to the transmitted pulse signal, since a softer conformal layer has higher damping. As compared with a soft conformal layer, a stiff conformal layer may not improve signal transmission very effectively but does not introduce much attenuation to the transmitted pulse signal.

Both the adjacent tissue and the hold-down pressure influence the transmission of a pulse signal to the sensor. The effect of the hold-down pressure on a measured pulse signal is twofold. On the one hand, a high hold-down pressure translates to a high conformal interaction between the sensor and the artery, thus leading to improved signal transmission. On the other hand, excessive hold-down pressure may occlude the blood flow and suppress the pulse signal. In other words, the excitation source, the pulse signal in the artery, can be changed by the hold-down pressure [112].

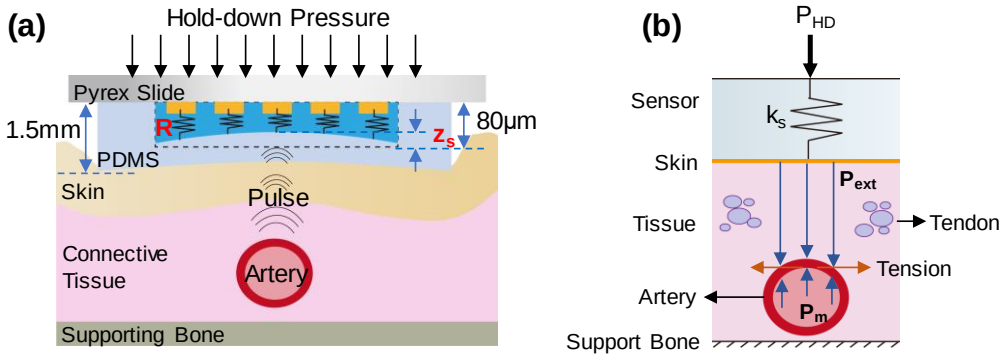


Figure 6.3 Arterial pulse signal measured using the distributed-deflection sensor with no conformal layer: (a) schematic; and (b) mechanical model. Note that the mechanical model is demonstrated for the artery deep under the skin.

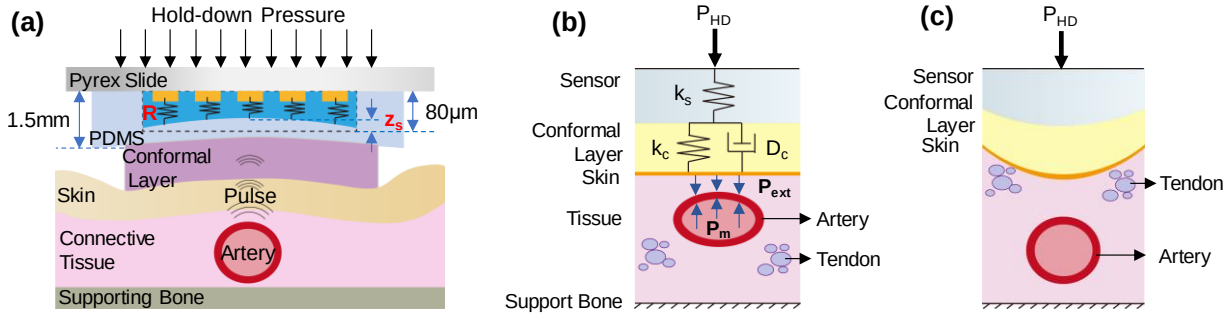


Figure 6.4 Arterial pulse signal measured using the distributed-deflection with a geometry-conformal layer: (a) schematic; (b) mechanical model; and (c) the conformal layer overpasses the rigid tissue. Note that the mechanical model is demonstrated for the artery close to the skin.

## 6.2 Performance of Optimized Sensor with Conformal Layers for Estimating Arterial Wall Parameters

The estimated arterial wall parameters are affected by both the sensor design and subject-specific parameters. To further investigate how the two factors influence the measured results, measured signals from normal-weight and obese subjects using a sensor with different PDMS conformal layers will be analyzed and compared.

### 6.2.1 Measurement Protocol

This study was approved by the IRB of Old Dominion University for arterial pulse measurement by adding a conformal layer to the current sensor. Consent forms are obtained from the six male subjects before any measurements. The pulse measurement is conducted in a quiet and temperature-controlled room. Subjects should remain still during pulse measurement. To measure a pulse signal, a uniform conformal layer is placed at the artery site and then the sensor is placed on top of the conformal layer. Afterward, two fingers are used to hold the sensor and maintain the stillness of the sensor. Such manual control of hold-down pressure is chosen for two reasons. First, this approach is of practical utility in real life, because the sensor can be easily held by the subject or a caregiver. Second, a control mechanism with a feedback loop on quantitatively controlling the hold-down pressure will contaminate the respiration information in the pulse signal by introducing another source of motion artifact. The same sensor is used for all the pulse measurements to eliminate the influence of the sensor on the measured results.

As shown in Figure 6.5, the arterial pulse signals were measured at RA and STA with two fingers holding the sensor. The two arterial sites are chosen for comparison because they have different overlying tissue between the skin and arterial wall, and they are located in the proximal and distal sites. The pulse measurements at RA and STA using the optimized sensor are

demonstrated in Figure 6.5 (b) and (c), respectively. Pulse signals were firstly measured from RA at rest via the sensor without the conformal layer by applying different hold-down strength for approximately 2mins. Then, a PDMS conformal layer is placed between the skin surface and the sensor.

The procedure for holding the sensor with different hold-down strength toward the arterial region is described in Figure 6.6. The sensor is initially placed on top of the skin by holding it with two fingers at RA. Then, the hold-down pressure is increased and kept for approximately 10 secs; after that, the strength is increased again. Until the pulse signals with the largest amplitude are identified, the hold-down pressure is then decreased until the original position is reached. This manually controlled pressure should be within the pain tolerance of subjects. As shown in Figure 6.6, the interaction region between the sensor and artery is demonstrated as a contact zone, where the obtained pulse signals are clear with noticeable indent depths.

In some cases, it may not exhibit a clear increase or decrease pressure in the subject with high BMI because of the thicker overlying tissue. Different conformal layers with different stiffness (1:10/1:20/1:30 mixing ratio) and thickness (1mm/2mm/3.5mm) will be applied to accommodate different subjects. The pulse signals measured on the subjects without conformal layers was used as a reference for comparison. Due to the thinner overlying tissue and its closeness to the skin surface at STA, the hold-down pressure is kept as the pulse signal with the largest amplitude, i.e. without increased or decreased pressure. The PDMS conformal layer with 1mm thickness, 1:10, 1:20 and 1:30 mixing ratio were used for arterial pulse measurement at STA on subjects at rest.

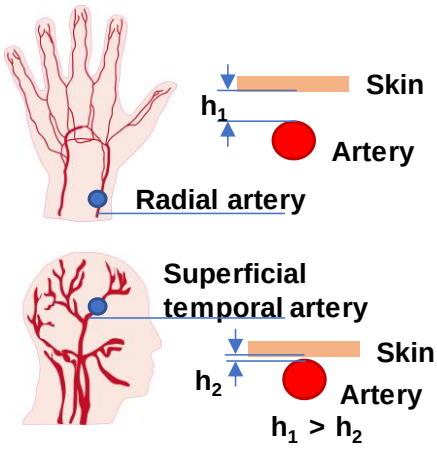


(a)

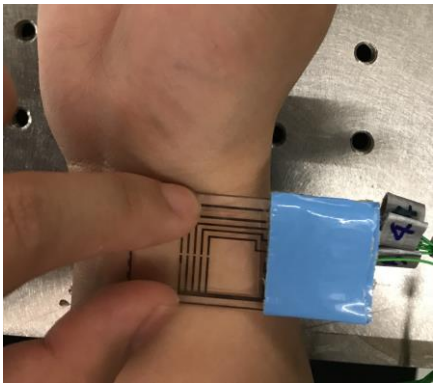

(b)

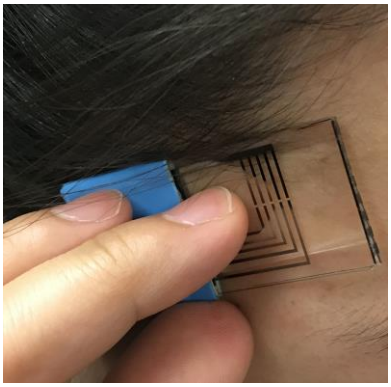

(c)

Figure 6.5 Measurement method for pulse signals: (a) arterial supply to the hand via the RA and to the head via STA; (b) pulse measurement at RA and (c) pulse measurement at STA.

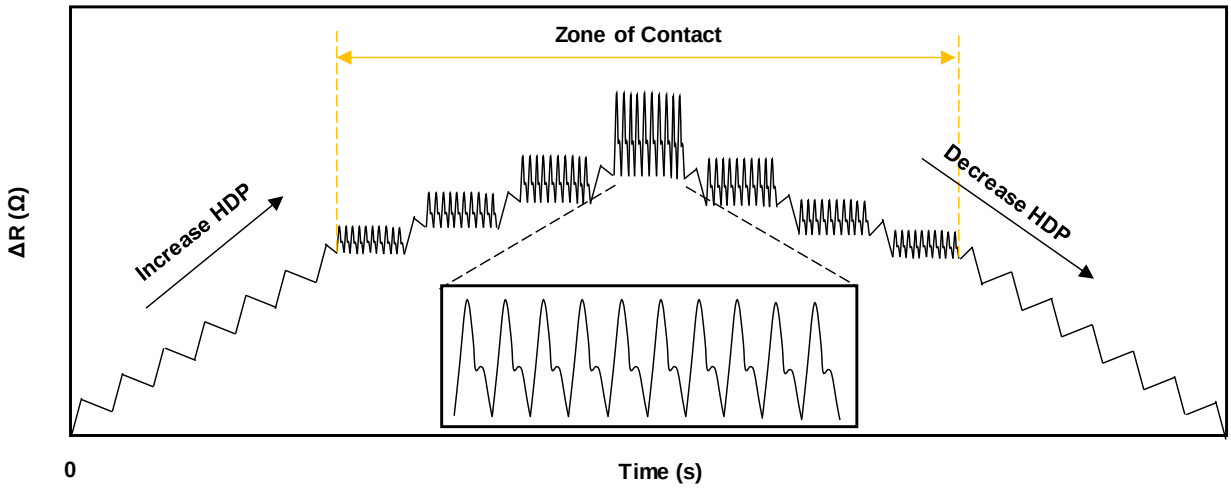


Figure 6.6 Demonstration of arterial pulse waveforms varied with hold-down pressure.

6.2.2 Results

The pulse signals are amplified obviously from the measured pulse signals on the 62yr-M subject and 24yr-M subject in Figure 6.7 and Figure 6.8, respectively. Without a conformal layer, signals were weakened because of the thicker overlying tissue in Figure 6.7, while the amplitude of the pulse signal is almost doubled with adding a conformal layer. Note that, the absolute resistance varies slightly while increasing or decreasing pressure in the measured result using the sensor without a conformal layer. Due to the thicker overlying tissue of the 62yr-M subject, the sensor-artery interaction is very weak. Obvious enhancement of this interaction is shown in the measurement results, especially the pulse signals measured via sensor with a 2mm, 1:10 PDMS conformal layer. But the signal is distorted as adding the layer with a 3.5mm thickness as the key features of the pulse signals are totally different from others.

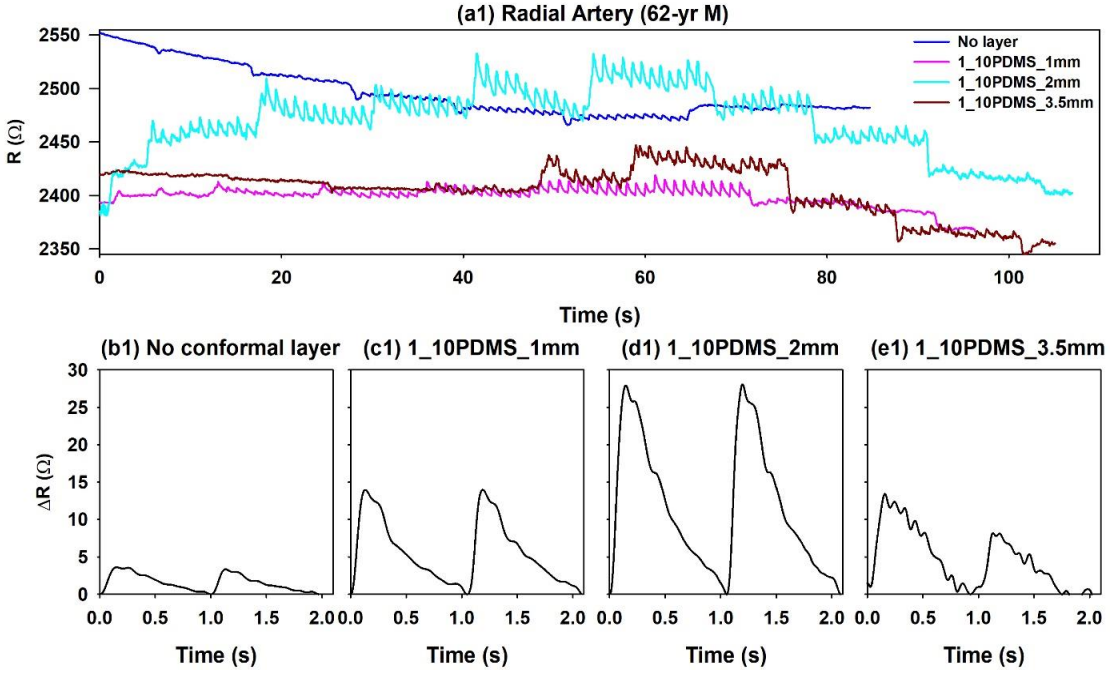

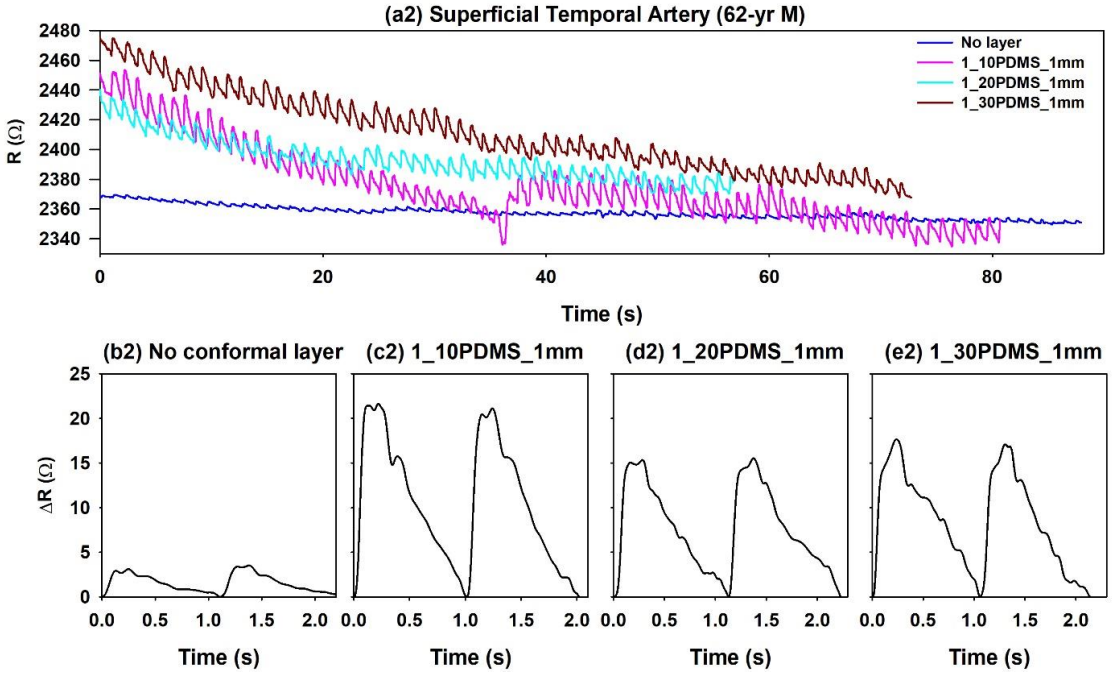


Figure 6.7 Measured pulse signals from 62yr-M at radial artery: (a1) measured pulse signals under different HDP; and (b1) - (e1) comparison of no conformal layer, 1: 10 PDMS with thickness 1mm, 2mm, and 3.5mm. Measured pulse signals from 62yr-M at superficial temporal artery: (a2) measured pulse signals under different HDP; and (b2)-(e2) comparison of no conformal layer, 1: 10, 1:20, 1:30 PDMS with 1mm thickness.

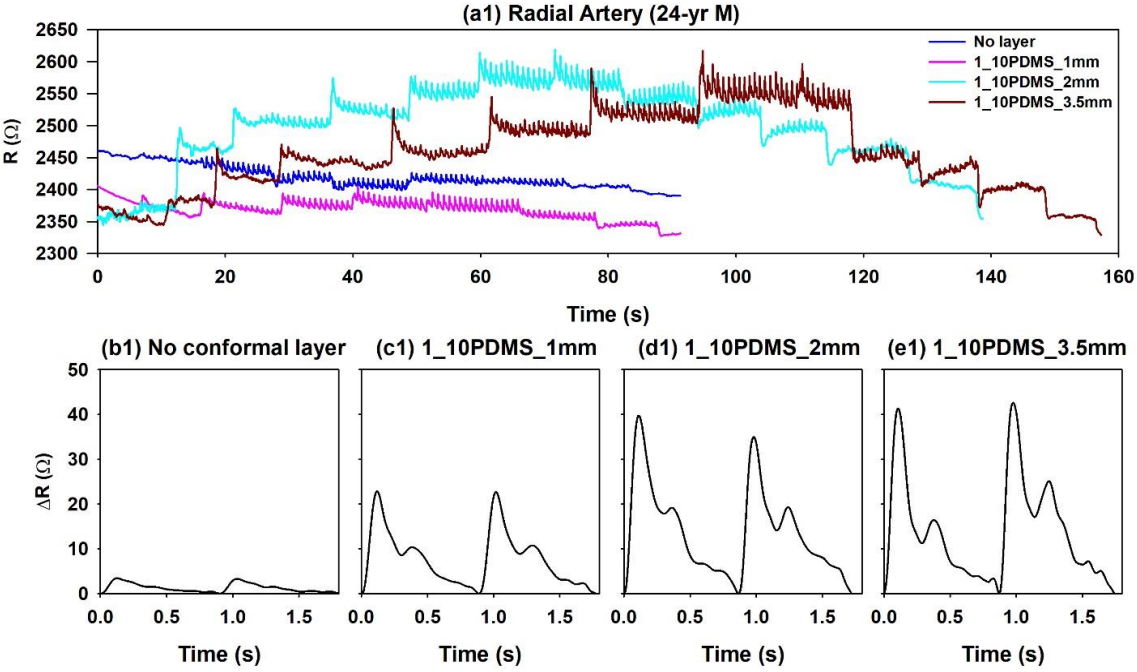

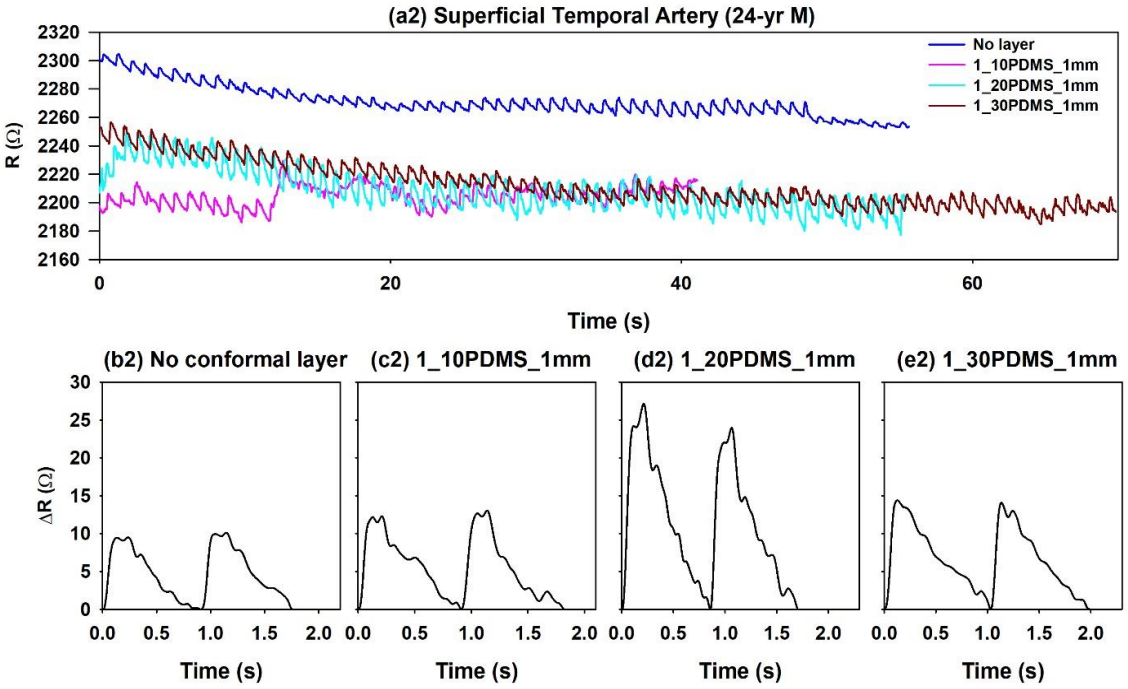


Figure 6.8 Measured pulse signals from 24yr-M at radial artery: (a1) measured pulse signals under different HDP; and (b1) - (e1) comparison of no conformal layer, 1: 10 PDMS with thickness 1mm, 2mm, and 3.5mm. Measured pulse signals from 24yr-M at superficial temporal artery: (a2) measured pulse signals under different HDP; and (b2)-(e2) comparison of no conformal layer, 1: 10, 1:20, 1:30 PDMS with 1mm thickness.

Though the pulse signal is clear enough from the measured signals on the 24yr-M subject with lower BMI, a significant amplified signal is seen as pressure increased. Overall, the conformal layer with 1mm or 2mm thickness works better on pulse acquisition than others for the two subjects at RA. The sensor with 1mm-thick, 1:10 or 1:20 PDMS conformal layer amplifies the arterial pulse signals measured from STA on the two subjects.

6.2.2.2 Variation on Thickness of Conformal Layer

The estimated arterial wall parameters using the optimized sensor with different conformal layers are shown in Table 6.1. The data for the 19yr-M subject without conformal layer and with 1mm-thick 1:10PDMS conformal layer is missing since the thicker overlying

tissue impedes the pulse signal acquisition. The data for 62yr-M, 31yr-M, and 25yr-M subjects with a 3.5mm-thick 1:10 PDMS conformal layer are missing because of the distorted pulse signals. The amplitude of the pulse signal, *Ur0*, is increased significantly after inserting the conformal layer for all subjects, especially for those with higher BMI. The measured HR varies little from the results using different sensors, which indicated the accuracy of the optimized sensor with a conformal layer.

Table 6.1 Values of parameters from six subjects at RA with varied thickness and 1:10 PDMS conformal layers under the largest HDP.

| Subject | Conformal Layer | PWV | $r_0$ | HR | Ur0 | D | K | $\eta_{\theta\theta}$ | $E_{\theta\theta}$ |
|---|---|---|---|---|---|---|---|---|---|
| 62yr-M BMI:30.5 | No layer | 10.024 | 0.6141 | 60 | 3.66 | 7.05 | 164.02 | 2.6543 | 61.755 |
| | 1mm PDMS | 9.9591 | 0.6569 | 57 | 11.86 | 5.55 | 154.51 | 2.3403 | 65.042 |
| | 2mm PDMS | 10.161 | 0.6363 | 58 | 28.27 | 6.14 | 162.93 | 2.4743 | 65.712 |
| 24yr-M BMI:20.4 | No layer | 11.29 | 0.5931 | 65 | 2.972 | 8.09 | 214.99 | 2.8433 | 75.643 |
| | 1mm PDMS | 12.099 | 0.5752 | 69 | 22.51 | 9.28 | 256.72 | 3.0369 | 84.102 |
| | 2mm PDMS | 11.8 | 0.6033 | 69 | 38.33 | 7.59 | 231.46 | 2.7524 | 83.985 |
| | 3.5mm PDMS | 12.078 | 0.6114 | 71 | 40.59 | 7.20 | 239.27 | 2.6794 | 89.175 |
| 31yr-M BMI:25.2 | No layer | 11.875 | 0.6029 | 66 | 18.04 | 7.61 | 234.13 | 2.7556 | 85.011 |
| | 1mm PDMS | 11.209 | 0.6139 | 59 | 16.46 | 7.28 | 207.92 | 2.6797 | 76.962 |
| | 2mm PDMS | 11.483 | 0.6313 | 62 | 23.09 | 6.38 | 210.98 | 2.5186 | 83.256 |
| 25yr-M BMI:29.2 | No layer | 12.683 | 0.5796 | 78 | 11.19 | 9.00 | 280.10 | 2.9912 | 93.117 |
| | 1mm PDMS | 11.889 | 0.6184 | 71 | 20.95 | 6.89 | 230.48 | 2.6205 | 87.475 |
| | 2mm PDMS | 12.561 | 0.5973 | 78 | 27.7 | 7.87 | 264.43 | 2.8047 | 94.326 |
| 19yr-M BMI: 36 | 2mm PDMS | 13.345 | 0.5559 | 91 | 29.42 | 10.6 | 322.70 | 3.246 | 98.99 |
| | 3.5 mm PDMS | 12.865 | 0.5359 | 87 | 16.25 | 12.3 | 311.71 | 3.495 | 88.786 |
| 28yr-M BMI:27.9 | No layer | 11.211 | 0.581 | 70 | 20.08 | 9.15 | 218.821 | 2.998 | 72.833 |
| | 1mm PDMS | 12.124 | 0.560 | 70 | 50.10 | 10.3 | 263.516 | 3.198 | 82.267 |
| | 2mm PDMS | 11.393 | 0.582 | 65 | 62.58 | 8.76 | 223.716 | 2.956 | 75.528 |
| | 3.5mm PDMS | 11.747 | 0.574 | 68 | 87.66 | 9.30 | 241.403 | 3.044 | 79.131 |

The relationship between BMI and arterial wall parameters from measured results via the sensor without a conformal layer, with 1mm-thick, 2mm-thick conformal layer are shown in Figure 6.9, Figure 6.10, and Figure 6.11, respectively. Because of the difficulty of obtaining the pulse signal on the subject with higher BMI, the data point in some figures is reduced to five.

The comparison of these linear regression equations should be conducted in the measured results from same subjects.

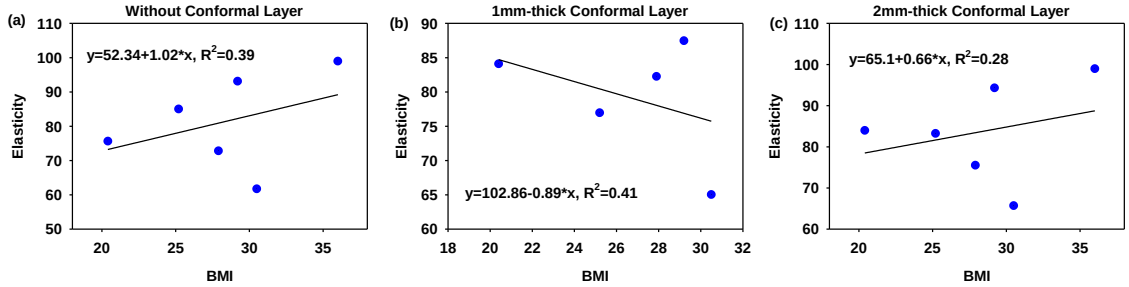


Figure 6.9 The relationship between BMI and elasticity from the optimized sensor with different conformal layer.

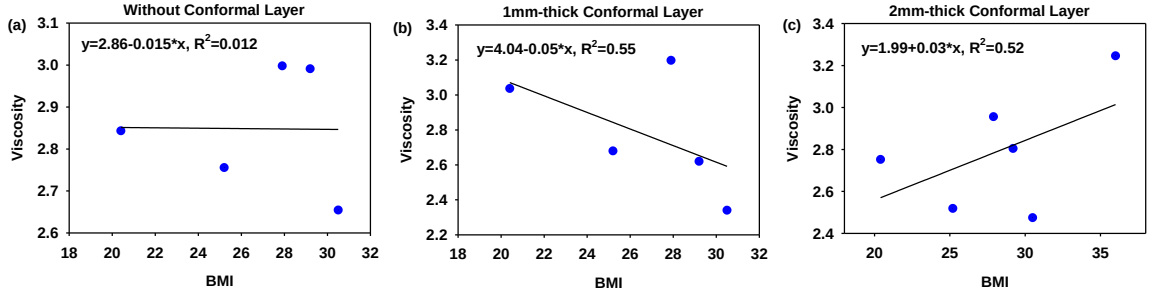


Figure 6.10 The relationship between BMI and viscosity from the optimized sensor with different conformal layer.

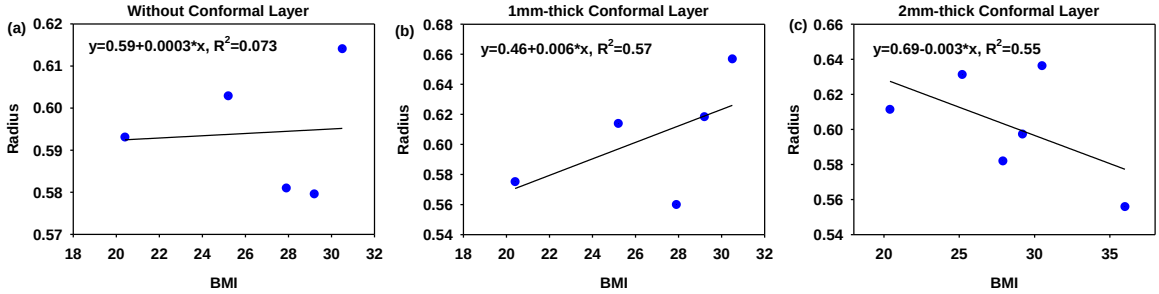


Figure 6.11 The relationship between BMI and radius from the optimized sensor with the different conformal layer.

As shown in Figure 6.9 (a) and (c), the linear trend changes slightly by adding a 2mm-thick conformal layer in the measurement. But the trend for viscosity and radius varies largely from the measured results, which can be observed in Figure 6.10 (a)-(b) and Figure 6.11 (a)-(b). Though these changes are obvious, the $R^2$ indicates a weak correlation between the two

parameters. The results reveal that the estimated arterial wall parameters vary slightly after adding a conformal layer to the optimized sensor for arterial pulse measurement.

6.2.2.3 Variation on Stiffness of Conformal Layer

The estimated arterial wall parameters from the measured signals on six subjects at STA are shown in Table 6.2. Due to the difficulty of the capturing pulse signals on the 31yr-M subject via the sensor with a 1mm-thick 1:10 PDMS layer and 19yr-M subject via the sensor without conformal, those data are missing in the table.

The value of elasticity increases in the rest of the four subjects from the measured signals via the sensor without conformal layer to the measured signals with a 1:10 PDMS conformal layer. The opposite trend is shown in the data collected on 31yr-M and 19yr-M subjects. The estimated value of HR varies little from measured results via the optimized sensor designs, except the 19yr-M subject who has the highest BMI. The pulse amplitude at STA is significantly enhanced after adding the conformal layer, especially for the 19yr-M subject.

The relationship of BMI and arterial wall parameters estimated from the measured arterial pulse signals at STA using the sensor with different conformal layer are shown in Figure 6.12, Figure 6.13, and Figure 6.14, respectively. The estimated elasticity is slightly affected by the mixing ratio of the conformal layer, as shown in Figure 6.12 (a)(c)(d). But the estimated viscosity and radius from measured signals on six subjects vary insignificantly while adding a conformal layer in the optimized sensor. Though the conclusion cannot be made on the effect of adding a conformal layer to the new sensor design, the pulse signals are amplified significantly, especially in those who have a higher BMI. This indicates the effectiveness of the method for improving sensor-artery interaction during arterial pulse measurement.

Table 6.2 Values of parameters from six subjects at STA with varied stiffness of 1mm-thick conformal layers under the largest HDP.

| Subject | Conformal Layer | PWV | $r_0$ | HR | Ur0 | D | K | $\eta_{\theta\theta}$ | $E_{\theta\theta}$ |
|---|---|---|---|---|---|---|---|---|---|
| 62yr-M BMI:30.5 | No layer | 9.0935 | 0.675 | 54 | 3.078 | 5.03 | 126.28 | 2.2246 | 55.685 |
| | 1:10 PDMS | 10.361 | 0.6738 | 58 | 20.07 | 4.87 | 159.83 | 2.2052 | 72.352 |
| | 1:20 PDMS | 10.046 | 0.6766 | 55 | 14.69 | 4.79 | 149.56 | 2.1871 | 68.358 |
| | 1:30 PDMS | 9.3902 | 0.6937 | 53 | 15.35 | 4.35 | 127.68 | 2.0822 | 61.206 |
| 24yr-M BMI:20.4 | No layer | 10.449 | 0.6606 | 63 | 8.875 | 5.35 | 168.77 | 2.3041 | 72.355 |
| | 1:10 PDMS | 11.623 | 0.6107 | 67 | 12.79 | 8.73 | 242.36 | 2.8293 | 81.75 |
| | 1:20 PDMS | 11.68 | 0.6137 | 70 | 23.79 | 7.12 | 223.54 | 2.6636 | 83.746 |
| | 1:30 PDMS | 12.034 | 0.6214 | 65 | 12.81 | 6.72 | 233.15 | 2.5909 | 89.989 |
| 31yr-M BMI:25.2 | No layer | 11.338 | 0.5935 | 61 | 2.755 | 8.11 | 217.62 | 2.8439 | 76.349 |
| | 1:20 PDMS | 10.239 | 0.6355 | 59 | 9.919 | 6.21 | 166.58 | 2.4856 | 66.609 |
| | 1:30 PDMS | 11.451 | 0.6431 | 63 | 14.33 | 5.90 | 205.23 | 2.4249 | 84.286 |
| 25yr-M BMI:29.2 | No layer | 10.893 | 0.6099 | 70 | 4.631 | 7.37 | 195.57 | 2.7042 | 72.297 |
| | 1:10 PDMS | 12.566 | 0.6005 | 72 | 10.77 | 7.79 | 264.24 | 2.7837 | 94.8 |
| | 1:20 PDMS | 12.613 | 0.6026 | 74 | 9.079 | 7.66 | 265.62 | 2.762 | 95.819 |
| | 1:30 PDMS | 12.728 | 0.6222 | 71 | 11.38 | 6.67 | 261.15 | 2.5832 | 101.05 |
| 19yr-M BMI: 36 | 1:10PDMS | 12.708 | 0.571 | 92 | 15.43 | 9.61 | 288.36 | 3.087 | 92.360 |
| | 1:20PDMS | 12.311 | 0.598 | 83 | 13.87 | 7.86 | 254.86 | 2.800 | 90.750 |
| | 1:30 PDMS | 11.665 | 0.604 | 81 | 16.53 | 8.09 | 232.41 | 2.797 | 81.759 |
| 28yr-M BMI:27.9 | No layer | 10.636 | 0.623 | 63 | 10.58 | 6.81 | 184.40 | 2.60 | 70.40 |
| | 1:10PDMS | 11.138 | 0.655 | 60 | 18.02 | 5.45 | 189.58 | 2.33 | 81.28 |
| | 1:20PDMS | 12.432 | 0.636 | 71 | 16.57 | 6.15 | 243.80 | 2.48 | 98.24 |
| | 1:30PDMS | 10.849 | 0.602 | 67 | 14.14 | 7.68 | 196.56 | 2.77 | 70.82 |

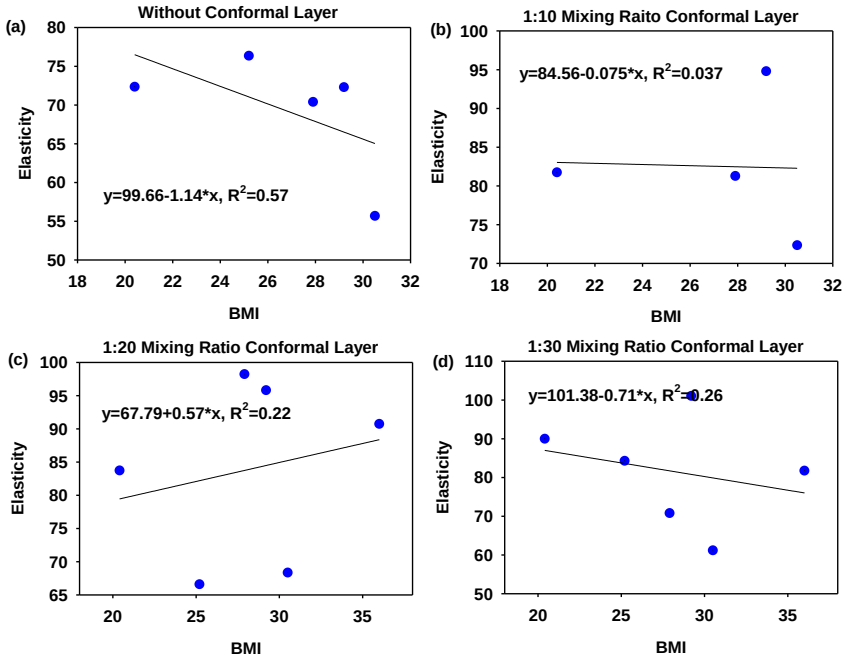


Figure 6.12 Relationship of BMI and elasticity from the measured signals at STA using optimized sensor adding a conformal layer with 1mm-thick and different mixing ratio.

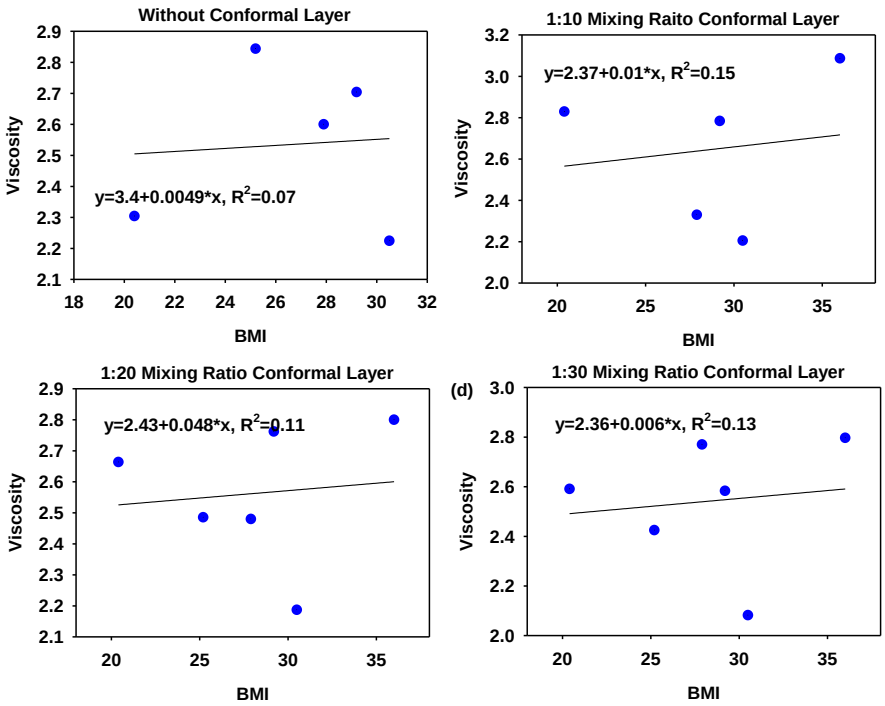


Figure 6.13 Relationship of BMI and viscosity from the measured signals at STA using optimized sensor adding a conformal layer with 1mm-thick and different mixing ratio.

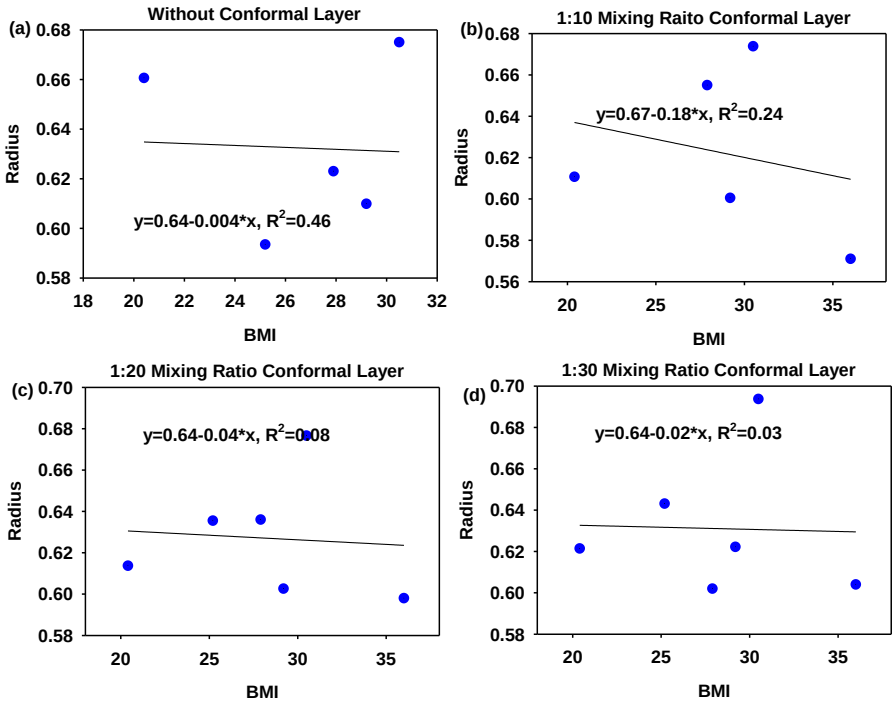


Figure 6.14 Relationship of BMI and radius from the measured signals at STA using optimized sensor adding a conformal layer with 1mm-thick and different mixing ratio.

6.2.2.4 Variation of Respiration Waveform on Sensor with Different Conformal Layers

Owing to the respiration of a subject and the hand jittering during a measurement, motion artifacts in a pulse measurement are unavoidable. Sometimes, it is desirable to assess the arterial pulse waveform difference between at-rest and post-exercise. The absolute resistance signals of the five transducers from a subject post-exercise measured are shown in Figure 6.15. The $4^{th}$ and $5^{th}$ transducers capture not only a clear patterned pulse signal, but also a heavily-breathing pattern, indicating that these two transducers at the site of the carotid artery. The breathing pattern introduces an extremely large baseline drift to the recorded pulse signal. However, the sensor is capable of obtaining the undistorted pulse waveform under such severe motion artifacts. The rest of the three transducers obtain random signals with the heavily-breathing pattern, indicating that these transducers are away from the carotid artery. Owing to fabrication variation, the original resistance varies among the five transducers. As such, this measurement indicates that the transducers do not interfere with each other in a pulse measurement.

The hold-down pressure fluctuates in accord with respiratory-related motion artifacts and non-respiratory-related motion artifacts. The complex relations among respirations, motion artifacts, hold-down pressure, and a measured pulse signal is illustrated in Figure 6.16. The pulse signal in an artery arises from the heartbeat. Owing to the Autonomic Nervous System (ANS) [113], respirations modulate the pulse signal and thus is embedded in the pulse signal. Meanwhile, respirations give rise to body motion, referred to as respiratory-related body motion. A subject also experiences non-respiratory-related body motion (e.g., the slight shifting of body parts) and the two fingers holding the sensor also move slightly, which is non-respiratory-related. Therefore, three sources of motion artifacts influence the hold-down pressure and to what extent each source influences the hold-down pressure is unpredictable. Note that the adjacent tissue and

the holding strength of the fingers determine the hold-down pressure magnitude. Furthermore, the hold-down pressure interacts with the pulse signal in an artery. As such, the measured pulse signal is less contaminated by non-respiratory motion artifacts than the time-varying hold-down pressure, and thus is used for deriving the respiratory waveform.

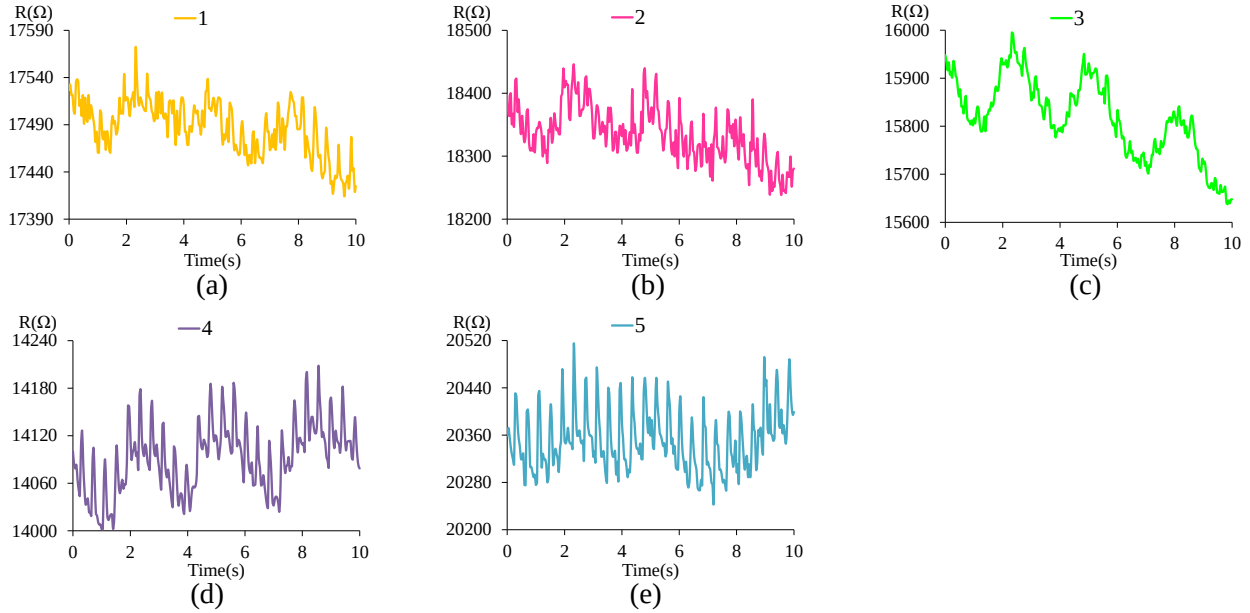


Figure 6.15 Absolute resistance signals of the five transducers recorded from carotid pulse signals post-exercise.

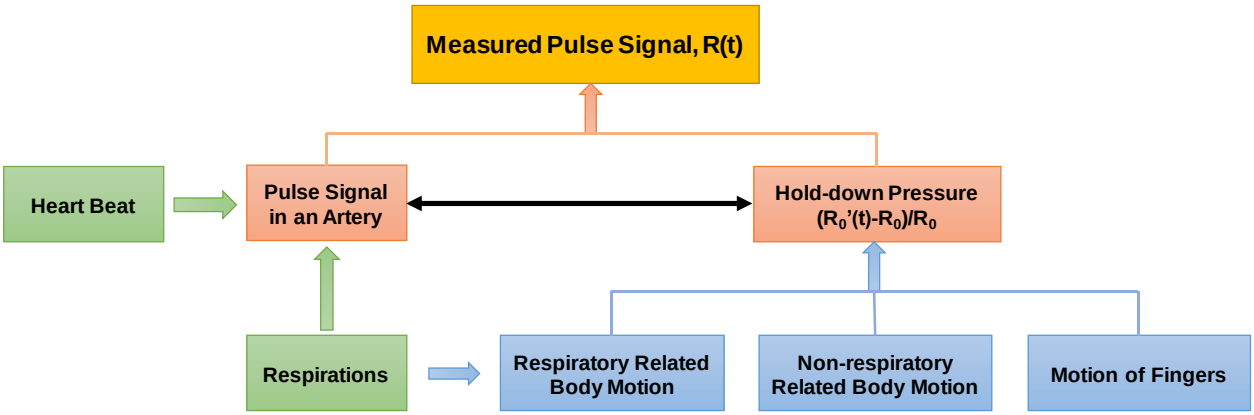


Figure 6.16 Complex relations among respirations, motion artifacts, hold-down pressure and a measured pulse signal.

To analyze the respiration waveform, the signals are extracted from arterial pulse signals. The frequency range of respiration signal is 0.2-0.4Hz. Empirical Mode Decomposition (EMD) is commonly used for extracting respiration waveforms. EMD decomposes a nonstationary and nonlinear signal into a sum of components called the Intrinsic Mode Function (IMF) and a final residual, through repeating the basic sifting process. The algorithm of EMD for a signal *R(t)* can be summarized as follows [114]: identify the local maxima and minima of *R(t)*; generate the upper envelope, *U(t)*, and lower envelop, *L(t)*; calculate the local mean *m(t) = (U(t)+ L(t))/2*; extract the detail signal *d(t)=R(t)-m(t)*, until it meets a stopping criterion and becomes $IMF_i$: $R(t)-IMF_i=m_i(t)$; and iterate the residual $m_i(t)$ for the sifting process. IMFs and a final residual are presented as:

$$R(t)=\sum_{i=1}^{n} IMF_i(t)+m_n(t) R(t)=\sum_{i=1}^{n} IMF_i(t)+m_n(t) \tag{6.1}$$

where $IMF_i(t)$ are the IMFs and $m_n(t)$ is a final residual. The IMF of the pulse signal within the frequency range of 0.2-0.4Hz was selected as the respiration waveform.

Ensembled Empirical Mode Decomposition (EEMD) method [115], a popular noise-assisted data analysis method for non-linear and non-stationary signal, is utilized to derive the respiration signals from the pulse signals. This method solves the problem of mode mixing in Empirical Mode Decomposition (EMD) through the help of adding white noise, resulting in a more precise extraction of the respiration signal. To investigate the effect of sensor design on respiration waveform, EEMD method is utilized to extract the waveform from 28yr-M at RA and STA before exercise. The signals are extracted from the same sensor with varies thickness and the sensor with varies stiffness under the same thickness.

The respiration waveforms derived from pulse signals measured at RA and STA are shown in Figure 6.17. The amplitude of each respiration waveform varies with time, due to non-respiratory motion artifacts. The pulse signals at the RA via the sensor without conformal layer generate much stronger respiration waveforms than the rest. The pulse signals measured at STA via the sensor a 1:10 PDMS conformal layer registers the strongest respiration waveform, which is followed by the one from the pulse signal measured with a 1:20 PDMS conformal layer. The correlation of the respiration waveform strength with the pulse amplitude might result from high conformal interaction, which alleviates the influence of non-respiratory motion artifacts on a measured pulse signal and thus translates to a stronger respiration signal.

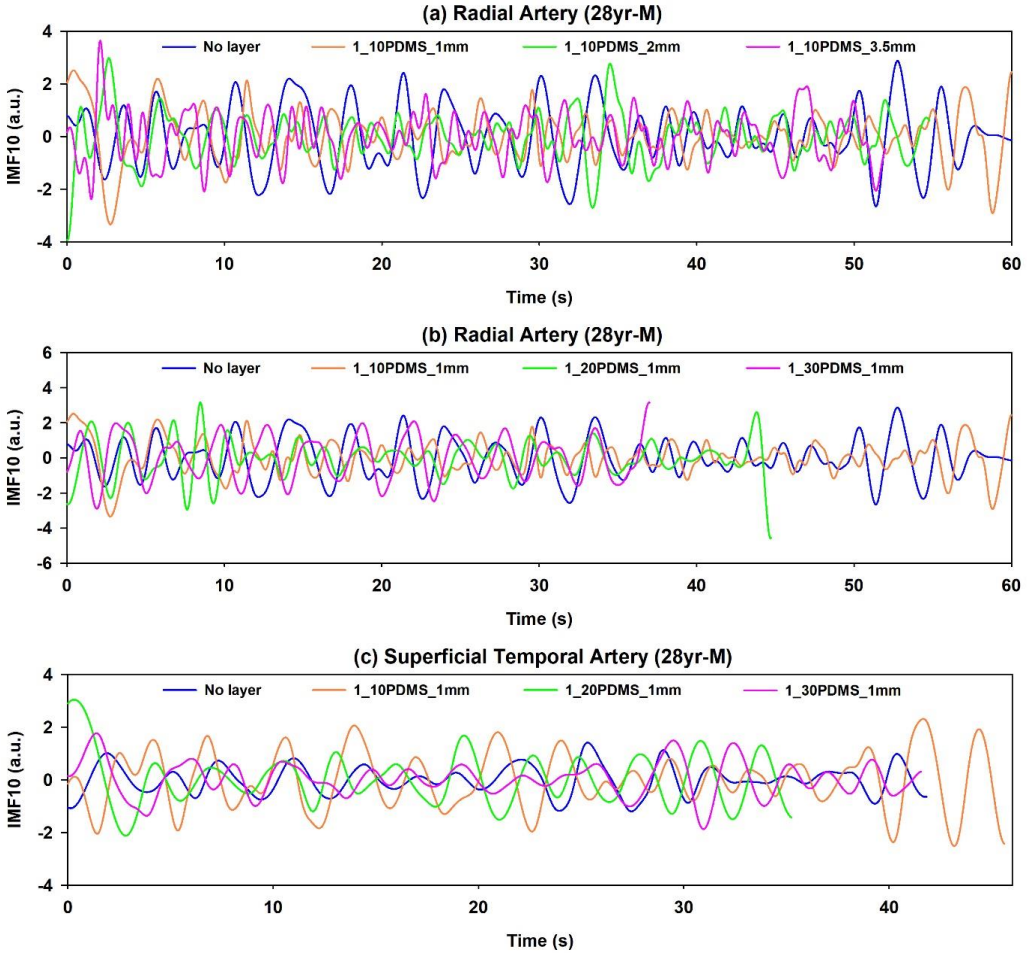


Figure 6.17 Respiration signals derived from the measured pulse signals at RA (a)(b) and the STA (c) on the 28yr-M subject.

## 6.3 Performance of Optimized Sensor for Tracking Changes in Arterial Wall Parameters

Subject-specific parameters, such as overlying tissue between skin and artery, is a primary factor that may affect the estimation of arterial wall parameters. Subjects with normal-weight and over-weight are chosen for investigating the influence of estimated parameters. Obese individuals have a higher prevalence of hypertension than those who have normal weight. Indeed, obese individuals have higher central BP and stiffer central arteries compared with normal-weight counterparts [116]. Moderate or acute maximal exercise can induce substantial changes and may reveal potential vascular abnormalities, which may not cover at rest. Thus, understanding how obesity influences the arterial wall parameter estimation of great importance.

### 6.3.1 Measurement Protocol

The pulse signals are captured from 19yr-M (BMI: 36) and 28yr-M (BMI: 27.9). A polymer conformal layer may insert between the sensor and skin for signal amplification. In the meantime, a medical instrument (fully automatic upper arm blood pressure monitor, Paramed monitor) is placed on the arm to measure blood pressure and HR. The sensor and the blood pressure cuff will be worn at the same time. The two subjects are required to do 2-5min moderate exercise. The pulse signals are measured at rest and at different times during the first 25 minutes post-exercise.

### 6.3.2 Results

#### 6.3.2.1 Arterial Wall Parameters Estimated on Subjects with Different BMI

By analyzing the data collected from the sensor with different conformal layers before moderate exercise, the 2mm-thick 1:10PDMS conformal layer was chosen for arterial pulse measurement on the 19yr-M subject. While a 1mm-thick 1:10 PDMS conformal layer was chosen for the 28yr-M subject at RA since they provide largest output. The sensor with a 1mm-

thick 1:10 PDMS conformal layer was used to measure the pulse signals at STA on the two subjects. The estimated arterial wall parameters from the measured results using a sensor with conformal layers are shown in Table 6.3. Arterial wall parameters change largely at post-exercise 1min; then they fluctuate slightly. Finally, the parameters tend to recover to the original state. The HR is slowly recovered after 25min of the exercise and fluctuated between post 10min and post 25min at RA and STA. The measured results indicate the effectiveness of the optimized sensor with conformal layers for tracking the changes in arterial wall parameters.

Table 6.3 Comparison of parameters before and post exercise for 19yr-M and 28yr-M subjects.

| Subject | Artery | Physical Status | PWV | $r_0$ | HR | Ur0 | D | K | $\eta_{\theta\theta}$ | $E_{\theta\theta}$ |
|---|---|---|---|---|---|---|---|---|---|---|
| 19yr-M | RA | Post 1min | 16.483 | 0.458 | 118 | 45.29 | 23.00 | 599.18 | 4.78 | 124.59 |
| | | Post 5min | 13.281 | 0.533 | 104 | 32.22 | 12.66 | 334.47 | 3.54 | 93.83 |
| | | Post 10min | 13.026 | 0.539 | 92 | 27.31 | 12.39 | 321.61 | 3.49 | 91.03 |
| | | Post 15min | 15.347 | 0.485 | 99 | 22.18 | 18.60 | 491.15 | 4.29 | 113.94 |
| | | Post 25min | 13.581 | 0.541 | 96 | 17.92 | 11.87 | 343.86 | 3.44 | 99.61 |
| | STA | Post 1min | 17.573 | 0.547 | 118 | 15.99 | 11.17 | 565.94 | 3.34 | 169.07 |
| | | Post 5min | 14.827 | 0.558 | 103 | 8.90 | 10.46 | 399.57 | 3.22 | 122.96 |
| | | Post 10min | 12.417 | 0.530 | 95 | 6.01 | 12.96 | 294.64 | 3.58 | 81.61 |
| | | Post 15min | 15.412 | 0.514 | 101 | 18.85 | 15.03 | 468.08 | 3.84 | 122.49 |
| | | Post 25min | 13.407 | 0.568 | 95 | 11.89 | 9.70 | 320.24 | 3.11 | 102.86 |
| 28yr-M | RA | Post 1min | 16.324 | 0.520 | 123 | 90.57 | 13.72 | 512.77 | 3.70 | 138.50 |
| | | Post 5min | 13.265 | 0.528 | 102 | 58.43 | 12.89 | 333.76 | 3.59 | 92.93 |
| | | Post 10min | 13.174 | 0.529 | 99 | 59.27 | 12.84 | 329.28 | 3.58 | 91.80 |
| | | Post 15min | 12.721 | 0.557 | 94 | 51.88 | 10.59 | 294.00 | 3.24 | 90.00 |
| | | Post 25min | 13.483 | 0.535 | 103 | 40.13 | 12.56 | 345.61 | 3.52 | 97.10 |
| | STA | Post 1min | 14.942 | 0.485 | 122 | 11.33 | 18.07 | 460.97 | 4.25 | 108.38 |
| | | Post 5min | 12.832 | 0.542 | 103 | 13.00 | 11.74 | 305.51 | 3.42 | 89.13 |
| | | Post 10min | 14.269 | 0.558 | 97 | 18.13 | 10.34 | 364.86 | 3.21 | 113.68 |
| | | Post 15min | 13.210 | 0.577 | 93 | 9.53 | 9.22 | 304.57 | 3.02 | 100.52 |
| | | Post 25min | 13.406 | 0.563 | 91 | 12.37 | 10.06 | 322.41 | 3.16 | 101.40 |

6.3.2.2 Comparison of Measured Results with Medical Instruments

The medical instrument is used to measure the blood pressure and heart rate before exercise and post exercise at the different time period. The systolic pressure (SP), diastolic

pressure (DP) and HR measured from the two subjects are shown in Table 6.4. The estimate HR in Table 6.3 and Table 6.4 indicates a good consistency of the results from the current sensor with the medical instrument. Though measurement error might occur during the pulse measurement, the optimized sensor with a conformal layer captures the main trend during this procedure, and the measured results vary little compared with measured results from a medical instrument. An increased SP is observed in the two subjects right after exercise. The parameters fluctuate between the data measured at post-exercise 15min and 25min, which is also found in the estimated parameters measured using our sensor. The DP is decreased right after exercise on the 19yr-M subject, while, it is increased on the 28yr-M subject. This may be caused by the measurement error, which occurs in wrapping the pressure cuff on the arm with thick overlying tissue on the 19yr-M subject.

Table 6.4 Comparison of parameters after moderate exercise for 19yr-M and 28yr-M subjects.

| | | At rest | Post 1min | Post 5min | Post 10min | Post 15min | Post 25min |
|---|---|---|---|---|---|---|---|
| 19yr-M | SP | 140 | 154 | 127 | 127 | 136 | 125 |
| | DP | 96.5 | 81 | 66 | 70 | 70 | 74 |
| | HR | 82.5 | 120 | 105 | 96 | 95 | 94 |
| 28yr-M | SP | 102 | 181 | 132 | 127 | 119 | 114 |
| | DP | 70 | 84 | 77 | 76 | 78 | 68 |
| | HR | 62 | 125 | 102 | 97 | 95 | 93 |

The estimated arterial wall parameters and measured results from the medical instruments on the 19yr-M subject are plotted in the same graph for comparison, which is shown in Figure 6.18. The ΔP is calculated as the difference between SP and DP. The change in measured SP and ΔP has a similar trend in the changes in the estimated elasticity from at-rest to post 25min, which are shown in Figure 6.18 (a). The trend for the measured HR and the estimated HR are similar, which indicate the good accuracy of the current sensor compared with the medical instrument. The trend for the estimated wall radius is opposite to viscosity at two locations. Note that, the

elasticity varies largely from the results measured at STA in Figure 6.18 (c). This may be caused by heavy breath induced head movement in the recovering process after the moderate exercise.

The estimated arterial wall parameters and measured results on the 28yr-M subject from the medical instruments are plotted in Figure 6.19. The estimated elasticity and HR vary slightly compared with the measured results using a medical instrument. The opposite trend is found in the estimated viscosity and radius using current sensor in Figure 6.19 (b) and (d). The two sensors were held by different investigators, the results may be affected by the hold-down pressure. But, the changes in arterial wall parameters still captured by the current sensor and the measured results are consistent with the results from a medical instrument.

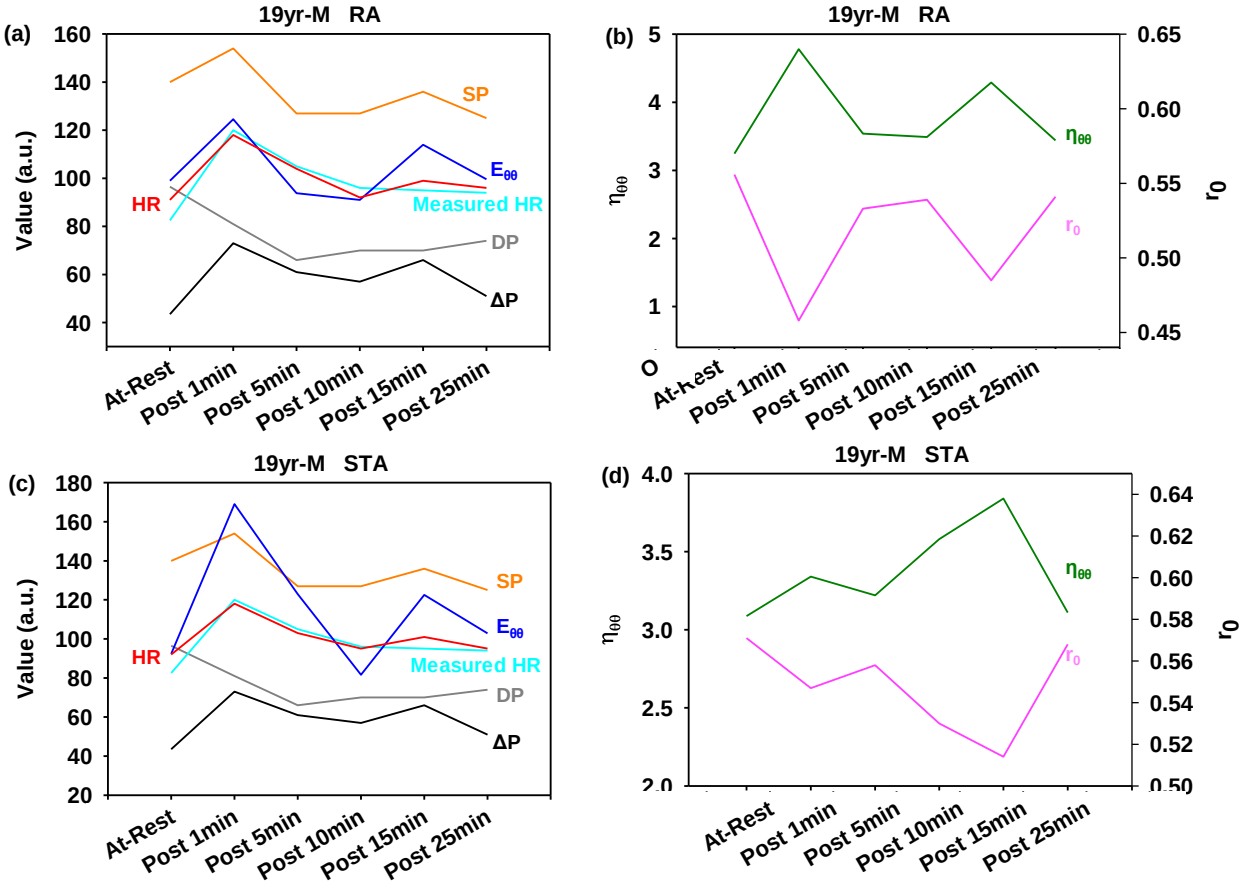


Figure 6.18 Compare the estimated arterial wall parameters and HR with the measured results from a medical instrument for 19yr-M subject before and post-exercise at RA and STA.

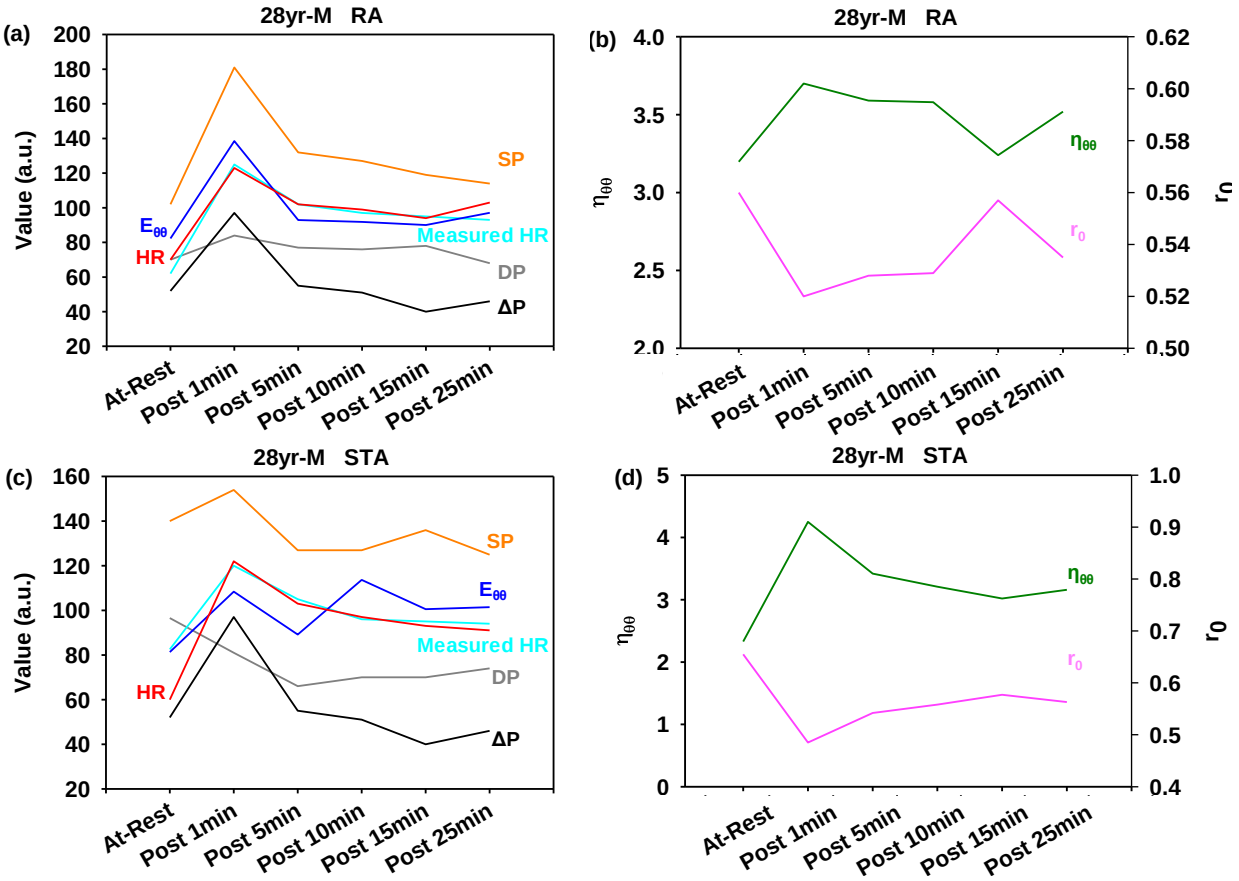


Figure 6.19 Compare the estimated arterial wall parameters and HR with the measured results from a medical instrument for the 28yr-M subject before and post-exercise at RA and STA.

## 6.4 Conclusion

This chapter presents the sensor optimization method by adding a conformal layer between sensor and skin to enhance sensor-artery interaction. The performance of the sensor with a conformal layer on the estimation of arterial wall parameters is examined. First, the results of the performance characterization of the sensor with a conformal layer reveal good linearity. Then, two experiments were carried out for analyzing how the sensor design and subject-specific parameters affect the estimation of arterial wall parameters.

The first experiment was conducted by measuring the pulse signals on subjects using a sensor with a conformal layer using the different PDMS mixing ratio with varying thickness. The

results from six subjects show the significant improvement of pulse amplitude after adding a conformal layer at RA and STA, especially in the subject with high BMI. The second experiment is conducted by tracking the changes in arterial wall parameters via moderate exercise using the sensor with a conformal layer. Two subjects with different BMI were enrolled for this purpose. The subjects are required to do 5mins moderate exercise; then their pulse signals were measured post-exercise at the different time period. A medical instrument, Paramed monitor, was used to measure the blood pressure and heart rate before and post-exercise on the two subjects. The obtained changes in arterial wall parameters were consistent with the measured changes using a medical instrument. Overall, the study on the estimation of arterial wall parameters using a tactile with a conformal layer suggests that the model-based analysis is promising in monitoring cardiovascular change at home.

# CHAPTER 7

# CONCLUSIONS AND FUTURE WORK

## 7.1 Conclusions

This dissertation focuses on the estimation of arterial wall parameters via model-based analysis of noninvasively measured pulse signals via a microfluidic-based tactile sensor. The objective is to offer a simple-use, low-cost, home use tool for monitoring arterial wall parameters. To achieve the objective, specific aims are include: (1) design and develop a tactile sensor for arterial pulse measurement; (2) design, develop, and implement a model-based analysis for extracting the arterial wall parameters; (3) optimization of sensor design, improvement of sensor-artery interaction, and the investigation of the influence of arterial wall parameters on the sensor design, arterial sites, and subject specificity. Meanwhile, statistical analysis, such as linear regression or t-test, is used to compare the difference under different conditions. A series of studies were performed to achieve the aims: 1) experimental study on the performance of the sensor for arterial pulse measurements at different arterial sites, such as RA, CA, and STA; 2) experimental study on extracting arterial wall parameters from human subjects at rest and post-exercise at different time period, 1min, 5mins, 10mins, 15mins, and 25mins; and 3) experimental study on sensor optimization, its performance of improving the sensor-artery interaction, and its effects of subject specificity. Moreover, a medical instrument is introduced as a reference for comparing the physical condition before and after exercise. As compared with current medical devices for pulse signal measurements (pulse oximeters or PPG sensors), the developed sensor offers great robustness to motion artifacts and thus improves the accuracy in the derived physiological parameters for monitoring cardiovascular health.

### 7.1.1 Study on Performance of Arterial Pulse Measurement Via A Microfluidic-based Tactile Sensor

The objective of this study was to investigate the performance of the sensor on arterial pulse measurement and extract parameters related to the health condition and arterial wall elasticity. In this dissertation, a tactile sensor with the same design was built on Pyrex/PET substrate. The sensor entails a PDMS microstructure embedded with an electrolyte-enabled 5×1 transducer array, with a 1.5mm-resolution being compatible with the radial and carotid arterial dimensions. Via the sensor, the radial and carotid arterial pulse signals of five subjects are recorded as a resistance signal with motion artifacts. Related signal-processing algorithms are written in Matlab to remove motion artifacts from the resistance signal, extract the key tonometric parameters, and calculate the PWV and radial and carotid AI.

While the measured difference between radial and carotid pulse waveforms of a subject is consistent with the related findings in the literature, the difference in the measured pulse waveform among the subjects also reveals related physiological significance. The tonometric parameters extracted from the five subjects show the feasibility of the sensor for capturing the key feature of the pulse signals. The calculated carotid-radial PWV for the two subjects without hypertension is in line with the PWV values in the literature: a normal distribution of 9.01±1.2 m/s of 17 individuals with an age distribution of 32.8±9.5 years [58]. The measured carotid-radial PWV of three subjects manifests how the PWV should vary with gender and hypertension. According to the literature [59], the radial AI is higher than the carotid AI regardless of sex (7.1±20.2 versus 73.8±18.5 for men and 18.6±16.9 versus 84.5±17.1 for women). The calculated radial and carotid AI of the five subjects captures its positive correlation with age and gender.

Additionally, the sensor exhibits reasonably good repeatability in measuring a pulse signal with similar finger-holding strength.

Whereas the tonometric parameters of the measured radial and carotid pulse waveforms on each subject are consistent with the related findings in the literature, the difference in tonometric parameters among the subjects also reveals physiological significance. The measured PWV and radial and carotid AI of the subjects show good agreement with how they should vary with age and gender. As a result, this sensor has the potential of serving as a cheap and convenient point-of-care diagnostic tool for an untrained individual to keep track of his cardiovascular condition.

### 7.1.2 Study on Arterial Wall Parameters Extracting from Subjects At-Rest and Post-Exercise

Arterial wall parameters (i.e., radius and viscoelasticity) are prognostic markers for Cardiovascular Diseases (CVD), but their current monitoring systems are too complex for home use. The objective of this study is to estimate the arterial wall parameters via models and validate the proposed model from measured arterial pulse signals. The equations for the longitudinal and radial motion of the arterial wall were derived to understand the physiological meaning in pulse propagation. The governing equation for the radial motion of the arterial wall was derived, indicating that the driving force for the radial wall motion is the longitudinal stretching of the arterial wall, which arises from the axial blood flow in an artery.

Based on the derived governing equation and time-harmonic nature of the radial wall motion, the arterial model is modeled as a second-order dynamic system. A data-processing algorithm was utilized to process the measured pulse signal to obtain the radius waveform and its first-order and second-order derivatives, and extract their key features. A dynamic system model of the arterial wall and a hemodynamic model of the blood flow were developed to interpret the

extracted key features for estimating arterial wall parameters, with no need of calibration. Consequently, the spring stiffness and damping coefficient of the dynamic system are representative of the elasticity and viscosity of the arterial wall, respectively.

First, pulse signals are measured at RA and STA of seven healthy subjects at rest using a microfluidic-based tactile sensor. The measured results show that there is a moderate difference in $E_{\theta\theta}$ and $\eta_{\theta\theta}$ between the two arteries, but a large difference among the subjects. This is believed to be caused by the small absolute values of wall viscosity, relative to the value of wall elasticity. The measured difference in the physical properties between the two arteries and among the seven subjects validates the feasibility of the proposed dynamic modeling of the radial wall motion to capture the physical properties of the arterial wall. Because a measured pulse signal is a combination of the sensor, $P_{HD}$, the subject-specific parameters (i.e., overlying tissue and blood pressure) and the arterial wall, the measured difference in the two physical properties is not suitable for comparison between different arteries and different subjects unless $P_{HD}$ is well controlled and the influence of the sensor design and subject-specific parameters are considered.

Then, the change in the cardiovascular system influences arterial stiffness and damping via exercise was introduced to solve these problems. Changes in arterial wall parameters were introduced to healthy subjects (n=5) by moderate exercise. The estimated values were compared between pre-exercise and post-exercise for a significant difference ($p<0.05$). The estimated changes on the radius, elasticity, and viscosity were consistent with the findings in the literature (between pre-exercise and 1min post-exercise: -11%±4%, 55%±38% and 28%±11% at the radial artery; -7%±3%, 36%±28% and 16%±8% at the carotid artery).

The experiment conducted on the two subjects, 19yr-M and 28yr-M, indicates the effectiveness of tracking changes in arterial wall parameters from the measured signals using the

sensor with a conformal layer. The amplitude of the pulse signals is significantly enhanced by adding a conformal layer, especially for the subject with high BMI. The estimated parameters are consistent with the measured results from a medical instrument.

Overall, the model-based analysis allows tracking changes in arterial wall parameters using a microfluidic-based tactile sensor. It shows the potential of developing a solution to at-home monitoring of the cardiovascular system for early detection of CVD.

### 7.1.3 Study on Optimization of Sensor Design and Evaluation of Its Performance

The objective of this study was to optimize the sensor design for improving sensor-artery interaction. The factors that influence the arterial pulse measurement are analyzed, which includes hold-down pressure, sensor sensitivity, and inter-subject variation. To implement the sensor for practical use, an optimized sensor with different thickness of varying stiffness and damping are utilized in measuring pulse signals at RA and STA. The measured results were obtained from six male subjects (two of them have higher BMI, over 29) at rest using the sensor with different conformal layers.

The pulse measured without a conformal layer as a reference, the influence of a conformal layer on a measured pulse signal is evaluated by its characterization and performance on arterial pulse measurement. A conformal layer greatly amplifies the pulse signals at the two RA and STA. For those subjects with higher BMI, the influence of the conformal layer is critical by enhancing the amplitude of pulse signals. Thicker conformal layer or higher stiffness of a conformal layer with the same thickness may weaken the influence the respiration waveform at RA While, lower stiffness of the conformal layer weakens the respiration waveform at STA. The proposed sensor designs significantly improve the sensor-artery interaction which makes the

sensor available to subjects with different subject-specificity. It provides a convenient at home pulse measurement method and promising approach for patient-specific pulse monitoring.

**7.2 Study Limitation and Future Work**

This study is focused on the study the feasibility of the proposed method for estimating arterial wall parameters from measured arterial pulse signals on subjects at different arteries. Due to the small sample size of subjects, the statistical analysis is limited and impedes the qualitative research. It is difficult to find a significant relationship from the measured results since the statistical tests normally require a larger sample size. Despite numerous significant efforts devoted to developing the method on the estimation of arterial wall parameters, there are still several challenges in the future study.

First, the method for arterial pulse measurement could be improved. The hold-down pressure varies due to the variation in neighboring tissues and blood pressures among different subjects. The same hold-down pressure does not translate to the same transmural pressure. Motion artifacts introduce further variation to the transmural pressure in different pulse cycles of measured pulse signals. A method for calibrating or quantifying the changes on hold-down pressure could be developed in the future. Develop effective motion artifacts (MA) reduction or removal method is also crucial to improve the accuracy for arterial pulse measurement. Though numerous solutions have been investigated to solve this problem, such as motion-resistant sensing design with processing algorithms for noise cancellation and multisensory fusion for MA identification, it is still a major obstacle to overcome.

Second, the tactile sensor could be used for monitoring the cardiovascular system on patients. The envisioned application of this work is for periodically tracking changes of arterial wall parameters at home, after a diagnosis is conducted using medical instruments at a clinic.

The estimated values of arterial wall parameters at the diagnosis site is used as the reference. Afterward, patients or caregivers at home will use our approach to track changes of arterial wall parameters relative to the reference for timely intervention and treatment assessment, before the next scheduled clinical diagnosis arrives. For now, the measured results are obtained from healthy subjects with different ages and BMIs. To validate the capability of health monitoring, the sensor could be used to monitor arterial pulse signals from patients. As compared with the healthy subjects, the measured pulse signals from patients may carry significant meanings for implementing the sensor for daily use.

Third, the current method for extracting arterial wall parameters is a lack of calibration from medical instruments. To further validate the accuracy of the current sensor on tracking these parameters, comparison, and calibration of the measured results with commercial instruments is necessary. These medical instruments may be utilized for comparisons, such as UltraSound, MRI, and Patient Monitor.

## REFERENCES


[1] M. Heron, and R. N. Anderson, “Changes in the leading cause of death: recent patterns in heart disease and cancer mortality,” *Cancer,* vol. 400, no. 500000, pp. 600000, 2016.

[2] S. Mendis, P. Puska, B. Norrving *et al.*, *Global atlas on cardiovascular disease prevention and control*: Geneva: World Health Organization, 2011.

[3] C. Leguy, E. Bosboom, H. Gelderblom *et al.*, “Estimation of distributed arterial mechanical properties using a wave propagation model in a reverse way,” *Medical Engineering and Physics,* vol. 32, no. 9, pp. 957-967, 2010.

[4] A. C. Guyton, and J. E. Hall, “Textbook of medical physiology. 11th,” *WB Sounders Company, Philadelphia*, 2006.

[5] C. Vlachopoulos, M. O'Rourke, and W. W. Nichols, *McDonald's blood flow in arteries: theoretical, experimental and clinical principles*: CRC press, 2011.

[6] D. Bergel, “The static elastic properties of the arterial wall,” *The Journal of physiology,* vol. 156, no. 3, pp. 445-457, 1961.

[7] H. Gray, and S. Standring, *Gray's anatomy*: Arcturus Publishing, 2008.

[8] T. Khamdaeng, J. Luo, J. Vappou *et al.*, “Arterial stiffness identification of the human carotid artery using the stress–strain relationship in vivo,” *Ultrasonics,* vol. 52, no. 3, pp. 402-411, 2012.

[9] M. F. O’rourke, and J. Hashimoto, “Mechanical factors in arterial aging: a clinical perspective,” *Journal of the American College of Cardiology,* vol. 50, no. 1, pp. 1-13, 2007.

[10] Y. Fung, "Biomechanics: circulation, chapter 4," New York: Springer, 1997.

[11] M. Safar, J. Blacher, J. Mourad *et al.*, “Stiffness of carotid artery wall material and blood pressure in humans: application to antihypertensive therapy and stroke prevention,” *Stroke,* vol. 31, no. 3, pp. 782-790, 2000.

[12] M. F. O'rourke, and G. Mancia, "Arterial stiffness," LWW, 1999.

[13] L. J. S. da Fonseca, M. A. Mota-Gomes, and L. A. Rabelo, “Radial applanation tonometry as an adjuvant tool in the noninvasive arterial stiffness and blood pressure assessment,” *World Journal of Cardiovascular Diseases,* vol. 4, no. 05, pp. 225, 2014.

[14] W. W. Nichols, “Clinical measurement of arterial stiffness obtained from noninvasive pressure waveforms,” *American journal of hypertension,* vol. 18, no. S1, pp. 3S-10S, 2005.

[15] D. Bia, I. Aguirre, Y. Zócalo *et al.*, “Regional differences in viscosity, elasticity, and wall buffering function in systemic arteries: pulse wave analysis of the arterial pressure-diameter relationship,” *Revista Española de Cardiología (English Edition),* vol. 58, no. 2, pp. 167-174, 2005.

[16] Z. Lénárd, D. Fülöp, Z. Visontai *et al.*, “Static versus Dynamic Distensibility of the Carotid Artery in Humans,” *Journal of Vascular Research,* vol. 37, no. 2, pp. 103-111, 2000.

[17] D. H. Bergel, “The dynamic elastic properties of the arterial wall,” *The Journal of Physiology,* vol. 156, no. 3, pp. 458-469, 1961.

[18] L. Wang, S. Ansari, D. Slavin *et al.*, “Non-invasive vascular resistance monitoring with a piezoelectric sensor and photoplethysmogram,” *Sensors and Actuators A: Physical,* vol. 263, pp. 198-208, 2017.

[19] D. Perloff, C. Grim, J. Flack *et al.*, "Human blood pressure determination by sphygmomanometry," *Circulation,* vol. 88, no. 5, pp. 2460-2470, 1993.
[20] M. Karamanoglu, M. O'rourke, A. Avolio *et al.*, "An analysis of the relationship between central aortic and peripheral upper limb pressure waves in man," *European heart journal,* vol. 14, no. 2, pp. 160-167, 1993.
[21] L. A. Geddes, *Handbook of blood pressure measurement*: Springer Science & Business Media, 2013.
[22] Y. L. Shevchenko, and J. E. Tsitlik, "90th Anniversary of the development by Nikolai S. Korotkoff of the auscultatory method of measuring blood pressure," *Circulation,* vol. 94, no. 2, pp. 116-118, 1996.
[23] T. G. Pickering, J. E. Hall, L. J. Appel *et al.*, "Recommendations for blood pressure measurement in humans and experimental animals: part 1: blood pressure measurement in humans: a statement for professionals from the Subcommittee of Professional and Public Education of the American Heart Association Council on High Blood Pressure Research," *Circulation,* vol. 111, no. 5, pp. 697-716, 2005.
[24] M. Ramsey, "Blood pressure monitoring: automated oscillometric devices," *Journal of clinical monitoring,* vol. 7, no. 1, pp. 56-67, 1991.
[25] G. M. Drzewiecki, J. Melbin, and A. Noordergraaf, "Arterial tonometry: review and analysis," *Journal of biomechanics,* vol. 16, no. 2, pp. 141-152, 1983.
[26] K. Matthys, and P. Verdonck, "Development and modelling of arterial applanation tonometry: a review," *Technology and Health Care,* vol. 10, no. 1, pp. 65-76, 2002.
[27] J. Penaz, "Photoelectric measurement of blood pressure, volume and flow in the finger'In: Digest of the 10th International Conference on Medical and Biological Engineering," *Dresden,* vol. 104, 1973.
[28] J. Allen, "Photoplethysmography and its application in clinical physiological measurement," *Physiological measurement,* vol. 28, no. 3, pp. R1, 2007.
[29] E. Soleimani, M. Mokhtari-Dizaji, N. Fatouraee *et al.*, "Assessing the blood pressure waveform of the carotid artery using an ultrasound image processing method," *Ultrasonography,* vol. 36, no. 2, pp. 144, 2017.
[30] P. Tortoli, R. Bettarini, F. Guidi *et al.*, "A simplified approach for real-time detection of arterial wall velocity and distension," *IEEE transactions on ultrasonics, ferroelectrics, and frequency control,* vol. 48, no. 4, pp. 1005-1012, 2001.
[31] A. E. Zavodni, B. A. Wasserman, R. L. McClelland *et al.*, "Carotid artery plaque morphology and composition in relation to incident cardiovascular events: the Multi-Ethnic Study of Atherosclerosis (MESA)," *Radiology,* vol. 271, no. 2, pp. 381-389, 2014.
[32] B. M. Pannier, A. P. Avolio, A. Hoeks *et al.*, "Methods and devices for measuring arterial compliance in humans," *American journal of hypertension,* vol. 15, no. 8, pp. 743-753, 2002.
[33] D. Valdez-Jasso, D. Bia, Y. Zócalo *et al.*, "Linear and nonlinear viscoelastic modeling of aorta and carotid pressure–area dynamics under in vivo and ex vivo conditions," *Annals of biomedical engineering,* vol. 39, no. 5, pp. 1438-1456, 2011.
[34] H. Shin, and S. D. Min, "Feasibility study for the non-invasive blood pressure estimation based on ppg morphology: normotensive subject study," *Biomedical engineering online,* vol. 16, no. 1, pp. 10, 2017.

[35] M. Alivon, T. V.-D. Phuong, V. Vignon *et al.*, “A novel device for measuring arterial stiffness using finger-toe pulse wave velocity: Validation study of the pOpmètre®,” *Archives of cardiovascular diseases,* vol. 108, no. 4, pp. 227-234, 2015.

[36] Y.-F. Cheung, “Arterial stiffness in the young: assessment, determinants, and implications,” *Korean circulation journal,* vol. 40, no. 4, pp. 153-162, 2010.

[37] V. Eck, J. Sturdy, and L. Hellevik, “Effects of arterial wall models and measurement uncertainties on cardiovascular model predictions,” *Journal of biomechanics,* vol. 50, pp. 188-194, 2017.

[38] A. S. Liberson, J. S. Lillie, S. W. Day *et al.*, “A physics based approach to the pulse wave velocity prediction in compliant arterial segments,” *Journal of biomechanics,* vol. 49, no. 14, pp. 3460-3466, 2016.

[39] J. Menacho, L. Rotllant, J. Molins *et al.*, “Arterial pulse attenuation prediction using the decaying rate of a pressure wave in a viscoelastic material model,” *Biomechanics and modeling in mechanobiology,* vol. 17, no. 2, pp. 589-603, 2018.

[40] A. R. Ghigo, X.-F. Wang, R. Armentano *et al.*, “Linear and nonlinear viscoelastic arterial wall models: application on animals,” *Journal of biomechanical engineering,* vol. 139, no. 1, pp. 011003, 2017.

[41] A. Lungu, J. Wild, D. Capener *et al.*, “MRI model-based non-invasive differential diagnosis in pulmonary hypertension,” *Journal of biomechanics,* vol. 47, no. 12, pp. 2941-2947, 2014.

[42] L. Peter, N. Noury, and M. Cerny, “A review of methods for non-invasive and continuous blood pressure monitoring: Pulse transit time method is promising?,” *Irbm,* vol. 35, no. 5, pp. 271-282, 2014.

[43] D. Wang, J. Shen, L. Mei *et al.*, “Performance Investigation of a Wearable Distributed-Deflection Sensor in Arterial Pulse Waveform Measurement,” *IEEE Sensors Journal,* vol. 17, no. 13, pp. 3994-4004, 2017.

[44] S.-i. Katsuda, K. Takazawa, M. Miyake *et al.*, “Local pulse wave velocity directly reflects increased arterial stiffness in a restricted aortic region with progression of atherosclerotic lesions,” *Hypertension Research,* vol. 37, no. 10, pp. 892, 2014.

[45] O. Lichtenstein, M. E. Safar, E. Mathieu *et al.*, “Static and Dynamic Mechanical Properties of the Carotid Artery From Normotensive and Hypertensive Rats,” *Hypertension,* vol. 32, no. 2, pp. 346-350, 1998.

[46] L. Wang, S. Ansari, K. Najarian *et al.*, "Estimation of peripheral artery radius using non-invasive sensors and Kalman filtering of local dynamics." pp. 807-812.

[47] Y. Shi, P. Lawford, and R. Hose, “Review of zero-D and 1-D models of blood flow in the cardiovascular system,” *Biomedical engineering online,* vol. 10, no. 1, pp. 33, 2011.

[48] W. Gu, P. Cheng, A. Ghosh *et al.*, “Detection of distributed static and dynamic loads with electrolyte-enabled distributed transducers in a polymer-based microfluidic device,” *Journal of Micromechanics and Microengineering,* vol. 23, no. 3, pp. 035015, 2013.

[49] P. Cheng, W. Gu, J. Shen *et al.*, "Performance Characterization of a PDMS-Based Microfluidic Device for Detecting Continuous Distributed Loads." pp. V010T11A063-V010T11A063.

[50] D. Wang, D. J. Krusienski, and Z. Hao, "A Flexible PET-based Wearable Sensor for Arterial Pulse Waveform Measurement." pp. 66-75.

[51] T. Ashraf, Z. Panhwar, S. Habib *et al.*, "Size of radial and ulnar artery in local population," *JPMA-Journal of the Pakistan Medical Association,* vol. 60, no. 10, pp. 817, 2010.
[52] J. Krejza, M. Arkuszewski, S. E. Kasner *et al.*, "Carotid artery diameter in men and women and the relation to body and neck size," *Stroke,* vol. 37, no. 4, pp. 1103-1105, 2006.
[53] W. J. Hurst, "The heart: arteries and veins," 1982.
[54] C. M. McEniery, J. R. Cockcroft, M. J. Roman *et al.*, "Central blood pressure: current evidence and clinical importance," *European heart journal,* vol. 35, no. 26, pp. 1719-1725, 2014.
[55] R. Kelly, C. Hayward, A. Avolio *et al.*, "Noninvasive determination of age-related changes in the human arterial pulse," *Circulation,* vol. 80, no. 6, pp. 1652-1659, 1989.
[56] G. F. Mitchell, S.-J. Hwang, R. S. Vasan *et al.*, "Arterial stiffness and cardiovascular events: the Framingham Heart Study," *Circulation,* vol. 121, no. 4, pp. 505-511, 2010.
[57] P. Digiglio, R. Li, W. Wang *et al.*, "Microflotronic arterial tonometry for continuous wearable non-invasive hemodynamic monitoring," *Annals of biomedical engineering,* vol. 42, no. 11, pp. 2278-2288, 2014.
[58] O. McEleavy, R. McCallum, J. Petrie *et al.*, "Higher carotid–radial pulse wave velocity in healthy offspring of patients with Type 2 diabetes," *Diabetic Medicine,* vol. 21, no. 3, pp. 262-266, 2004.
[59] J. Sugawara, H. Komine, K. Hayashi *et al.*, "Relationship between augmentation index obtained from carotid and radial artery pressure waveforms," *Journal of hypertension,* vol. 25, no. 2, pp. 375-381, 2007.
[60] M. F. O'Rourke, and D. E. Gallagher, "Pulse wave analysis," *Journal of hypertension. Supplement: official journal of the International Society of Hypertension,* vol. 14, no. 5, pp. S147-57, 1996.
[61] T. Weber, J. Auer, M. F. O'rourke *et al.*, "Arterial stiffness, wave reflections, and the risk of coronary artery disease," *Circulation,* vol. 109, no. 2, pp. 184-189, 2004.
[62] J. P. Murgo, N. Westerhof, J. P. Giolma *et al.*, "Aortic input impedance in normal man: relationship to pressure wave forms," *Circulation,* vol. 62, no. 1, pp. 105-116, 1980.
[63] Z. He, Y. Zhang, Z. Ma *et al.*, "A low-pass differentiation filter based on the 2nd-order B-spline wavelet for calculating augmentation index," *Medical engineering & physics,* vol. 36, no. 6, pp. 786-792, 2014.
[64] C. S. J. Leitão, P. F. da Costa Antunes, J. A. M. Bastos *et al.*, "Plastic optical fiber sensor for noninvasive arterial pulse waveform monitoring," *IEEE Sensors Journal,* vol. 15, no. 1, pp. 14-18, 2015.
[65] J. J. Oliver, and D. J. Webb, "Noninvasive assessment of arterial stiffness and risk of atherosclerotic events," *Arteriosclerosis, thrombosis, and vascular biology,* vol. 23, no. 4, pp. 554-566, 2003.
[66] K. Kohara, Y. Tabara, A. Oshiumi *et al.*, "Radial augmentation index: a useful and easily obtainable parameter for vascular aging," *American journal of hypertension,* vol. 18, no. S1, pp. 11S-14S, 2005.
[67] Y.-S. Lee, K.-S. Kim, C.-W. Nam *et al.*, "Clinical implication of carotid-radial pulse wave velocity for patients with coronary artery disease," *Korean Circulation Journal,* vol. 36, no. 8, pp. 565-572, 2006.

[68] M. Willemet, and J. Alastruey, "Arterial pressure and flow wave analysis using time-domain 1-D hemodynamics," *Annals of biomedical engineering,* vol. 43, no. 1, pp. 190-206, 2015.

[69] G. Baltgaile, "Arterial wall dynamics," *Perspectives in Medicine,* vol. 1, no. 1-12, pp. 146-151, 2012.

[70] R. K. Warriner, K. W. Johnston, and R. S. Cobbold, "A viscoelastic model of arterial wall motion in pulsatile flow: implications for Doppler ultrasound clutter assessment," *Physiological measurement,* vol. 29, no. 2, pp. 157, 2008.

[71] T. Pereira, C. Correia, and J. Cardoso, "Novel methods for pulse wave velocity measurement," *Journal of medical and biological engineering,* vol. 35, no. 5, pp. 555-565, 2015.

[72] H. Yli‐Ollila, T. Laitinen, M. Weckström *et al.*, "New indices of arterial stiffness measured from longitudinal motion of common carotid artery in relation to reference methods, a pilot study," *Clinical physiology and functional imaging,* vol. 36, no. 5, pp. 376-388, 2016.

[73] S. H. Taivainen, H. Yli-Ollila, M. Juonala *et al.*, "Influence of cardiovascular risk factors on longitudinal motion of the common carotid artery wall," *Atherosclerosis*, 2018.

[74] S. H. Taivainen, H. Yli‐Ollila, M. Juonala *et al.*, "Interrelationships between indices of longitudinal movement of the common carotid artery wall and the conventional measures of subclinical arteriosclerosis," *Clinical physiology and functional imaging,* vol. 37, no. 3, pp. 305-313, 2017.

[75] S. Svedlund, and L. M. Gan, "Longitudinal wall motion of the common carotid artery can be assessed by velocity vector imaging," *Clinical physiology and functional imaging,* vol. 31, no. 1, pp. 32-38, 2011.

[76] J. Tat, J. S. Au, P. J. Keir *et al.*, "Reduced common carotid artery longitudinal wall motion and intramural shear strain in individuals with elevated cardiovascular disease risk using speckle tracking," *Clinical physiology and functional imaging,* vol. 37, no. 2, pp. 106-116, 2017.

[77] H. Yli-Ollila, M. P. Tarvainen, T. P. Laitinen *et al.*, "Principal component analysis of the longitudinal carotid wall motion in association with vascular stiffness: a pilot study," *Ultrasound in Medicine and Biology,* vol. 42, no. 12, pp. 2873-2886, 2016.

[78] J. S. Au, D. S. Ditor, M. J. MacDonald *et al.*, "Carotid artery longitudinal wall motion is associated with local blood velocity and left ventricular rotational, but not longitudinal, mechanics," *Physiological reports,* vol. 4, no. 14, pp. e12872, 2016.

[79] J. S. Au, P. A. Bochnak, S. E. Valentino *et al.*, "Cardiac and haemodynamic influence on carotid artery longitudinal wall motion," *Experimental physiology*, vol. 103, no. 1, pp. 141-152, 2018.

[80] S. Qorchi, G. Zahnd, D. Galbrun *et al.*, "Kalman-Based Carotid-Artery Longitudinal-Kinetics Estimation and Pattern Recognition," *IRBM,* vol. 38, no. 4, pp. 219-223, 2017.

[81] Å. R. Ahlgren, S. Steen, S. Segstedt *et al.*, "Profound increase in longitudinal displacements of the porcine carotid artery wall can take place independently of wall shear stress: a continuation report," *Ultrasound in Medicine and Biology,* vol. 41, no. 5, pp. 1342-1353, 2015.

[82] J. R. Womersley, "XXIV. Oscillatory motion of a viscous liquid in a thin-walled elastic tube—I: The linear approximation for long waves," *The London, Edinburgh, and Dublin Philosophical Magazine and Journal of Science,* vol. 46, no. 373, pp. 199-221, 1955.

[83] G. Morgan, and J. Kiely, “Wave propagation in a viscous liquid contained in a flexible tube,” *The Journal of the Acoustical Society of America,* vol. 26, no. 3, pp. 323-328, 1954.
[84] D. Hughes, L. Geddes, J. Bourland *et al.*, "Dynamic imaging of the aorta in-vivo with 10 MHz ultrasound," *Acoustical imaging,* pp. 699-707: Springer, 1980.
[85] T. G. Papaioannou, and C. Stefanadis, “Vascular wall shear stress: basic principles and methods,” *Hellenic J Cardiol,* vol. 46, no. 1, pp. 9-15, 2005.
[86] N. Etchenique, S. R. Collin, and T. R. Moore, “Coupling of transverse and longitudinal waves in piano strings,” *The Journal of the Acoustical Society of America,* vol. 137, no. 4, pp. 1766-1771, 2015.
[87] B. Bank, and L. Sujbert, “Generation of longitudinal vibrations in piano strings: From physics to sound synthesis,” *The Journal of the Acoustical Society of America,* vol. 117, no. 4, pp. 2268-2278, 2005.
[88] L. Horný, M. Netušil, and T. Voňavková, “Axial prestretch and circumferential distensibility in biomechanics of abdominal aorta,” *Biomechanics and modeling in mechanobiology,* vol. 13, no. 4, pp. 783-799, 2014.
[89] C. Fortier, and M. Agharazii, “Arterial stiffness gradient,” *Pulse,* vol. 3, no. 3-4, pp. 159-166, 2015.
[90] A. V. Kamenskiy, I. I. Pipinos, Y. A. Dzenis *et al.*, “Passive biaxial mechanical properties and in vivo axial pre-stretch of the diseased human femoropopliteal and tibial arteries,” *Acta biomaterialia,* vol. 10, no. 3, pp. 1301-1313, 2014.
[91] G. Zhang, J.-O. Hahn, and R. Mukkamala, “Tube-load model parameter estimation for monitoring arterial hemodynamics,” *Frontiers in physiology,* vol. 2, pp. 72, 2011.
[92] D. Wang, L. Vahala, T. Alberts *et al.*, “Arterial Wall Motion and Its Dynamic Modeling for Arterial Stiffness and Damping,” *International Mechanical Engineering Congress & Exposition (IMECE 2018), Accepted.*
[93] D. Wang, L. Reynolds, T. Alberts *et al.*, “Model-based Analysis of Arterial Pulse Signals for Tracking Changes of Arterial Wall Parameters: a Pilot Study,” *IEEE Transactions on Biomedical Engineering, Under Review,* 2018.
[94] M. Boledovičová, J. Hendl, L. Lišková *et al.*, “Blood pressure relation to body composition and age: analysis of a nurse-led investigation and consultation program,” *Medical science monitor: international medical journal of experimental and clinical research,* vol. 19, pp. 612, 2013.
[95] B. S. Kim, Y. J. Jung, C. H. Chang *et al.*, “The anatomy of the superficial temporal artery in adult koreans using 3-dimensional computed tomographic angiogram: clinical research,” *Journal of cerebrovascular and endovascular neurosurgery,* vol. 15, no. 3, pp. 145-151, 2013.
[96] M. Guerrisi, I. Vannucci, and N. Toschi, “Differential response of peripheral arterial compliance-related indices to a vasoconstrictive stimulus,” *Physiological measurement,* vol. 30, no. 1, pp. 81, 2008.
[97] P. Singh, M. I. Choudhury, S. Roy *et al.*, “Computational study to investigate effect of tonometer geometry and patient-specific variability on radial artery tonometry,” *Journal of biomechanics,* vol. 58, pp. 105-113, 2017.
[98] P. Studinger, Z. Lénárd, Z. Kováts *et al.*, “Static and dynamic changes in carotid artery diameter in humans during and after strenuous exercise,” *The Journal of physiology,* vol. 550, no. 2, pp. 575-583, 2003.

[99] A. F. Mutter, A. B. Cooke, O. Saleh *et al.*, "A systematic review on the effect of acute aerobic exercise on arterial stiffness reveals a differential response in the upper and lower arterial segments," *Hypertension Research,* vol. 40, no. 2, pp. 146, 2017.

[100] R. J. Doonan, A. Mutter, G. Egiziano *et al.*, "Differences in arterial stiffness at rest and after acute exercise between young men and women," *Hypertension Research,* vol. 36, no. 3, pp. 226, 2013.

[101] X. Melo, B. Fernhall, D. A. Santos *et al.*, "The acute effect of maximal exercise on central and peripheral arterial stiffness indices and hemodynamics in children and adults," *Applied Physiology, Nutrition, and Metabolism,* vol. 41, no. 3, pp. 266-276, 2015.

[102] J. C. Greenfield JR, and D. M. Griggs JR, "Relation between pressure and diameter in main pulmonary artery of man," *Journal of Applied Physiology,* vol. 18, no. 3, pp. 557-559, 1963.

[103] Z. Visontai, Z. Lenard, K. Karlocai *et al.*, "Assessment of the viscosity of the pulmonary artery wall," *European Respiratory Journal,* vol. 16, no. 6, pp. 1134-1141, 2000.

[104] J. C. Lee, Z. Ghasemi, C.-S. Kim *et al.*, "Investigation of Viscoelasticity in the Relationship between Carotid Artery Blood Pressure and Distal Pulse Volume Waveforms," *IEEE journal of biomedical and health informatics,* 2017.

[105] B. Spronck, T. Delhaas, A. G. De Lepper *et al.*, "Patient-specific blood pressure correction technique for arterial stiffness: evaluation in a cohort on anti-angiogenic medication," *Hypertension Research,* vol. 40, no. 8, pp. 752, 2017.

[106] J. Liu, H.-M. Cheng, C.-H. Chen *et al.*, "Patient-specific oscillometric blood pressure measurement: Validation for accuracy and repeatability," *IEEE journal of translational engineering in health and medicine,* vol. 5, pp. 1-10, 2017.

[107] K. Pilt, K. Meigas, M. Viigimaa *et al.*, "Arterial pulse waveform dependence on applied pressure." pp. 277-280.

[108] C. Pang, J. H. Koo, A. Nguyen *et al.*, "Highly skin-conformal microhairy sensor for pulse signal amplification," *Advanced materials,* vol. 27, no. 4, pp. 634-640, 2015.

[109] D. M. Drotlef, M. Amjadi, M. Yunusa *et al.*, "Bioinspired Composite Microfibers for Skin Adhesion and Signal Amplification of Wearable Sensors," *Advanced Materials,* 2017.

[110] N. Luo, W. Dai, C. Li *et al.*, "Flexible piezoresistive sensor patch enabling ultralow power cuffless blood pressure measurement," *Advanced Functional Materials,* vol. 26, no. 8, pp. 1178-1187, 2016.

[111] X. Teng, and Y. Zhang, "The effect of contacting force on photoplethysmographic signals," *Physiological measurement,* vol. 25, no. 5, pp. 1323, 2004.

[112] J. Lee, and K. C. Nam, "Tonometric Vascular Function Assessment," *Biomedical Engineering*: InTech, 2009.

[113] W. Jänig, "Autonomic nervous system," *Human physiology,* pp. 333-370: Springer, 1989.

[114] N. E. Huang, Z. Shen, S. R. Long *et al.*, "The empirical mode decomposition and the Hilbert spectrum for nonlinear and non-stationary time series analysis." pp. 903-995.

[115] Z. Wu, and N. E. Huang, "Ensemble empirical mode decomposition: a noise-assisted data analysis method," *Advances in adaptive data analysis,* vol. 1, no. 01, pp. 1-41, 2009.

[116] O. Kolade, T. O'Moore-Sullivan, M. Stowasser *et al.*, "Arterial stiffness, central blood pressure and body size in health and disease," *International Journal of Obesity,* vol. 36, no. 1, pp. 93, 2012.

# VITA

Dan Wang received her B.S. degree in Electronic Information Engineering from Southwest University of Science and Technology, Mianyang, China, in 2010 and received her M.E. degree in Control Engineering from University of Electronic Science and Technology of China, Chengdu, China, in 2013, respectively. She is currently a Ph.D. candidate in the Department of Mechanical and Aerospace Engineering at Old Dominion University. She has been working on the design, modeling, fabrication, characterization of microfluidic-based sensor built on Pyrex/PET substrate. She implemented the sensor in arterial pulse measurement on human subjects and rabbits. Her research interests are design, characterization, and application of a microfluidic-based tactile sensor, the development of model-based analysis for arterial wall parameters extraction and arterial pulse analysis.